Synthetic Tuning of Monodisperse Metallic Nanoparticles for Catalytic Applications

By

Sen Zhang

B.Sc., University of Science and Technology of China, 2008

M.A., Brown University, 2011

A Dissertation Submitted in Partial Fulfillment of the

Requirements for the Degree of Doctor of Philosophy

in the Department of Chemistry at Brown University

Providence, Rhode Island

May 2014

This dissertation by Sen Zhang is accepted in its present form

by the Department of Chemistry as satisfying the dissertation requirement

for the degree of Doctor of Philosophy.

Date _____   _____

                                                        Shouheng Sun, Advisor

Recommended to the Graduate Council by

Date _____   _____

                                                        Robert Hurt, Reader

Date _____   _____

                                                        J. William Suggs, Reader

Approved by the Graduate Council

Date _____   _____

                                                        Peter Weber, Dean of the Graduate School

Curriculum Vita

Sen Zhang was born on September 12, 1986, in Hefei, Anhui, China. He attended University of Science and Technology of China (Hefei, China) from 2004 to 2008, graduating with his B.Sc. in Chemistry. In 2009, he was accepted with a fellowship in the graduate program of the Department of Chemistry at Brown University to pursue the degree of Doctor of Philosophy in Chemistry. During this period, he held positions as research and teaching assistants. Since January 2010, he has focused on the synthetic tuning of monodisperse nanoparticles for catalytic and magnetic applications under the supervision of Professor Shouheng Sun. He has 14 papers published in peer-reviewed journals, 1 book chapter, 2 patents in pending and another 6 papers under review or in preparation.

Publications

21. **Sen Zhang**, Huiyuan Zhu, Guangming Jiang, Shouheng Sun, "Monodisperse AuMn Nanoparticles: A Superior Non-Pt Catalyst for Oxygen Reduction Reaction", in preparation.

20. **Sen Zhang**, Xu Zhang, Dong Su, Shouheng Sun, "Monodisperse intermetallic FePtNi/FePtCu Nanoparticles as Highly Efficient Catalysts for Oxygen Reduction Reaction", in preparation.

19. **Sen Zhang**, Guangming Jiang, Liheng Wu, Shouheng Sun, "Chemical Synthesis of Structure-Controllable Fe and FeCo High-moment Nanoparticles", in preparation.

18. **Sen Zhang**, Dong Su, Shaojun Guo, Huiyuan Zhu, Shouheng Sun, "A general one-pot approach to FePdM (M=Au, Ag and Cu) Trimetallic Nanoparticles", in preparation.

17. **Sen Zhang**, Xiaolian Sun, Aruna Sigdel, Shouheng Sun, "Synthetically Tuning Magnetic Nanoparticles for Biomedical Applications", *Chemical Society Reviews*, invited, in preparation.

16. Shaojun Guo,[§] **Sen Zhang**,[§] ([§]**equal contribution**) Dong Su, Shouheng Sun, "Seed-Mediated Synthesis of Core/Shell FePtM/FePt (M = Pd, Au) Nanowires and Their Electrocatalysis for Oxygen Reduction Reaction", Submitted to *Journal of the American Chemical Society*.

15. Huiyuan Zhu,[§] **Sen Zhang**,[§] ([§]**equal contribution**) Shaojun Guo, Dong Su, Shouheng Sun, "Synthetic Control of FePtM Nanorods (M = Cu, Ni) to Enhance Oxygen Reduction Reaction", *Journal of the American Chemical Society* **2013**, *135*, 7130-7133.

14. Huiyuan Zhu, **Sen Zhang**, Yuxi Huang, Liheng Wu, Shouheng Sun, "Monodisperse $M_xFe_{3-x}O_4$ (M = Mn, Fe, Co, Cu) Nanoparticles and Their Electrocatalysis for Oxygen Reduction Reaction", *Nano Letters*, **2013**, *13*, 2947-2951.

13. **Sen Zhang**, Shouheng Sun, "Iron Oxide Based Magnetic Nanoparticles for Biological Imaging", *Nanotechnology in Biological Imaging*, Edited by Mikhail Berezin, John Wiley & Sons, Ltd., in press.

12. **Sen Zhang**, Onder Metin, Dong Su, Shouheng Sun, "Monodisperse AgPd Alloy Nanoparticles and Their Superior Catalytic Activity in Formic Acid Dehydrogenation", *Angewandte Chemie International Edition*, **2013**, *52*, 3681-3684 (**VIP article**).

11. Shaojun Guo, Dongguo Li, Huiyuan Zhu, **Sen Zhang**, Nenad M. Markovic, Vojislav R. Stamenkovic, Shouheng Sun, "MPt (M = Fe, Co) Nanowires as Efficient Catalysts for Oxygen Reduction Reaction", *Angewandte Chemie International Edition*, **2013**, *52*, 3465-3468 (**VIP article**).

10. Jonghun Lee, **Sen Zhang**, Shouheng Sun, "Recent Progress in Synthesis and Applications of Magnetic and Semiconducting Metal Oxide Nanocrystals", *Chemistry of Materials*, **2013**, *25*, 1293-1304.

9. Shaojun Guo[§], **Sen Zhang**[§] ([§]**equal contribution**), Shouheng Sun, "Tuning Nanoparticle Catalysis for Oxygen Reduction Reaction", *Angewandte Chemie International Edition*, **2013**, *52*, 2-21.

8. Shaojun Guo, **Sen Zhang**, Liheng Wu, Shouheng Sun, "Co/CoO Nanoparticles Assembled on Graphene for Electrochemical Reduction of Oxygen", *Angewandte Chemie International Edition*, **2012**, *51*, 11770-11773 (**VIP article**).

7. **Sen Zhang**, Shaojun Guo, Huiyuan Zhu, Dong Su, Shouheng Sun, "Structure-Induced Enhancement in Electrooxidation of Trimetallic FePtAu Nanoparticles", *Journal of the American Chemical Society* **2012**, *134*, 5060-5063 (**Highlighted by *C&EN news* and Brown University Media Relations**).

6. **Sen Zhang**, Jonghun Lee, Shouheng Sun, "Chemical Synthesis of Monodisperse Magnetic Nanoparticles", *The Open Surface Science Journal* **2012**, *4*, 26-34.

5. Shaojun Guo, **Sen Zhang**, Xiaolian Sun, Shouheng Sun, "Synthesis of Ultrathin FePtPd Nanowires and Their Use as Catalysts for Methanol Oxidation Reaction**,** *Journal of the American Chemical Society* **2011**, *133*, 15354-15357.

4. **Sen Zhang**, Huiyuan Zhu, Zhi-Bin Hu, Lu Liu, Shaofeng Chen, Shu-Hong Yu, "Magnetite-Nanoparticles-Attached Necklace-like Cu@Cross-Linked Poly(vinyl

alcohol) Microcables: Synthesis, Individual Magnetic Manipulation and Fluorescent Property", *Chemical Communications* **2009**, 2326-2328.

3. Ming-Jun Hu, Yang Lu, **Sen Zhang**, Shi-Rui Guo, Bin Lin, Meng Zhang, Shu-Hong Yu, "High Yield Synthesis of Bracelet-like Hydrophilic Ni-Co Magnetic Alloy Flux-Closure Nanorings", *Journal of the American Chemical Society* **2008**, *130*, 11606-11607.

2. Sheng-Liang Zhong, Ji-Ming Song, **Sen Zhang**, An-Wu Xu, Wei-Tang Yao, Shu-Hong Yu, "Template-free Hydrothermal Synthesis and Formation Mechanism of Hematite Microrings", *The Journal of Physical Chemistry C* **2008**, *112*, 19916-19921.

1. Hua Wang, **Sen Zhang**, Mozhen Wang, Xuewu Ge, "Preparation of Monodisperse Polystyrene Particles from Emulsifier-free Miniemulsion Polymerization", *Chemistry Letters* **2008**, *37*, 1158-1159.

Acknowledgements

There are many people I would like to say "Thank you" for their kind help during my graduate study in the past four years. First of all, I would like to give my sincerest appreciation to my advisor, Professor Shouheng Sun. I have known him since he gave a very impressive presentation in my college, which was a huge propulsion to my coming to Brown for graduate study. I appreciate he gave me the valuable opportunity to join his group to pursue my PhD. He inspires me through his visionary insight, serious attitude and persistent passion in science. His support, encouragement and fatherly affection have accompanied me and warmed me for the past four years. Professor Sun, you have set up a perfect model for me to pursue my future dreams.

I am grateful to so many great professors at Brown. Professor Robert Hurt and Professor J. William Suggs served in my committee and provided a lot of valuable suggestions and encouragements during my RPD, ORP and research, directing me to become a PhD at every important step. Professor Wesley Bernskoetter, Professor Eunsuk Kim, Professor William Risen and Professor Dwight Sweigart gave their excellent teaching in my first year at Brown and laid my foundation for the understanding of advanced inorganic chemistry and scientific research methodology. I deeply appreciate Professor Wesley Bernskoetter and Prof. Eunsuk Kim for their help and support in my searching for postdoc positions. I also want to thank Professor Matthew Zimmt for his constant encouragement during my research and future planning.

I could have never accomplished my work if I did not have so many great and professional collaborators. Thank Dr. Dong Su at Brookhaven National Laboratory for his great work on STEM analysis of my samples. Thank Dr. Xu Zhang and Professor Gang Lu in the Department of Physics at California State University Northridge for their collaborations on theoretical calculations. Thank Dr. Anthony McCormick in the Department of Engineering at Brown for the help on TEM and SEM operation. Thank Dr. Joseph Orchardo and Dr. David Murray in the Department of Geological Science at Brown for help with ICP measurement.

I am also very fortunate to have worked with my wonderful group members. Dr. Shaojun Guo helped me a lot in electrochemistry and shared many experiences of his success with me. Professor Metin Önder, a previous postdoc at the Sun group, helped me in the design and synthesis of heterogeneous catalysts. Dr. Yi Liu gave me the introductory lessons of nanoparticle synthesis. Her pursuit to the high quality synthesis has a great influence on me in my own research. Thanks go to Jonghun Lee, Sally Ho and Aruna Sigdel. We have enjoyed a great time as a best team. Thanks, Dongguo Li, for the collaboration and the help in electrochemistry. Thanks, Liheng Wu, for knowing you almost eight years and joining the same college and lab together. Thanks, Guangming Jiang, for your assistance in a lot of experiments. I also would like to thank Dr. Hongwang Zhang, Dr. Yongsheng Yu, Dr. Natalie Huls, Dr. Kai Cheng, Dr. Vismadeb Mazumder, Dr. Don Ho, Dr. Youngmin Li, Dr. Daohua Sun, Dr. Pinxian Xi, Dr. Hao Pang, Dr. Yong Li, Dr. Rui Hao, Dr. Xiaolian Sun, Bo

To my love, HUIYUAN

Abstract of "Synthetic Tuning of Monodisperse Metallic Nanoparticles for Catalytic

Applications" by SEN ZHANG, Ph. D., Brown University, May 2014.

Rational design and controlled synthesis of metallic nanoparticles (NPs) is the key to developing highly efficient and stable catalysts for some new alternative energy conversion and chemical transformation systems such as proton exchange membrane fuel cells. The organic solution based chemical synthesis provides a robust approach to monodisperse metallic NPs with precise control on NP parameters including size, shape, composition and crystal structure etc.. Based on the synthetic tuning on these parameters, the monodisperse metallic NPs can be used for the study of synthesis-catalysis correlation and the optimization of NPs catalytic performance.

This dissertation begins with an overview of the background and fundamental theory of metallic NPs for catalytic applications followed by the introduction of organic solution based chemical synthesis of monodisperse NPs. It further illustrates the synthetic tuning of metallic NPs for catalytic applications by providing several monodisperse metallic NPs catalysts I developed in the past four years. These metallic NPs have been demonstrated to be the advanced catalysts for various catalytic reactions including oxygen reduction reaction (ORR), formic acid oxidation reaction (FAOR), methanol oxidation reaction (MOR) and formic acid dehydrogenation (FAD).

Table of Contents

List of Figures and Tables

Cu atoms. Two models have a core composition of ~$Fe_{25}Cu_{25}Pt_{50}$ and a three-atomic-layer shell of Pt. (C, D) Periodic supercells consisting of 108 atoms used to simulate atomic structure of *fcc*-FeCuPt (C) and *fct*-FeCuPt (D). The blue, purpul and orange balls stand for Pt, Fe and Cu atoms, respectively. 74

cycles of the C-Ag$_{42}$Pd$_{58}$ catalyst in the dehydrogenation of aqueous FA solution (10 mL, 1 M) at 50 ^{o}C. (B) A representative TEM image of the C-Ag$_{42}$Pd$_{58}$ catalyst after the 4th catalytic run.   187

Chapter 1

Background and Fundamental Theory of Metallic Nanoparticles

for Catalytic Applications

1.1 General Introduction of Nanomaterials

One nanometer (nm) is a billionth (10^{-9}) of a meter, and this length is comparable with the size of a cluster of tens of atoms. [1] For example, the DNA molecular has a diameter of around 0.5-2 nm and the red blood cells have the size of 7000-8000 nm. (**Figure 1-1**) Nanomaterials normally refer to materials with at least one dimension that falls into the regime of 1-100 nm, which could be nanoparticles (NPs, 0-dimensional), nanowires/nanorods (NWs/NRs, 1-dimensional) and nanoplates (2-dimensional). The interest in materials in this scale can be traced back to the visionary lecture of "*There's Plenty of Room at the Bottom*" given by Richard Feynman at the American Physical Society meeting at Caltech on December 29, 1959. [2] Since then, more and more research efforts have been dedicated in the field of nanomaterials. Today, "nano" has become ever increasingly popular not only in lab research but also in the industrial applications. A lot of the advanced technologies in electronics, magnetics and so on are related to nanomaterials. For example, the latest Intel processors, with cuter size and smarter performance, are based on the 22 nm technology. [3] **Figure 1-1** also lists a series of representative nanomaterials manmade.

Beyond the miniaturization of materials, nanomaterials are of great appeal due to their unique physical and chemical properties which are dramatically distinct compared to their bulky counterparts. [4-9] One typical example is the quantum dots (QDs). [10-12] With scale-down to nano-regime, the inorganic semiconductor nanocrystals (NCs) (CdSe, GaN, InP ect.) show size-dependent fluorescent emission.

This is because the physical size of the NCs is comparable to or smaller than the natural length scale (Bohr radius) of carrier (electron-hole pair) and then generates a confinement to the carriers in the NCs. Referred to as "quantum effect", this physical confinement leads to atomic-like optical behavior in NCs as the continuous energy bands in the bulky materials become discrete and quantized. [12] Electron transition among the quantized energy levels makes QDs absorb and emit photons with the specific energy level, exhibiting the characteristic narrow and symmetric fluorescent emission. More importantly, the quantum effect is strongly dependent on the physical size of NCs. By simply controlling the monodisperse NCs size, the characteristic fluorescent emission of QDs can be readily tuned. Plus their high resistances to degradation, the inorganic QDs are widely used in optoelectronics (transistors, solar cells, light-emitting diodes) [13-17] and biomedical imaging [18-21].

Another example is the localized surface plasma resonance (SPR) on some noble metallic nanoparticles (NPs) (Au, Ag etc.). [22, 23] Due to the nano-size confinement, the collective oscillation of electrons in the conduction band of NPs can be driven by the electromagnetic field of the incident light, making the NPs show a strong absorption of the visible light. Moreover, this adsorption can also be controlled by the size and shape of NPs. Therefore, Au and Ag NPs can show tunable colors by controlling their size/shape. [24, 25] This unique nanoscale SPR has shown great potentials in biomedical and biosensor applications. [25-28]

Figure 1-1. The scale of things to explain the regime of nanomaterials and the typical natural and artificial examples of nanomaterials. (Courtesy of the Office of Basic Energy Sciences, Office of Science, U.S. Department of Energy, http://www.sc.doe.gov/bes/scale_of_things.html)

Thus far, the nanomaterials and their unique properties have been intensively studied in various applications including magnetic, electronic, biomedical and catalytic applications. [8, 13, 15, 27, 29] To optimize their applications in these fields, NPs

should first be made with controlled dimensions (size, shape, composition and structure) as their physical properties are strongly dimension-dependent. During my PhD study, I specifically centered on the rational design and controlled synthesis of metallic NPs for catalytic applications.

1.2 Metallic Nanoparticles for Catalytic Applications

The first advantage of NPs as catalysts is their much higher surface area than bulk material catalysts. As **Figure 1-2** shows, a cube with an edge of 1 cm has a surface area of 6 cm^2. When it is separated to 10^{12} cubes with the edge of 1 micrometer (μm), the total surface area will be 6 m^2. Further separation to 10^{21} 1-nm-sized cubes, the surface area can reach 6000 m^2. [30] The much increased surface area of NPs can provide abundant interfaces for catalytic reactions, making NPs ideally suitable to be the active electrochemical and heterogeneous catalysts.
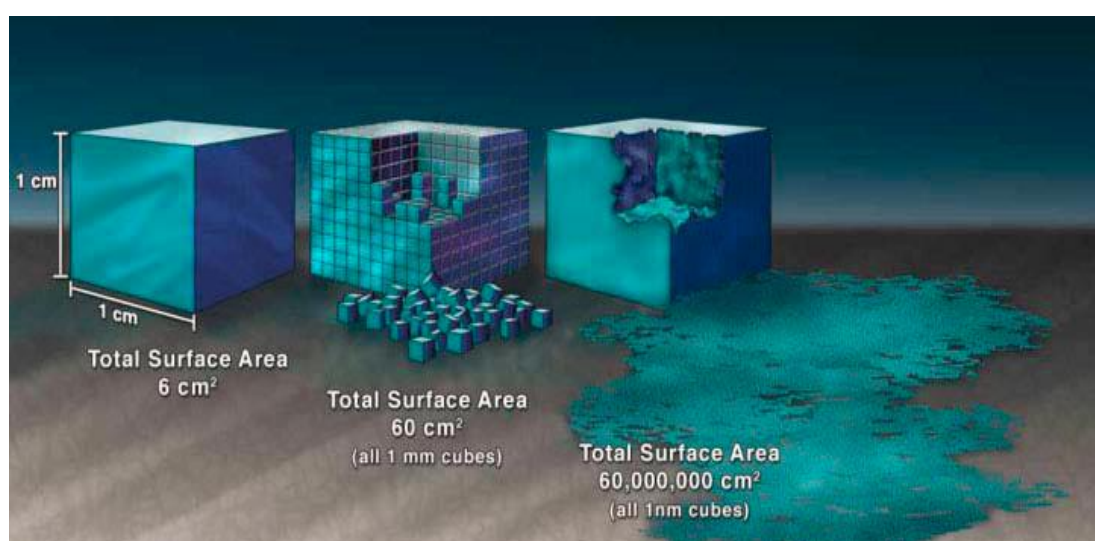
Figure 1-2. Schematic illustration of the nanosize-induced the increase of surface area [30].

Not only the huge surface area does the NPs can achieve, the controlled synthesis of NPs can also provide more opportunity to tailor the catalysis efficiency by tuning the interface energetics. [29] This is because the NPs surface/interface energetics can be governed by the electronic structure and ligand arrangement of NPs which can be realized by the synthetic tuning of NPs size, shape, composition and structures and so on. [29] In my PhD study, those metallic NPs are designed and synthetically tuned for to highly efficiently catalyze the reactions related to electrochemical energy conversion for fuel cells applications and chemical transformations (H_2 generation).

1.2.1 Fuel Cells and Fuel Cells Catalysts

Fuel cells are a common type of energy devices developed for future energy applications. Among various forms of fuel cells designed and tested, proton exchange membrane fuel cells (PEMFCs) are featured by high energy density, low operation temperatures and low environmental impacts, and represent a promising technology to power portable electronic devices, transportation vehicles, and stationary grids. [31, 32] **Figure 1-3** illustrates a typical PEMFC design, in which fuel (hydrogen, H_2) is oxidized at anode and oxygen (O_2) is reduced at cathode, converting the chemical energy stored in H_2 into electric energy. In this fuel cell device, the fuel can be any of hydrogen, methanol, ethanol or formic acid, while highly electronegative O_2 is chosen to receive electrons released from the fuel. [33] To achieve the desired energy

6

output, proton-exchange membrane based on Nafion, a copolymer of tetrafluoroethylene and perfluoro-2-(fluorosulfonylethoxy) propylvinylether, is used to separate the anode and cathode and to allow protons to migrate from anode to cathode to neutralize the reduced oxygen.[34] Overall, *via* a fuel oxidation reaction and oxygen reduction reaction (ORR), electrons flow outside the cell to power electronic devices and protons migrate from anode to cathode inside through Nafion membrane to complete the charge flow in the circuit.[35]
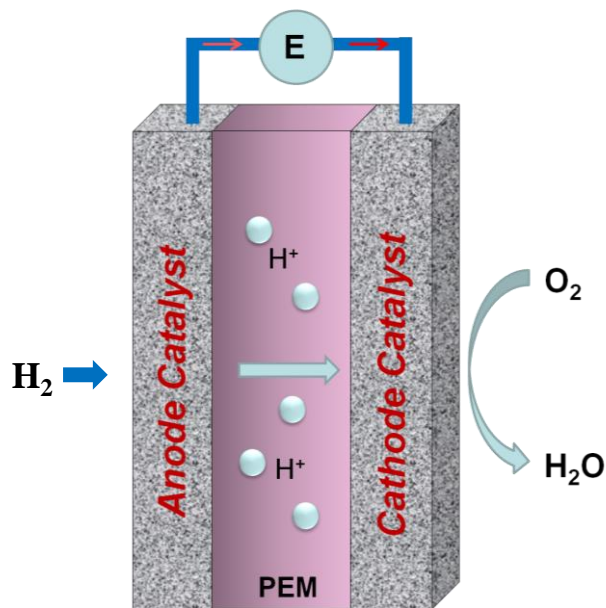
Figure 1-3. Schematic illustration of a typical PEMFC with H_2 as fuel.

Despite their great potential as an efficient device to convert chemical energy into electric energy, PEMFCs do have their own serious limitations that prevent them from being scaled-up for commercial applications.[34] Both the fuel oxidation reaction

and ORR need catalysts to lower their electrochemical over-potentials and to obtain high voltage output; platinum (Pt) has been the universal choice of catalyst for both reactions.[36, 37] However, Pt is not a cheap metal for practical use - the industrial ORR catalyst with small Pt nanoparticles (NPs) supported on carbon takes over 55 % cost of a fuel cell stack. [32] Furthermore, Pt NPs are subject to dissolution, coalescence, and poisoning in fuel cell reaction conditions, reducing both catalyst active surface area and efficiency that leads to undesired increase in over-potentials for fuel cell reactions, especially for ORR.[38-42] Today, the life time of the state-of-art Pt catalyst maintaining high fuel cell performance is far shorter than the 5000 h set as the year 2017 target by the US Department of Energy (DOE).[43] The high cost and limited catalyst life time have posed tremendous challenges in developing Pt-based catalysts for practical fuel cell applications, and new innovative approach to highly efficient fuel cell catalysts is now desperately needed.

1.2.2 Cathodic Reaction: Oxygen Reduction Reaction (ORR)

The ORR is a complex reduction process involving multiple electrons. [44] Highly electronegative O_2 at the cathode functions as an electron sink to initiate fuel oxidation at anode and O_2 itself is converted into H_2O or OH^- depending on electrolytes used in electrochemical studies. In an acidic solution (either $HClO_4$ or H_2SO_4 for example), O_2 can be reduced in a $4e^-$ process and converted to H_2O: $O_2 + 4H^+ + 4e^- \rightarrow 2H_2O$. O_2 may also undergo a partial $2e^-$ reduction to hydrogen peroxide,

H_2O_2, followed by another $2e^-$ reduction to convert H_2O_2 to H_2O: $O_2 + 2H^+ + 2e^- \rightarrow$

H_2O_2; $H_2O_2 + 2H^+ + 2e^- \rightarrow 2H_2O$. In an alkaline solution (KOH is often used), O_2 can

be reduced via a $4e^-$ process to form hydroxide, OH^-: $O_2 + 2H_2O + 4e^- \rightarrow 4OH^-$, or

via two 2e- processes to form HO_2^- and then OH^-: $O_2 + H_2O + 2e^- \rightarrow HO_2^- + OH^-$;

$HO_2^- + H_2O + 2e^- \rightarrow 3OH^-$. [45] In the common acid and alkaline solutions, ORR on a

Pt catalyst follows the $4e^-$ pathway. The commonly accepted O_2 activation

mechanism on Pt involves O_2 adsorption, O-O bond activation and O-H bond

formation, as illustrated in **Figure 1-4.**[46]

$$O_2 \longrightarrow O_2^* \qquad\qquad (1)$$

$$O_2^* \longrightarrow O^* + O^* \qquad\qquad (2)$$

$$O^* + O^* + (H^+ + e^-) \longrightarrow OH^* + O^* \qquad\qquad (3)$$

$$OH^* + O^* + (H^+ + e^-) \longrightarrow H_2O + O^* \qquad\qquad (4)$$

$$H_2O + O^* + (H^+ + e^-) \longrightarrow H_2O + OH^* \qquad\qquad (5)$$

$$H_2O + OH^* + (H^+ + e^-) \longrightarrow 2H_2O \qquad\qquad (6)$$
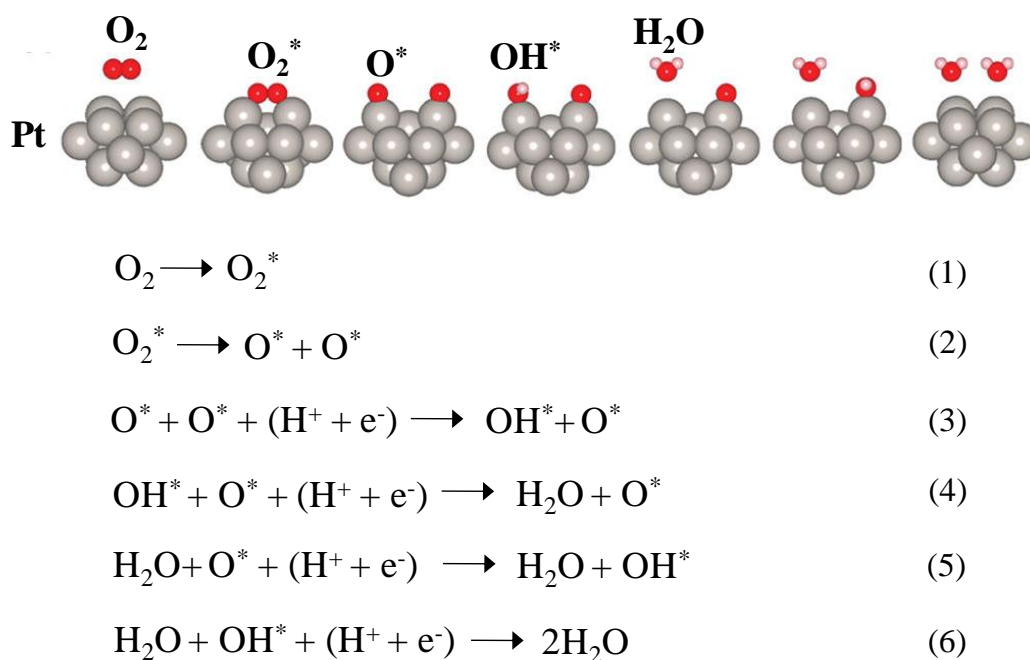
Figure 1-4. The proposed catalytic mechanism of O_2 reduction on Pt catalyst in an acid solution. Reprinted from Ref. 46 with permission by American Chemical Society.

Although the whole ORR process is very complicated and elusive, it can be

summarized as the adsorption and desorption of oxygenated intermediate species (O^*,

OH*, OOH* etc.). Therefore, ORR dynamics can be determined by the surface oxygen adsorption energy (E_o) of a catalyst, which describes the bonding capability of a catalyst to oxygenated intermediate species. [47] Recently, some theoretical calculations have concluded that the E_o should be in a proper level to support the favorable dynamics of ORR on the electrochemical interface, where the bonding of oxygenated species is neither too strong nor too weak. [48, 49] As a result of ideal E_0, the adsorption and desorption of catalytic intermediate, two contradictory processes, are perfectly balanced. The pure Pt have too strong bonding with oxygenated species, providing a surface undesirable to desorption and exhibiting low ORR catalysis (large over-potential). [48, 49] To enhance the ORR dynamics on Pt NPs, this over-strong adsorption has to be lowered to the proper level.

To perform electrochemical evaluation on ORR, the NP catalyst is usually dispersed in a mixture of water, isopropanol and Nafion (5%) with a volume ratio of 4:1:0.025%, and deposited on a glassy carbon (GC) rotating disk electrode (RDE). [50] Depending on the area of the RDE used, the Pt loading amount is controlled in a range from 10 to 50 $\mu g/cm^2$ to ensure a thin layer of NP deposition on the electrode surface. [50] More catalyst loading can lead to the formation of an overly thick (> 1 μm) catalyst agglomerate, resulting in excessive mass-transport loss [50, 51] and a large uncertainty in qualifying catalytic activities. [52, 53]

Electrochemical properties of the catalyst in an N_2- or Ar-saturated acid solution (either 0.1 M $HClO_4$ or 0.5 M H_2SO_4) are first studied by cyclic voltammetry to

obtain cyclic voltammogram (CV) and to determine the electrochemically active surface area, ECASA, of the Pt catalyst. In a cathodic scanning process, H^+ is first reduced into H_2 that is absorbed on the catalyst surface and the related area under the current (I) – potential (V) curve is often referred to as H_2 absorption region. The absorbed H_2 is oxidized in an anodic scanning process, regenerating H^+, and the related area covered by I-V curve is referred to as H_2 desorption region. The H_2 desorption area surrounded by the I-V curve and the potential scanning base line is integrated to obtain ECASA.[54] In the calculation, electric charge is assumed to be 210 mC/cm^2 Pt after double-layer correction.[55] ORR activities are measured in an O_2-saturated acid or alkaline solution with the RDE rotating at a certain speed (usually 1600 rpm) and potential sweeping from 1.05 to 0 V (vs. reversible hydrogen electrode, RHE) at rates ranging from 5 to 20 mV/s to minimize the interference from capacitive currents. From the ORR polarization curves of two kinds of catalysts under the same Pt loading and measurement condition, the half-wave potential ($E_{1/2}$) of these two catalysts can be obtained and used to determine the catalyst activity qualitatively, see **Figure 1-5**. The higher the number, the better the ORR activity is. For a more quantitative comparison, the kinetic current at 0.9 V (vs. RHE) is first obtained from ORR polarization curve according to the Levich-Koutecky equation: [50, 51]

$$1/i = 1/i_k + 1/i_d \qquad (7)$$

where i is the current obtained experimentally, i_k is the mass-transport free kinetic

current and i_d is the diffusion-limited current, as indicated in **Figure 1-5**. Specific activity can be determined via calculation of i_k using equation (1) and then normalized with the Pt ECASA. From the same experimental data, one can also determine the mass activity of the catalysts via i_k normalization to the Pt loading amount. Through direct comparison between specific and mass activities of two different catalysts, the efficiency of the new catalyst can be evaluated.
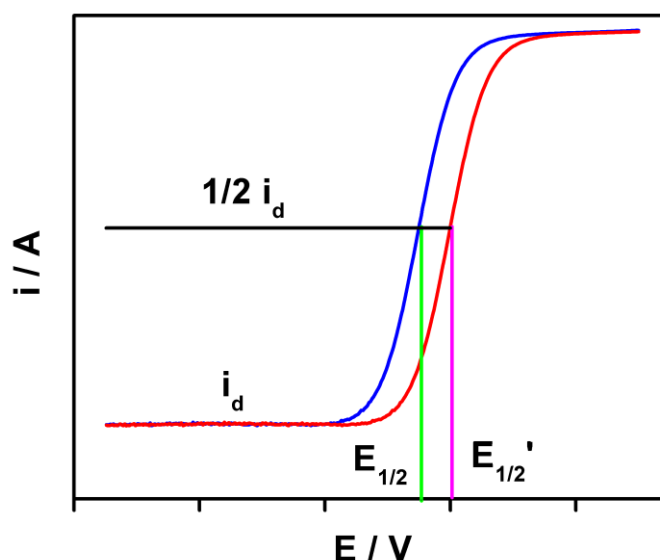
Figure 1-5. Typical ORR polarization curves of two different catalysts and the parameters used to compare qualitatively the activity of these two catalysts.

The catalyst durability is tested by cycling the potentials from 0.6 to 1.05 V (*vs.* RHE) in O_2-saturated 0.1 M $HClO_4$ or 0.5 M H_2SO_4 solution. More than 4000 cycles are now routinely used in the literature and the shift of ORR polarization curve and the NP morphology, and therefore ECASA, change before and after these potential cycles are compared to measure the durability of the NP catalyst. The smaller the

shift and NP morphology (ECASA) change, the better the durability. In alkaline solution, time (t) dependent current (i) curve (i-t curve) at a constant potential (usually half-wave potential) is usually used to estimate and compare the stability of catalysts.[56, 57]

Synthetic tuning of metallic NPs for ORR catalysis is one of the main components of my dissertation. In chapter 3-4, I will introduce a new structure-control strategy to optimize the ORR activity and durability of the bimetallic FePt and trimetallic FeCuPt NPs. In chapter 5, I will be focused on the shape effect of NPs catalysts for ORR, where the FePtCu and FePtNi nanorods are synthetically tuned and systematically studied. In chapter 6, non-Pt metallic Co NPs will be discussed as another class of catalyst for the ORR in the alkaline condition.

1.2.3   Anodic Reaction: Formic Acid and Methanol Oxidation Reactions

Considering the difficult purification, transfer and storage of hydrogen (H_2), a great deal of emphasis have been placed on fuels of small organic molecules in PEMFCs studies. Formic acid (HCOOH), a promising choice of fuel, has attracted growing attention due to their facile power-system integration, low cross-over flux through Nafion membranes (fuel molecule diffusion to cathode side to interfere ORR, which is negligible for HCOOH because of electrostatic repulsion of HCOO- and sulfo group in Nafion), and convenient storage and transport of liquid formic acid. [58] The formic acid oxidation reaction (FAOR) usually requires a Pd or Pt-based nanocatalyst.

Pd-based nanocatalyst shows the good catalytic activity for formic acid oxidation reaction (FAOR), but its high performance cannot be sustained in the long term because of its easy dissolution in acidic solutions and the vulnerability towards intermediate species. [58] Comparing to Pd-based nanocatalyst, Pt nanocatalyst is believed to be much stable in acidic solution; however, its FAOR activity is restrained by so-called "CO poisoning". [59, 60] **Figure 1-6A** shows a cyclic voltammograms (CVs) of Pt NPs in the FAOR condition. In the forward scan which is normally used to indicating the oxidation reactions, there are two peaks. This is because the formic acid can be oxidized in two paths, a dehydrogenation path and a dehydration path. (**Figure 1-6B**) The low-potential oxidation peak (P_1) is intimately related to the direct FAOR to CO_2 *via* dehydrogenation path while the high-potential oxidation peak (P_2) corresponds to the oxidation of the absorbed CO generated from dehydration path (**Figure 1-6A**). Since the Pt can easily catalyze the formic acid dehydration and CO can adsorb on Pt-surface strongly, the most of surface active site of Pt will be blocked by CO. As a result, the FAOR acitivity (P_1) is very weak, but at the CO-oxidation potential (P_2) there is a huge current which is useless for an anodic reaction in fuel cells (anode has a negative potential than cathode). The ultimate goal for Pt-based nanocatalyst is to complete eliminate the CO poisoning for stimultaneous enhancement in both activity and durability.

(B)

Pathway I: dehydrogenation (direct FAOR, desirable)
$$HCOOH \longrightarrow CO_2 + 2H^+ + 2e^- \text{ (low potential)}$$
Pathway II: Dehydration (indirect, undesirable)
$$HCOOH \longrightarrow CO + H_2O$$
$$\longrightarrow CO_2 + 2H^+ + 2e^- \text{ (high potential)}$$
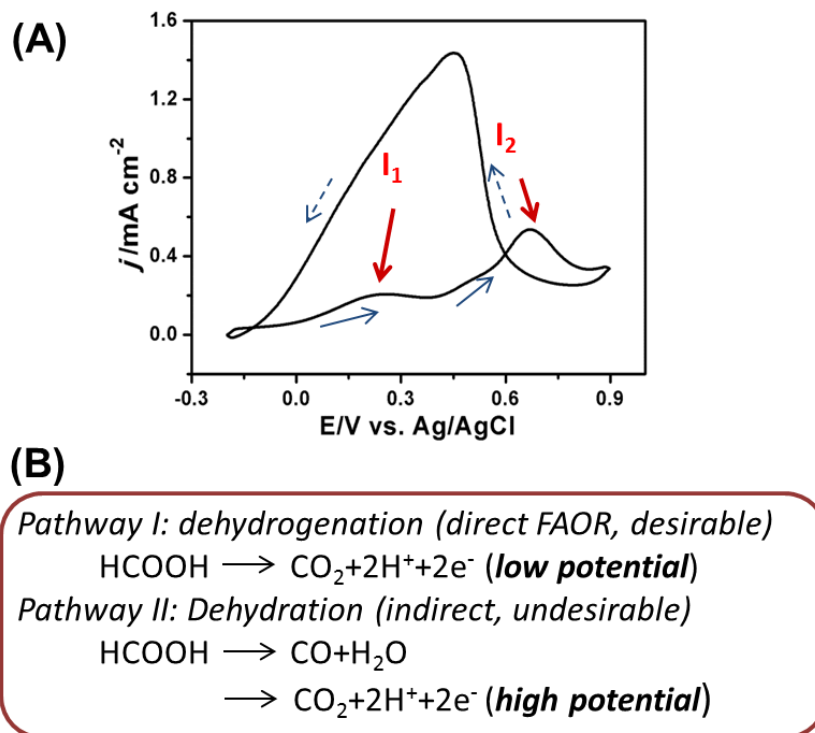
Figure 1-6. (**A**) CVs of FAOR on commercial Pt NPs. (**B**) The dual FAOR pathways on Pt NPs.

Previous effort to eliminate the CO-poisoning on Pt surface is to alloy Pt with other foreign metals such as Bi, Pb etc.. [59, 61] These alloy NPs with composition effect change the electronic structure and ligand condition of Pt which can suppress the formation of CO. In my graduate study, I have looked at the structural tuning of trimetallic FePtAu NPs beyond composition effect for the highly efficient FAOR catalysis, which have been demonstrated in Chapter 7 as the most active and durable NPs catalysts for FAOR.

Methanol oxidation reaction (MOR) is another very important anodic reaction studied for PEMFCs. One advantage of methanol (CH_3OH) fuel is its higher energy density (4690 kW/L) than formic acid (2086 kW/L) and hydrogen (2300 kW/L). [62]

The NPs, normally Pt-based NPs, can catalyze MOR to generate the CO_2 and protons, as show in equation 8.

$$CH_3OH + H_2O \longrightarrow CO_2 + 6H^+ + 6e^- \qquad (8)$$

To optimize the MOR on Pt-based NPs, a three step mechanism has to be mentioned, which includes: (I) dehydrogenation of methanol to CO, (II) dehydrogenation of water to O, (III) oxidative recombination of CO and O to form CO_2 followed by product desorption. [62, 63] Mechanism study points out that the Pt is active for methanol dehydrogenation, but poor for water dehydrogenation, leading to CO accumulation and slow dynamics of MOR. [62-64] To enhance the MOR catalysis, Pt has been selectively alloyed with some metals (Ru, Pd etc.) that are favorable for water dehydrogenation. [65, 66] In this thesis, I introduce an approach that combined the alloy strategy with NPs shape control to generate 1-dimentional FePtPd nanowires for a new kind of highly active and durable catalysts for MOR (Chapter 8).

1.2.4   Metallic NPs Heterogeneous Catalysts for Chemical Transformations

The hydrogen is a very important chemical in various applications. It can be used as a fuel at the anode of PEMFCs. It is also the key precursor or reducing agent in chemical industries such as fossil fuel processing and ammonium production. All these hydrogen economics, especially PEMFCs, strongly relies on the storage and utilization of H_2 in high purity and in facile conditions. Hydrogen produced by traditional hydrocarbon reforming in industry always has a small amount of CO

contamination, which is unacceptable in current PEMFCs and other industries with Pt as catalysts. Also considering the convenient usage of H_2, a great deal of research effort has been devoted to find a suitable hydrogen storage material which can store and release high purity H_2 in controlled conditions. [67, 68]

In my study, I have been focused on the formic acid dehydrogenations (FAD) in water solution and facile condition, as indicated in equation 9. [67]

$$HCOOH \longrightarrow CO_2 + H_2 \qquad (9)$$

To study FAD, we developed a self-designed set-up as shown in **Figure 1-7**, in which the evolution of H_2 along with reaction time will be studied. Based on this simple set-up, I have studied the synthetic tuning of AgPd alloy NPs for FAD, which has been demonstrated as the most active NP heterogeneous catalysts for FAD in water condition (Chapter 9).
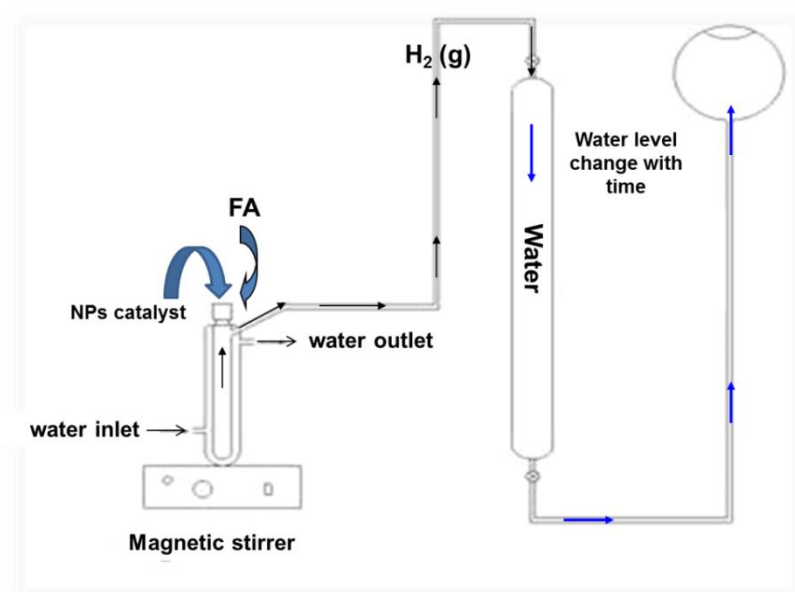
Figure 1-7. The illustration of the self-designed setup for FAD catalysis investigation.

Reference:

1. S. E. McNeil, J. Leukoc. Biol. **2005**, *78*, 585-594.

2. R. P. Feynman, *Eng. Sci.* **1960**, *23*, 22-27.

3. "3-D, 22nm: New Technology Delivers An Unprecedented Combination of Performance and Power Efficiency", *Intel* webpage: http://www.intel.com/content/www/us/en/silicon-innovations/intel-22nm-technology.html

4. G. A. Ozin, L. Cademartiri, *Nanochemistry: Principles and Practice*, Wiley-VCH **2009**.

5. C. N. R. Rao, A. Müller, A. K. Cheetham, *The Chemistry of Nanomaterials*, Wiley-VCH Verlag GmbH & Co. KGaA, **2005**.

6. S. C. Tjong, *Nanocrystalline Materials*, Elsevier Science Ltd, Oxford, **2006**.

7. S. Zhang, J. Lee, S. Sun, *The Open Sur. Sci. J.***2012**, *4*, 26-34.

8. N. A. Frey, S. Peng, K. Cheng, S. Sun, *Chem. Soc. Rev.* **2009**: *38*: 2532-2542.

9. C. M. Niemeyer, C. A. Mirkin, *Nanobiotechnology: Concepts, Applications and Perspectives*, Wiley-VCH, **2004**.

10. C. B. Murray, D. J. Norris, M. G. Bawendi, *Journal of the American Chemical Society* **1993**, *115*, 8706-8715.

11. C. B. Murray, C. R. Kagan, M. G. Bawendi, *Annu. Rev. Mater. Sci.* **2000**, *30*, 545-610.

12. V. I. Klimov, *Nanocrystal Quantum Dots*, CRC Press, Taylor and Francis Group, LLC. 2010.

13. V. Talapin, J.-S. Lee, M. V. Kovalenko, E. V. Shevchenko, *Chem. Rev.* **2010**, *110*, 389-458.

14. V. L. Colvin, M. C. Schlamp, P. A. Alivisato, *Nature* **1994**, *370*, 354-357.

15. E. H. Sargent, *Nat. Photon.* **2012**, *6*, 133-135.

16. J. Tang, K. W. Kemp, S. Hoogland, K. S. Jeong, H. Liu, L. Levina, M. Furukawa, X. Wang, R. Debnath, D. Cha, K. W. Chou, A. Fischer, A. Amassian, J. B. Asbury, E. H. Sargent, *Nat. Mater.* **2011**, *10*, 765-771.

17. Y. Shirasaki, G. J. Supran, M. G. Bawendi, V. Bulovic, *Nat. Photon.* **2013**, *7*, 13-23.

18. M. Bruchez, M. Moronne, P. Gin, S. Weiss, P. A. Alivisatos, Science **1998**, *281*, 2013-2016.

19. W. C. W. Chan, S. Nie, Science **1998**, *281*, 2016-2018.

20. I. L. Medintz, H. T. Uyeda, E. R. Goldman, H. Mattoussi, *Nat. Mater.* **2005**, *4*, 435.

21. P. Alivisatos, *Nat. Biotech.* **2004**, *22*, 47-52.

22. K. M. Mayer, J. H. Hafner, *Chem. Rev.* **2011**, *111*, 3828-3857.

23. M. B. Cortie, A. M. McDonagh, *Chem. Rev.* **2011**, *111*, 3717-3735.

24. Q. Zhang, J. Ge, T. Pham, J. Goebl, Y. Hu, Z. Lu, Y. Yin, *Angew. Chem. Int. Ed.* **2009**, *48*, 3516-3519.

25. Y. Xia, Y. Xiong, B. Lim, S. E. Skrabalak, *Angew. Chem. Int. Ed.* **2009**, *48*, 60-103.

26. L. He, M. D. Musick, S. R. Nicewarner, F. G. Salinas, S. J. Benkovic, M. J. Natan, C. D. Keating, *J. Am. Chem. Soc.* **2000**, *122*, 9071-9077.

27. E. Dreaden, X. Huang, A. M. Alkilany, C. J. Murphy, M. A. El-Sayed, *Chem. Soc. Rev.* **2012**, 41, 2740-2779.

28. C. J. Murphy, *Nat. Mater.* 2007, 6, 259-260.

29. S. Guo, S. Zhang, S. Sun, *Angew. Chem. Int. Ed.* **2013**, DOI: anie.201207186.

30. *What's so special about the nanoscale? Vol. 2011*, The United States National Nanotechnology Initiative, **2011**.

31. R. Borup, J. Meyers, B. Pivovar, Y. S. Kim, R. Mukundan, N. Garland, et al. *Chem. Rev.* **2007**, *107*, 3904-3951.

32. Y.-J. Wang, D. P. Wilkinson, J. Zhang, *Chem. Rev.* **2011**, *111*, 7625-7651.

33. Z. Chen, D. Higgins, A. Yu, L. Zhang, J. Zhang, *Energy Environ. Sci.* **2011**, *4*, 3167-3192.

34. Y. Bing, H. Liu, L. Zhang, D. Ghosh, J. Zhang, *Chem. Soc. Rev.* **2010**, *39*, 2184-2202.

35. D. S. Su, G. Sun, *Angew. Chem. Int. Ed.* **2011**, *50*, 11570-11572.

36. J. Chen, B. Lim, E. P. Lee, Y. Xia, *Nano Today* **2009**, *4*, 81-95.

37. S. Guo, E. Wang, *Nano Today* **2011**, *6*, 240-264.

38. Z. Chen, M. Waje, W. Li, Y. Yan, *Angew. Chem. Int. Ed.* **2007**, *46*, 4060-4063.

39. C. Koenigsmann, A. C. Santulli, K. Gong, M. B. Vukmirovic, W.-P. Zhou, E. Sutter, S. S. Wong, R. R. Adzic, *J. Am. Chem. Soc.* **2011**, *133*, 9783-9795.

40. C. Koenigsmann, E. Sutter, T. A. Chiesa, R. R. Adzic, S. S. Wong, *Nano Lett.* **2012**, *12*, 2013-2020.

41. C. Koenigsmann, E. Sutter, R. R. Adzic, S. S. Wong, *J. Phys. Chem. C* **2012**, *116*, 15297-15306.

42. S. Sun, G. Zhang, D. Geng, Y. Chen, R. Li, M. Cai, X. Sun, *Angew. Chem. Int. Ed.* **2011**, *50*, 422-426.

43. U. S. D. O. Energy,

http://www1.eere.energy.gov/hydrogenandfuelcells/mypp/pdfs/fuel_cells.pdf.

44. (a) M. R. Tarasevich, A. Sadkowski, E. Yeager, in Comprehensive Treatise of Electrochemistry, Vol. 7 (Eds: B. E. Conway, J. O. Bockris, E. B. Yeager, R. E. White), Plenum, New York 1983, pp. 301; (b) D. Yu, E. Nagelli, F. Du, L. Dai, *J. Phys. Chem. Lett.* **2010**, *1*, 2165-2173; (c) J. Zhang, K. Sasaki, E. Sutter, R. R. Adzic, *Science* **2007**, *315*, 220-222.

45. Y. Zheng, Y. Jiao, M. Jaroniec, Y. Jin, S. Z. Qiao, *Small* **2012**, *8*, 3550-3566.

46. D.-H. Lim, J. Wilcox, *J. Phys. Chem. C* **2012**, *116*, 3653-3660.

47. X. Zhang, G. Lu, W. A. Curtin, *Phys. Rev. B* **2013**, *87*, 054113.

48. V. Stamenkovic, B. S. Mun, K. J. J. Mayrhofer, P. N. Ross, N. M. Markovic, J. Rossmeisl, J. Greeley, J. K. Nørskov, *Angew. Chem. Int. Ed.* **2006**, *45*, 2897-2901.

49. J. K. Nørskov, J. Rossmeisl, A. Logadottir, L. Lindqvist, J. R. Kitchin, T. Bligaard, H. Jonsson, *J. Phys. Chem. B* **2004**, *108*, 17886-17892.

50. H. A. Gasteiger, S. S. Kocha, B. Sompalli, F. T. Wagner, *Applied Catalysis B: Environmental* **2005**, *56*, 9-35.

51. T. J. Schmidt, H. A. Gasteiger, Rotating thin-film method for supported catalysts, in: W. Vielstich, H. Gasteiger, A. Lamm (Eds.), Handbook of Fuel Cells-Fundamentals, Technology and Applications, **2003**, *2*, 316-333.

52. F. Gloaguen, P. Convert, S. Gamburzev, O. A. Velev, S. Srinivasan, *Electrochim. Acta* **1998**, *43*, 3767-3772.

53. J. Perez, E.R. Gonzalez, E.A. Ticianelli, *Electrochim. Acta* **1998**, *44*, 1329-1339.

54. B. Lim, M. Jiang, P. H. C. Camargo, E. C. Cho, J. Tao, X. Lu, Y. Zhu, Y. Xia, *Science* **2009**, *324*, 1302-1305.

55. T. J. Schmidt, H. A. Gasteiger, G. D. Stäb, P. M. Urban, D. M. Kolb, R. J. Behm, *J. Electrochem. Soc.* **1998**, *145*, 2354-2358.

56. S. Wang, D. Yu, L. Dai, *J. Am. Chem. Soc.* **2011**, *133*, 5182-5185.

57. S. Wang, D. Yu, L. Dai, D. W. Chang, J.-B. Baek, *ACS Nano* **2011**, *5*, 6202-6209.

58. X. Yu, P. G. Pickup, *J. Power Sources* **2008**, *182*, 124-132.

59. X. Ji, K. T. Lee, R. Holden, L. Zhang, J. Zhang, G. A. Botton, M. Couillard, L. F. Nazar, *Nat. Chem.* **2010**, *2*, 286-293.

60. S. Zhang, S. Guo, D. Su, S. Sun, *J. Am. Chem. Soc.* **2012**, *134*, 5060-5063.

61. Y. Kang, L. Qi, M. Li, R. E. Diaz, D. Su, R. R. Adzic, E. Stach, J. Li, C. B. Murray, *ACS Nano* **2012**, *6*, 2818-2825.

62. A. Chen, P. Holt-Hindle, *Chem. Rev.* **2010**, *110*, 3767–3804.

63. J. Kua, W. A. Goddard, *J. Am. Chem. Soc.* **1999**, *121*, 10928-10941.

64. B. C. H. Steele, A. Heinzel, *Nature* **2001**, *414*, 345-352.

65. M. Watanabe, S. Motoo, *J. Electroanaly. Chem.* **1975**, *60*, 275-283.

66. Y. Liu, M. Chi, V. Mazumder, K. L. More, S. Soled, J. D. Henao, S. Sun, *Chem. Mater.* **2011**, *23*, 4199-4203.

67. Ö. Metin, X. Sun, S. Sun, *Nanoscale* **2013**, *5*, 910-913.

68. S. Zhang, Ö. Metin, D. Su, S. Sun, *Angew. Chem. Int. Ed.* **2013**, *52*, 3681-3684.

Chapter 2

Chemical Synthesis and Characterization of Monodisperse Nanoparticles: Theory and General Experimental section

In chapter 1, I have discussed the great potential of nanoparticles (NPs) in various catalytic applications. To achieve any of these application goals, the size, composition, shape and structure of these NPs must be first controlled so that their catalytic properties can be specifically tuned. Recent advances in high temperature organic solution synthesis have led to the formation of various NPs with the desired dimension controls. This chapter starts with a brief introduction of synthetic theory in the high temperature organic solution synthesis of metallic NPs. It further illustrates the general experimental including set-up, NPs collection and purification. The NPs characterizations are also summarized to provide a general overview of analysis and evaluation on NPs morphology, structure and catalytic properties.

2.1 Organic Solution Synthesis to Monodisperse Nanoparticles

To facilitate systematic study of various applications, monodisperse (narrow size distribution in diameter with standard deviation less than 10%) nanoparticles (NPs) are highly desirable with precise control of parameters such as size, shape, composition and crystalline structure etc.. [1] These monodisperse NPs allow the unambiguous study of parameter-property correlation and are ideal platforms to optimize the catalytic applications.

During past decades, organic solution phase reactions in high temperature have been proven to be ideal for synthesizing NPs in high quality. [2-5] In the synthesis, the NPs are generally formed via nucleation and growth processes, as referred to as La Mer model (**Figure 2-1**). [6] The metal precursor, normally metal salt or organometallic complex (e.g. metal acetate, metal acetylacetonate, metal chloride and metal carbonyl etc.) is decomposed and reduced in high boiling-point organic solvents (e.g. benzyl ether, phenyl other, 1-octadecene etc.). To control NP nucleation and growth, the metal precursor is either "hot-injected" into the pre-heated solvent or pre-mixed with other surfactants in the organic solvent followed by heating. The nucleation happens when the rapid decomposition/reduction of metal precursors at high temperature yields an over-supersaturated atomic monomer solution in a short interval, which is called "burst nucleation". This burst nucleation consumes most monomers and prevents any further nucleation. The nuclei then grow up to monodisperse NPs at the same rate, depleting the rest of monomers.
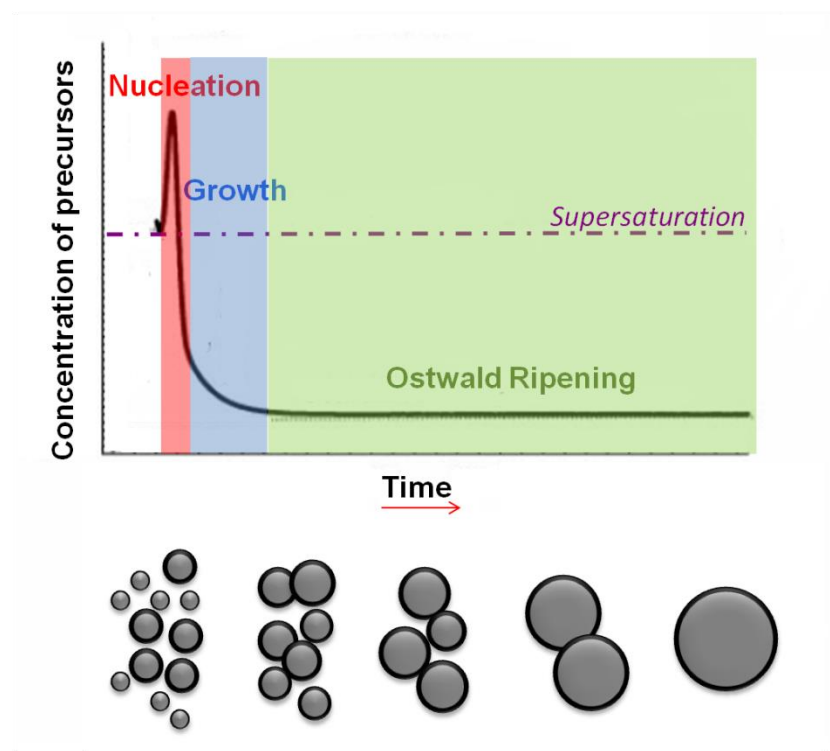
Figure 2-1. Schematic illustration of general chemistry for the preparation of monodisperse NPs.

During the aging of NPs in the synthesis, a self-regulating process called Ostwald ripening occurs. [7] This is caused by the fact that large NPs with less surface atoms are more thermodynamically stable than smaller NPs. Consequently, surface atoms of small NPs are subject to dissolve back the solution and then grow onto the larger NPs. Therefore, the NPs number will decrease until all the resultant NPs have the similar size, helping the formation of monodisperse NPs.

Due to the presence of large percentage of surface atoms that are chemically unsaturated on NP surface, NPs formed during the synthesis often have large surface energy and are prone to aggregation. To stabilize NPs from this aggregation, lipid-type surfactant molecules are normally used to react with surface atoms so that

these atoms can be passivated and NPs can be stabilized. The bipolar surfactant always has a polar group binding with the surface atoms and a hydrocarbon chain to provide steric protection of the NPs. Oleic acid and oleylamine are the common surfactant choices for this purpose. These surfactant-capped NPs can form very stable dispersion in a non-polar solvent such as hexane. On the other hand, surfactants are often used to control NP size and shape in the synthesis due to the slight binding difference between a surfactant molecule and the crystal facet. [8, 9]

It is still challenging to provide a versatile approach for all the metallic NPs. Depending on the nature of each specific metal, the effective synthetic route to different metallic NPs can be changed dramatically, which is still more of an art rather than science in current stage. [8] Fortunately, a lot of previous study in thin-film and bulk materials endowed us with the principles of designing catalytic metallic materials as introduced in Chapter 1. [10, 11] With these highly valuable design views, I tune the metallic NPs in my synthesis by controlling the reaction conditions (temperature, heating rate, reaction time etc.) and precursor/surfactant choice and so on in hope of fabricating desired NPs for highly performance catalytic applications.

2.2 General Experimental Section

2.2.1 Synthesis Set-up
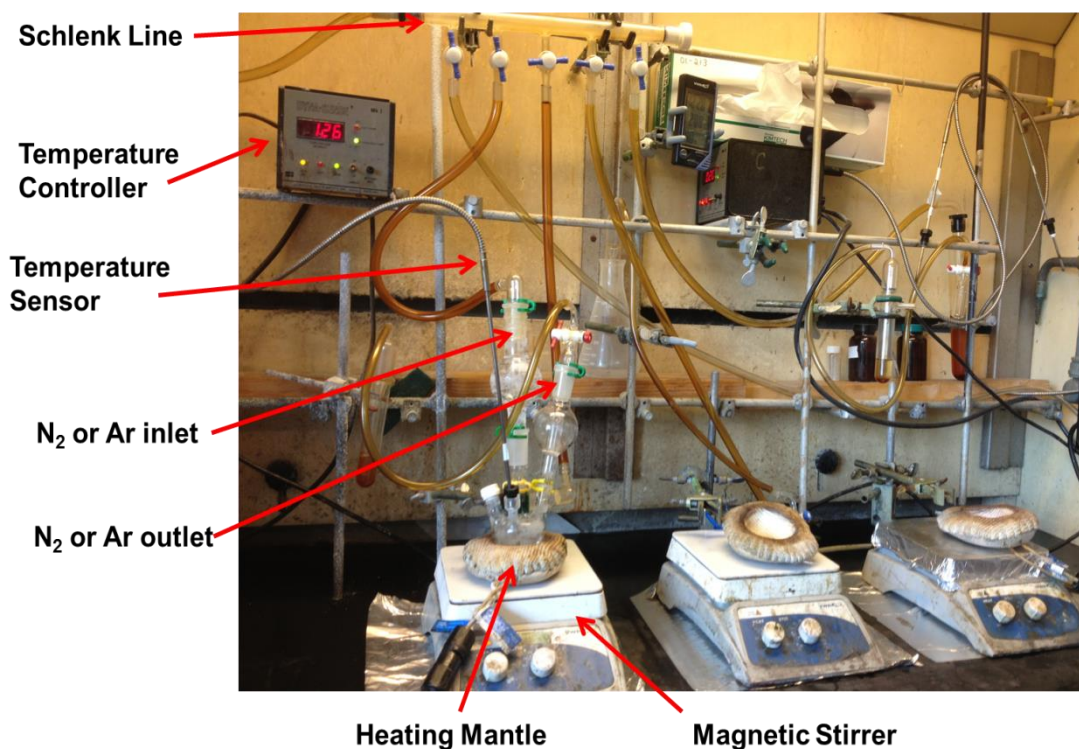
Figure 2-2. General set-up used to synthesize NPs in Sun group. Picture was taken in Geochem 309 with permission from Sun group.

Figure 2-2 shows a typical experimental set-up for high temperature organic solution synthesis of NPs. The reaction is generally carried out in a four neck flask integrated into a standard Schlenk line with inert gas protection (N_2 or Ar). The N_2 or Ar runs through the reaction system in sequence of a self-washing rotary evaporator gas inlet, flask and then a rotary trap gas outlet. This inert gas flow can also serve to blow off any low boiling point impurities and byproducts which can be collected in the rotary trap gas outlet. The reaction solution is stirred by a Teflon coated magnetic bar driven by a magnetic hotplate stirrer (VWR®, 620-HPS). The reaction temperature is governed by a digital temperature controller (Dyna-Sense®, VWR)

coupled with a hemispherical heating mantle (80W-115V, Ace Glass, Inc.), a precision platinum RTD temperature sensor, and a variable transformer with a voltage output range 0-140 V (Ace Glass, Inc.).

2.2.2 Chemicals

Most of chemicals used in the organic solution synthesis are ordered from Strem Chemicals Inc. and Sigma-Aldrich Co., and are used as received without any further purification unless otherwise stated. The air-sensitive and vapor-toxic chemicals such as iron pentacarbonyl ($Fe(CO)_5$) are stored in Ar-filled glove box (Vacuum Atmospheres Co. Omni-Lab glove box, ~0.2ppm O_2 and ~0.5ppm moisture) and are transferred using sealed syringe in well-ventilated hood. The combustible compounds such as hydride compounds are operated with special attention and stored in Ar-filled glovebox at low temperature. Details of the chemicals are provided in the experimental section of each chapter.

2.2.3 Nanoparticle Product Collection and Purification

The as-synthesized NPs are stabilized by the lipid-type surfactant and are well-dispersed in nonpolar solvent (hexane, chloroform, tetrohydrofuran etc.). Adding the excess amount of polar solvent (ethanol, isopropanol, acetone etc.) causes the agglomeration of NPs, which can be easily separated by centrifugation (2000 - 10,000 rpm, Allegra® 64R from Beckman Coulter). The collected NPs can be

re-dispersed in the nonpolar solvent by shaking, sonication (Branson 5510 Sonicator) or ortexing (MiniVortex, VWR). To remove any of the reaction residual and impurities, the agglomeration-centrifugation-redispersion processes are normally repeated several times. The NPs hexane dispersion is stored for future characterizations. For air-sensitive NPs, the dispersion should be stored in glovebox filled with Ar for long-term chemical stability.

2.3 Nanoparticle Characterization

2.3.1 Transmission Electron Microscopy (TEM)

TEM images are used to analyze the morphology of NPs. They are carried out on a Philips FEI CM20 (200 kV) at Brown University. Samples for TEM analysis were prepared by depositing a single drop of diluted NP dispersion in hexane on a Formvar/carbon coated copper grid (Ted Pella, Inc., 01754-F).

2.3.2 High Resolution Transmission Electron Microscopy (HRTEM)

The HRTEM technique is important to analyze the atomic structure of the single NP, such as lattice fringe. The most of HRTEM images are obtained with JEOL 2010 (200 kV) at Brown University. Some HRTEM images are obtained using a JEOL 2100F (200 kV) with a field-emission electron source and a FEI Titan 80-300 (300 kV) with an aberration (image) corrector in the Center for Functional Nanomaterials at Brookhaven National Lab. The samples are prepared in the same way as TEM

samples.

2.3.3 High-Angle Annular Dark-Field Scanning TEM (HAADF-STEM), STEM-Electron Energy-Loss Spectroscopy (STEM-EELS) and STEM-Energy Dispersive X-ray Spectroscopy (STEM-EDS)

HAADF-STEM images and STEM-EELS and STEM-EDS analysis are carried out using a Hitachi HD2700C (200kV) with a probe aberration-corrector, in the Center for Functional Nanomaterials at Brookhaven National Lab. The STEM analysis can provide the delicate atomic elemental distribution and structural information of single NP. Samples were prepared by depositing a single drop of diluted NP dispersion in hexane on an ultrathin carbon (<3nm)/holey support film coated copper grid (Ted Pella, Inc., 01824).

2.3.4 Scanning Electron Microscopy (SEM) and SEM-Energy Dispersive X-ray Spectroscopy (SEM-EDS)

The SEM images and SEM-EDS are obtained using a LEO 1560 SEM equipped with spatially resolved energy dispersive X-ray spectroscopy. Samples were prepared by depositing several drops of NPs dispersion in hexane on a silicon wafer attached to the SEM sample holder by conductive carbon tape.

2.3.5 X-ray Powder Diffraction (XRD)

XRD characterizations can provide the collective phase information of the NPs. They are carried out on a Bruker AXS D8-Advanced diffractometer with Cu Kα radiation ($\lambda = 1.5418$ Å). Drops of the NP hexane dispersion are dried on a glass slide or silicon wafer to form a non-transparent film of NPs on the substrate for analysis.

2.3.6 Electrochemical Measurements

The electrochemical measurements are performed on a Pine Electrochemical AFCBP1 Potentiostat or Autolab 302 Potentiostat, with a three-electrode system consisting of a glassy carbon (GC) working electrode (5 mm in diameter), an Ag/AgCl reference electrode (10% KNO_3), and a platinum wire counter electrode.

2.3.7 Magnetic Measurements

The magnetic hysteresis loops are collected on a Vibrating Sample Magnetometer (VSM) (LakeShore, 7404) with a field up to 1.5 kOe. The NPs are washed with hexane and ethanol combination and then dried at room temperature to obtain a non-sticky powder. Several mg of the powder is transferred to a gelatin capsule (0.3 ml, Electron Microscopy Science). A cotton ball is then pressed the powder firmly in the capsule for highly-sensitive measurement.

2.3.8 UV-Vis Measurements

UV-Vis spectra is used to analyze the surface plasma resonance (SPR) properties

of noble metal (Au, and Ag) NPs. They are collected on a PerkinElmer Lambda 35 UV/Vis spectrometer. The NPs dispersed in hexane solution (diluted, ~0.1 mg/ml) can be used to collect UV-Vis spectra.

Reference

1. S. Guo, S. Zhang, S. Sun, *Angew. Chem. Int. Ed.* **2013**, DOI: anie.201207186.

2. C. B. Murray, C. R. Kagan, M. G. Bawendi, *Annu. Rev. Mater. Sci.* **2000**, *30*, 545-610.

3. J. Park, J. Joo, S. G. Kwon, Y. Jang, T. Hyeon, *Angew. Chem. Int. Ed.* **2007**, *46*, 4630-4660.

4. S. Zhang, J. Lee, S. Sun, *The Open Sur. Sci. J.***2012**, *4*, 26-34.

5. J. Lee, S. Zhang, S. Sun, *Chem. Mater* **2013**, *25*, 1293-1304.

6. V. K. LaMer, R. H. Dinegar, *J. Am. Chem. Soc.***1950**, *72*, 4847-4854.

7. L. Ratke, P. W. Voorhees, *Growth and coarsening: Ostwald ripening in material processing*, Springer, **2002**.

8. Y. Xia, Y. Xiong, B. Lim, S. E. Skrabalak, *Angew. Chem. Int. Ed.* **2009**, *48*, 60-103.

9. Y. W. Jun, J. S. Choi, J. Cheon, *Angew. Chem. Int. Ed.* **2006**, *45*, 3414-3439.

10. Stamenkovic, V. R., Mun. B. S., Arenz. M., Mayrhofer. K. J. J., Lucas. C. a, Wang. G., Ross. P. N., Markovic, N. M. *Nature Mater.* **2007**, *6*, 241-247.

11. Stamenkovic,V. R.; Fowler, B; Mun, B. S; Wang, G; Ross, P. N; Lucas, C. A; Markovic, N. M. *Science* **2007**, *315*, 493-497.

Chapter 3

Structure-Induced Stain Control of Monodisperse Intermetallic FePt Nanoparticles for Oxygen Reduction Reaction Catalysis

Controlling crystal structure of multimetallic alloy nanoparticles (NPs) can provide a great opportunity to tune and optimize NPs catalysis, but still lack of systematically study in both synthesis and mechanism. Starting with monodisperse bimetallic FePt NPs that are made in non-aqueous solution synthesis, here we demonstrate the intermetallic ordering in face centered tetragonal (*fct*) FePt NPs leads to drastic enhancement in ORR catalysis comparing to traditional disordered face centered cubic (*fcc*) FePt NPs. The atomic-scale structural analysis and quantum mechanics-molecular mechanics (QM-MM) simulation reveal this structure-induced enhancement is contributed to the surface strain optimization in FePt/Pt core/shell NPs formed by electrochemical dealloying, in which the *fct*-FePt core can reduce the over-compression in fcc-FePt/Pt core/shell NPs and therefore optimize the oxygen adsorption energy (E_o) for ORR. This structure-control principle presents a new model to advanced NP catalysts with simultaneous enhancement in both activity and durability for practical applications.

3.1 Background and Motivation

In searching for highly efficient nanoparticle (NP) catalysts for chemical conversions and for renewable energy applications, one often explores NP size, shape and composition as important parameters to tune catalytic properties. [1, 2] Recent advance in monodisperse NP synthesis with these controlled parameters has led to ever increased catalytic performance in oxygen reduction reaction (ORR), a key step to low-temperature polymer electrolyte membrane fuel cells; and more importantly, is highly efficient to elucidate the correlation of NP parameter-catalysis in order to provide the predictable models for catalyst design and optimization. [2] In this regard, Pt-based NPs have constantly been the target subject due to their relatively high activity and stability for ORR in acidic conditions. [2] For example, monodisperse Pt binary and ternary alloy NPs with controlled size, shape, compositions and core/shell type NPs with a thin Pt-coating are prepared as robust ORR catalysts and are detailed investigated the electronic and geometric effect of each parameter in the catalysis. [3-14] However, these well-established Pt-based systems were mainly centered on structurally disordered NPs with limited report on ordered intermetallic NPs for ORR catalysis. This is mainly because intermetallic Pt-alloy NPs can only be obtained via high-temperature annealing during which NPs are strongly subjective to aggregation. [15] Without precise control of the uniform size/shape/composition of intermetallic NPs, previous Co-Pt intermetallic systems show very contradictory phenomena in ORR activity and durability. [16-18] Coated with MgO etc. protective shell, partially ordered

FePt NPs can be produced and exhibit increased ORR activity and durability. [19] But the multi-step MgO-coating and MgO-removal processes make the preparation too complicated to achieve uniform NPs-C electrochemical composites. Furthermore, it is highly desirable, but has not been achieved yet, to explore the mechanism manipulating this intermetallic-governed ORR catalysis.

Here we introduce a facile approach to monodisperse binary FePt NPs, which can be produced with the face-centered cubic (*fcc*) disordered structure *via* the organic solution chemistry [20] and can be transformed into face-centered tetragonal (*fct*) structured intermetallic NPs *via* protective annealing (**Figure 3.1**). The *fct*-FePt NPs can be converted to *fct*-FePt/Pt core/shell NPs with around 3 atomic layers of Pt shell after electrochemical dealloying, and then show around 200% enhancement in ORR activity and much increased durability comparing to *fcc*-FePt NPs counterpart. The atomic-scale structural analysis is conducted to monitor NPs' structural evolutions (intermetallic and core-shell), while the quantum mechanics-molecular mechanics (QM-MM) simulation is applied to reveal the mechanism of structure-induced enhancement. It is contributed to the surface strain optimization of FePt/Pt core/shell NPs in which the *fct* phase transformation in the core can reduce the over-compression in fcc-FePt/Pt NPs and therefore optimize the surface oxygen adsorption energy (E_o) for ORR. The E_o of *fct*-FePt/Pt core/shell NPs is calculated to be -0.97 eV, closer to the ideal E_o value of -1.0 eV than *fct*-FePt/Pt core/shell NPs (-0.94 eV).
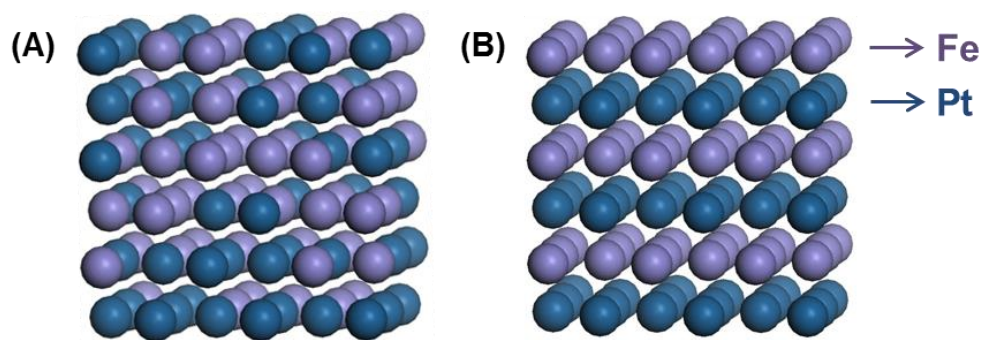
Figure 3-1. Schematic illustration of crystalline structure of *fcc*-FePt (**A**) and *fct*-FePt (**B**).

3.2 Results and Discussion

3.2.1 Synthesis and Structural Control of FePt NPs

FePt NPs were synthesized by co-reduction of platinum acetylacetonate, $Pt(acac)_2$, and thermal decomposition of iron pentacarbonyl, $Fe(CO)_5$ according to modified previous method (see **Experimental**). [21] In the synthesis, oleylamine and oleic acid were used to stabilize the NPs. Fe/Pt composition was controlled by varying the molar ratio of $Fe(CO)_5/Pt(acac)_2$ and reaction temperature. Increasing the reaction temperature or adding more $Fe(CO)_5$ tend to integrate more Fe in as-synthesized NPs, generating $Fe_{51}Pt_{49}$, $Fe_{42}Pt_{58}$, $Fe_{33}Pt_{67}$ and $Fe_{27}Pt_{73}$ NPs as indicated by coupled plasma-atomic emission spectroscopy (ICP-AES) and summarized in **Table 3-1**. Transmission electron microscopy (TEM) images show that these as-synthesized FePt with different compositions have constantly been the nanocubes of 8.5 nm ± 0.5 nm (**Figure 3-2**). In consistency with previous report, the as-synthesized FePt NPs

have typical *fcc* structure as indicated in their X-ray diffraction (XRD) patterns

(**Figure 3-3A**).[21]

Sample	Pt(acac)$_2$, mol	Fe(CO)$_5$, ml	Temperature, °C	As-synthesized NPs
A	0.5	0.16	220	Fe$_{51}$Pt$_{49}$
B	0.5	0.14	220	Fe$_{42}$Pt$_{58}$
C	0.5	0.14	200	Fe$_{33}$Pt$_{67}$
D	0.5	0.14	180	Fe$_{27}$Pt$_{73}$

Table 3-1. The composition control of as-synthesized FePt NPs by varying the precursor ratio of Fe(CO)$_5$/Pt(acac)$_2$ and reaction temperature.
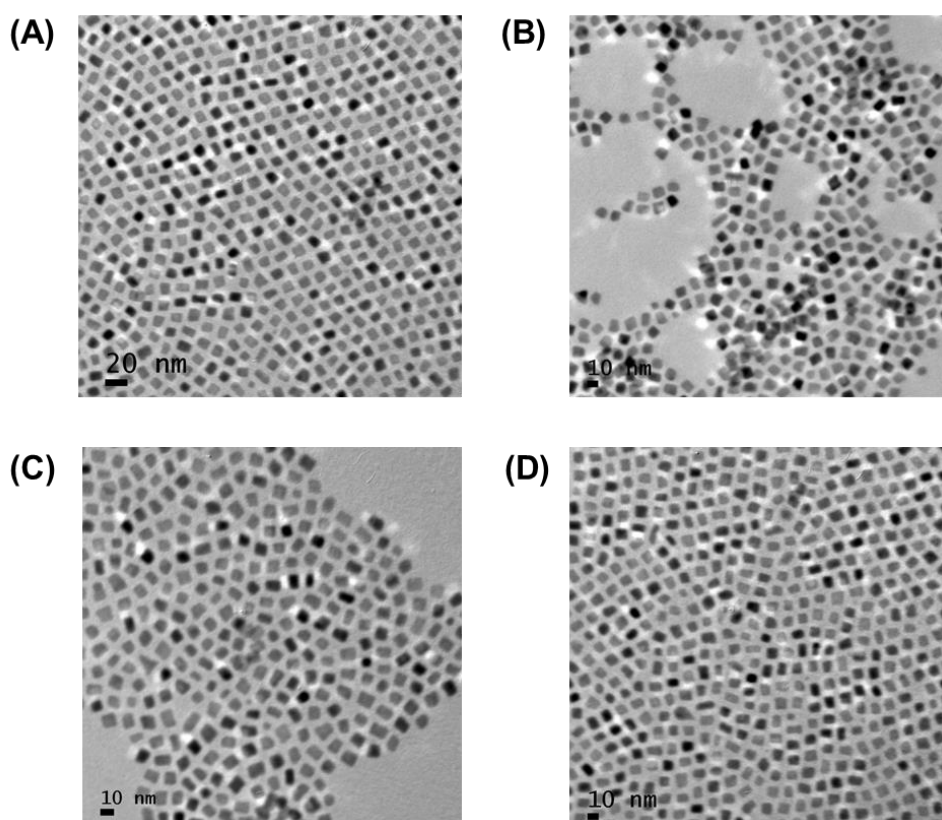
Figure 3-2. TEM images of the as-synthesized Fe$_{51}$Pt$_{49}$ (**A**), Fe$_{42}$Pt$_{58}$ (**B**), Fe$_{33}$Pt$_{67}$ (**C**) and Fe$_{27}$Pt$_{73}$ (**D**) NPs.
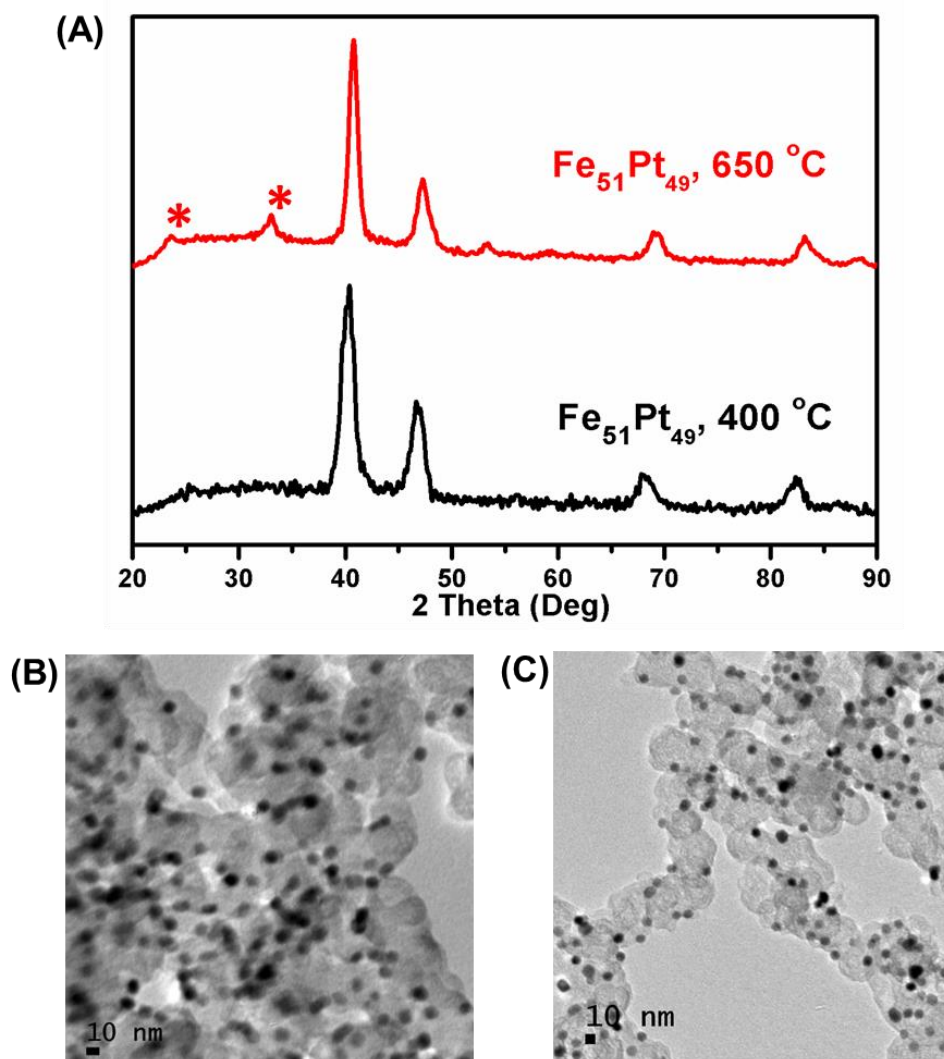
Figure 3-3. (**A**) XRD patterns of the $Fe_{51}Pt_{49}$ NPs annealed at 400 ℃, 650 ℃ (stars denote the *fct*-FePt peaks). (**B, C**) TEM images of the $Fe_{51}Pt_{49}$ NPs annealed at 400 ℃, 650 ℃. The NPs were deposited on the Ketjen carbon support and annealed under 95% Ar + 5% H_2 for 1 h.

High temperature annealing was used to initiate the phase transformation from the *fcc*-FePt to *fct*-FePt as well as to remove the organic surfactant for electrochemical purpose. [22] Given this annealing always caused NPs aggregation, we uniformly

loaded the as-synthesized NPs on Ketjen carbon (C) before the annealing (see **Experimental**). The NPs loading was finished in only hexane solution where the NPs were well dispersed and then physically absorbed onto the C support, which was different to previous process in hexane + acetone tended to agglomerate NPs. **Figure 3-3B&C** show the typical TEM images of the $Fe_{51}Pt_{49}$ under 95% Ar + 5% H_2 at 400 °C & 650 °C for 1 h. The high temperature treated NPs well preserved their monodisperse morphology due to the protection of C support, but were converted to thermodynamically stable spherical (polyhedron) NPs from cubes after the drastic surface atomic rearrangement at high temperature. The XRD was applied to monitor the *fcc-fct* structural transition (**Figure 3-3A**). For example, $Fe_{51}Pt_{49}$ remained to be *fcc* NPs after annealed at 400 °C. Highly ordered *fct*-$Fe_{51}Pt_{49}$ NPs were formed at 650 °C with two super-lattice peaks with 2 theta degree at 24, 33 °.

3.2.2 Electrochemical Dealloying of *fct*- and *fcc*-FePt NPs

The monodisperse *fcc*- and *fct*-$Fe_{51}Pt_{49}$ NPs supported on C (C-NPs) were ideal for systematic study of structure-governed catalysis in ORR. The electrochemical ink was made by dispersing C-NPs in deionized water + isopropanol + 5% Nafion (v/v/v = 4/1/0.05) to form a suspension of 0.5 mg catalyst/mL. 25 μL of the ink was deposited on the glassy carbon (GC) surface of a rotating disk electrode (RDE) and dried at ambient environment. The C-NPs were further electrochemically sweeped from 0.05 V to 1.02 V (vs. RHE) in the N_2-saturated 0.1 M $HClO_4$ solution to obtain

the stable cyclic voltammograms (CVs) for the calculation of electrochemically active surface area (ECASA) of the catalyst. [8, 23] It was noteworthy to mention that the surface Fe atoms were subject to be dealloyed during this process, generating the FePt/Pt core/shell NPs. [8] This electrochemical Fe dealloying in acidic solution was similar to previous report on CuPt, CoCuPt NPs and FePtCu nanorods (NRs). [9, 14, 24] The FePt/Pt core/shell NPs were characterized by atomically resolved aberration-corrected scanning transmission electron microscopy (STEM) and STEM-electron energy loss spectroscopy (STEM-EELS) elemental mapping. **Figure 3-4** show the high-angle annular dark field (HAADF)-STEM images and the related STEM-EELS line scan on dealloyed *fcc-* and *fct*-FePt NPs, confirming the formation of the Pt-shell with a thickness of 0.6 nm (around 3 atomic layers) on both NPs. But the unique part of *fct*-FePt NPs is the FePt core well retains the intermetallic ordering after the formation of a compact *fcc*-Pt shell, as demonstrated in **Figure 3-4A**. Considering HAADF-STEM image reflects the Z-contrast of metal, Pt tends to have a higher intensity (brighter image) than that of Fe. It is clearly seen that Pt atomic layers and Fe atomic layers alternate along one direction in the core region while a three-atomic-layer of Pt sit in the shell of NPs.
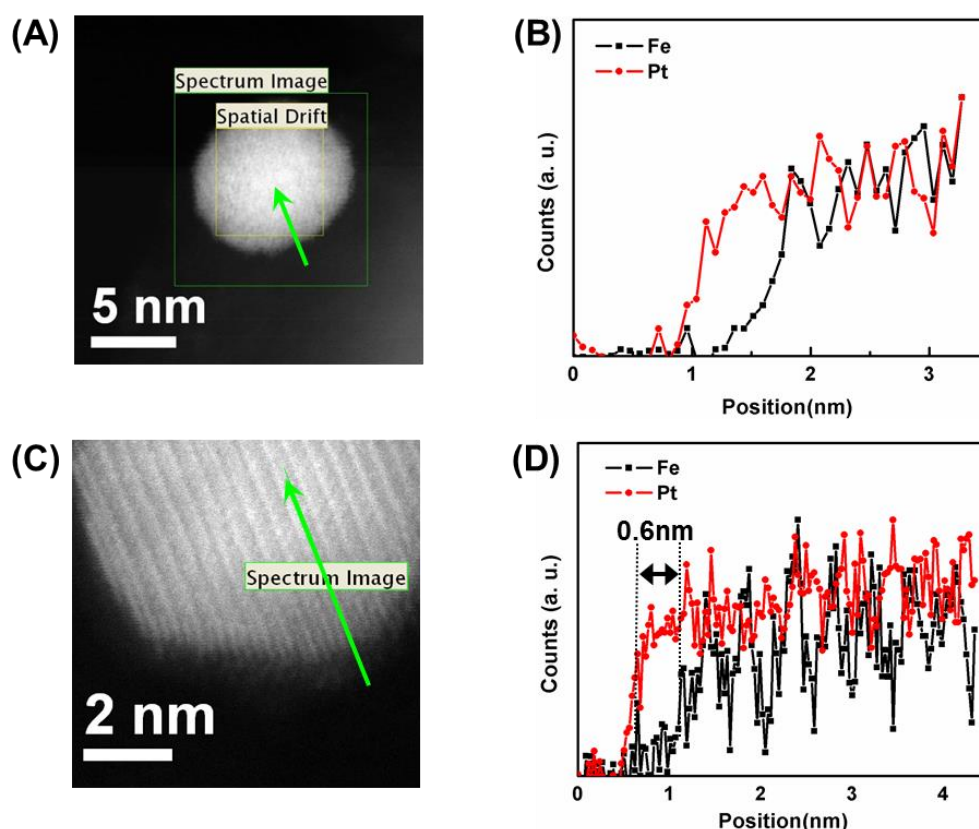
Figure 3-4. (**A, C**) HAADF-STEM images of the $Fe_{51}Pt_{49}$ NPs annealed at 400 ℃ (**A**), 650 ℃ (**C**) after CVs dealloying. (**B, D**) STEM-EELS line scans crossing the $Fe_{51}Pt_{49}$ NPs annealed at 400 ℃ (**B**), 650 ℃ (**D**) after CVs dealloying.

Also along with the Fe dealloying, the NPs composition was changed to $Fe_{25}Pt_{75}$ for *fcc*-$Fe_{51}Pt_{49}$ and $Fe_{26}Pt_{74}$ for *fct*-$Fe_{51}Pt_{49}$. This is different to previous observation of enhanced chemical stability and negligible Fe loss of *fct*-FePt when immersed in acidic solution. [19] Clearly, in electrochemical condition, the surface Fe is still vulnerable even though in the *fct*-FePt NPs.

3.2.3 Electrocatalysis of *fct*- and *fcc*-FePt NPs

43

Figure 3-5A, 3-6A & 3-7A shows the CVs of FePt/Pt core/shell NPs and commercial C-Pt (Pt NPs with a size of 2.5-3.5 nm) in the N_2-saturated 0.1 M $HClO_4$ solution with a sweep rate of 50 mV/s. The CV curves display strong peaks related to hydrogen underpotential adsorption/desorption below 0.4 V and Pt oxidization/reduction above 0.6 V. Among them, the hydrogen underpotential desorption (H_{upd}) peaks are used to estimate ECASA of the catalyst. [8, 23] **Figure 3-5B** shows a typical ORR polarization curve of the *fct*-$Fe_{51}Pt_{49}$ obtained at room temperature in O_2-saturated 0.1 M $HClO_4$ with a sweep rate of 20 mV/s and a rotation speed of 1600 rpm. The *fcc*-$Fe_{51}Pt_{49}$ and commercial Pt are also studied in the same condition (**Figure 3-6B & 3-7B**). The electrochemical reduction reaches the diffusion-limit below 0.8 V and a mixed kinetic-diffusion control region can be find between 0.8 and 1.0 V. The kinetic current related to the ORR can be evaluated from the polarization curve by using mass-transport correction and normalized to electrochemically active surface area (ECASA) and Pt amount. **Figure 3-5C** summarizes the specific activity comparison of *fcc*-$Fe_{51}Pt_{49}$, *fct*-$Fe_{51}Pt_{49}$ and commercial Pt. The *fct*-$Fe_{51}Pt_{49}$ exhibit a specific activity of 3.8 mA/cm^2 at 0.9 V (0.60 mA/cm^2 at 0.95 V), with an enhancement factor of over 2 comparing to *fct*-$Fe_{51}Pt_{49}$ (1.60 mA/cm^2 at 0.9 V and 0.26 mA/cm^2 at 0.95 V) and over 10 comparing to benchmark commercial Pt catalyst (0.32 mA/cm^2 at 0.9 V and 0.081 mA/cm^2 at 0.95 V), respectively.
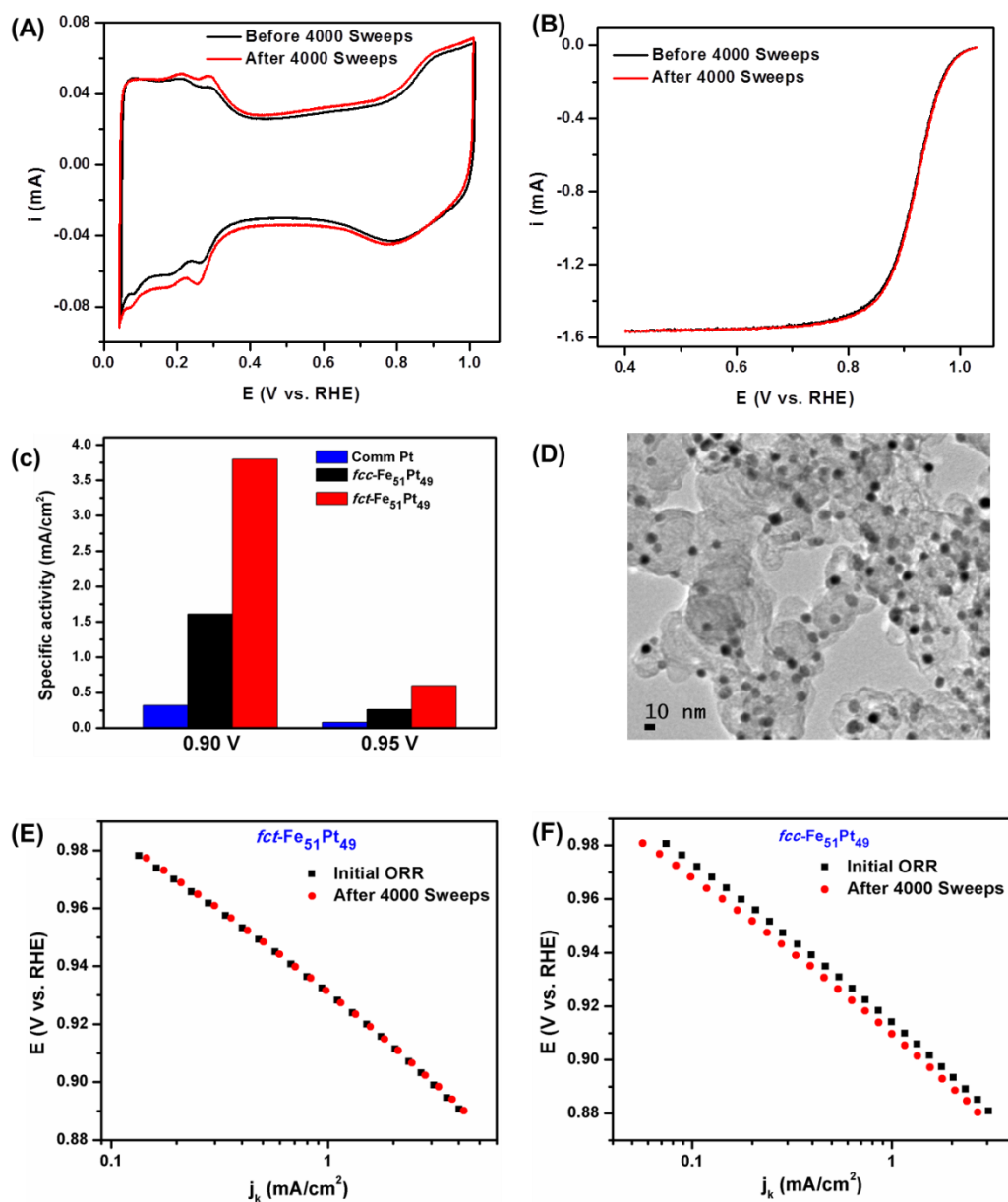
Figure 3-5. (**A**) CVs and (**B**) ORR polarization curves of the *fct*-Fe$_{51}$Pt$_{49}$ NPs before and after 4000 potential sweep between 0.6-1.0 V vs. RHE. (**C**) Specific ORR activities of *fcc*-Fe$_{51}$Pt$_{49}$, *fct*-Fe$_{51}$Pt$_{49}$ and commercial C-Pt with the RDE rotation rate at 1600 rpm. (**D**) TEM image of the *fct*-Fe$_{51}$Pt$_{49}$ NPs after 4000 potential sweep between 0.6-1.0 V vs. RHE. (**E, F**) Tafel plots of *fcc*-Fe$_{51}$Pt$_{49}$ (**F**), *fct*-Fe$_{51}$Pt$_{49}$ (**E**) NPs before and after 4000 potential sweep between 0.6-1.0 V vs. RHE.
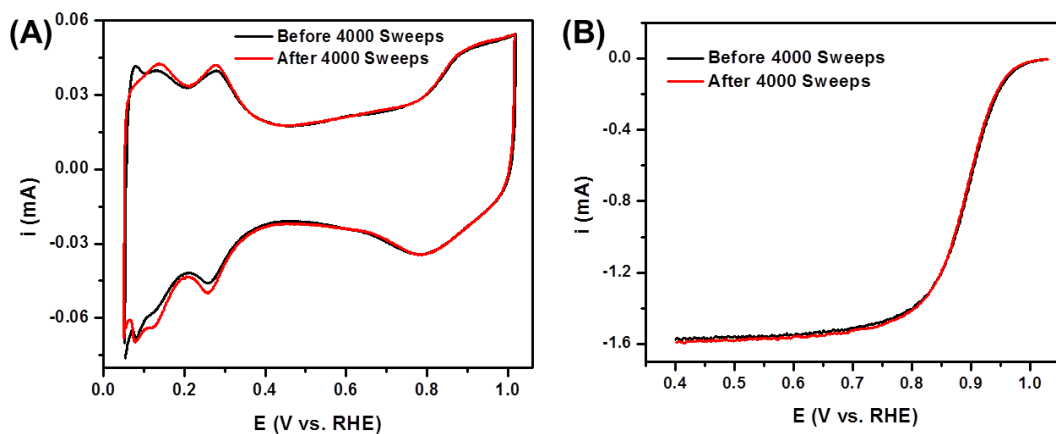
Figure 3-6. (**A**) CVs and (**B**) ORR polarization curves of the *fct*-Fe$_{51}$Pt$_{49}$ NPs before and after 4000 potential sweep between 0.6-1.0 V vs. RHE.
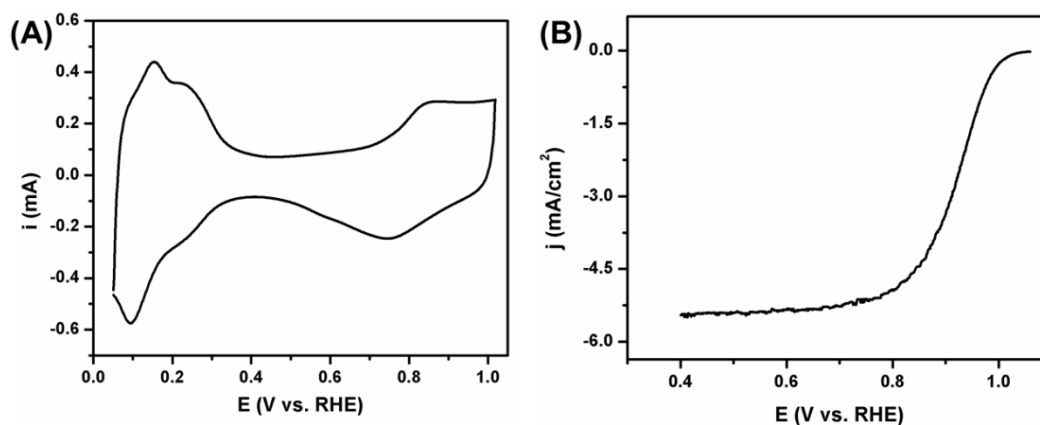
Figure 3-7. (**A**) CVs and (**B**) ORR polarization curves of the commercial C-Pt catalyst.

We further studied the stability of catalysts by sweeping the NPs between 0.6 and 1.1 V (vs. RHE) in the O$_2$-saturated 0.1 M HClO$_4$ with a scan rate of 50 mV/s. **Figure 3-5D** show the TEM image of *fct*-Fe$_{51}$Pt$_{49}$ after 4000 sweeps. We can see there is no visible morphology change during the stability test. We also studied the CVs and ORR polarization curves of the NPs after 4000 sweeps, and provided the Tafel plots of *fcc*-Fe$_{51}$Pt$_{49}$ and *fct*-Fe$_{51}$Pt$_{49}$ (**Figure 3-5E & F**, which describe the

specific activities (j_k, kinetic current density) as a function of electrode potential)
before and after stability test. The *fct*-Fe$_{51}$Pt$_{49}$ NPs catalysts show the overlaped Tafel
plot suggesting the high ORR catalytic stability of *fct*-Fe$_{51}$Pt$_{49}$, while *fcc*-Fe$_{51}$Pt$_{49}$ NPs
have an obvious activity drop after stability test. The mass activity of our FePt NPs is
limited by their big size. But the *fct*-Fe$_{51}$Pt$_{49}$ NPs still exhibited the mass activity of
400 mA/mg $_{Pt}$ at 0.9 V (vs. RHE) after 4000 sweeps, almost 3 times higher than
fcc-Fe$_{51}$Pt$_{49}$ NPs (135 mA/mg $_{Pt}$, also after 4000 sweeps) and commercial Pt (143
mA/mg $_{Pt}$, before stability test) which has much smaller size.

3.2.4 Theoretical Calculation for Enhancement Mechanism

The intermetallic structure-induced ORR enhancement was studied by the
computational simulation (see **Experimental**). We developed an 8 nm core-shell
cuboctahedrons (thermodynamically stable polyhedron shape) NPs model consisted
by the Fe$_{50}$Pt$_{50}$ alloy core (*fcc*-FePt or *fct*-FePt) and the shell of *fcc*-Pt (3 atomic
layers) (**Figure 3-8**). The core-shell FePt/Pt NPs have a theoretical composition of
around Fe$_{25}$Pt$_{75}$, very consistent with those of our NPs after Fe dealloying. Based on
the core/shell NP model, oxygen adsorption energy (E_o) on *fcc*-FePt/Pt or *fct*-FePt/Pt
are calculated to be -0.94 eV and -0.97 eV by using quantum mechanics-molecular
mechanics (QM-MM) calculations, respectively. It is well known that -1.0 eV is the
ideal E_o for ORR (**Table 3-2**). [26, 27] As a result of closer surface E_o to this best

theoretical value, *fct*-FePt/Pt show much enhanced ORR activity comparing to

fcc-FePt/Pt. This trend was indeed confirmed in our study.
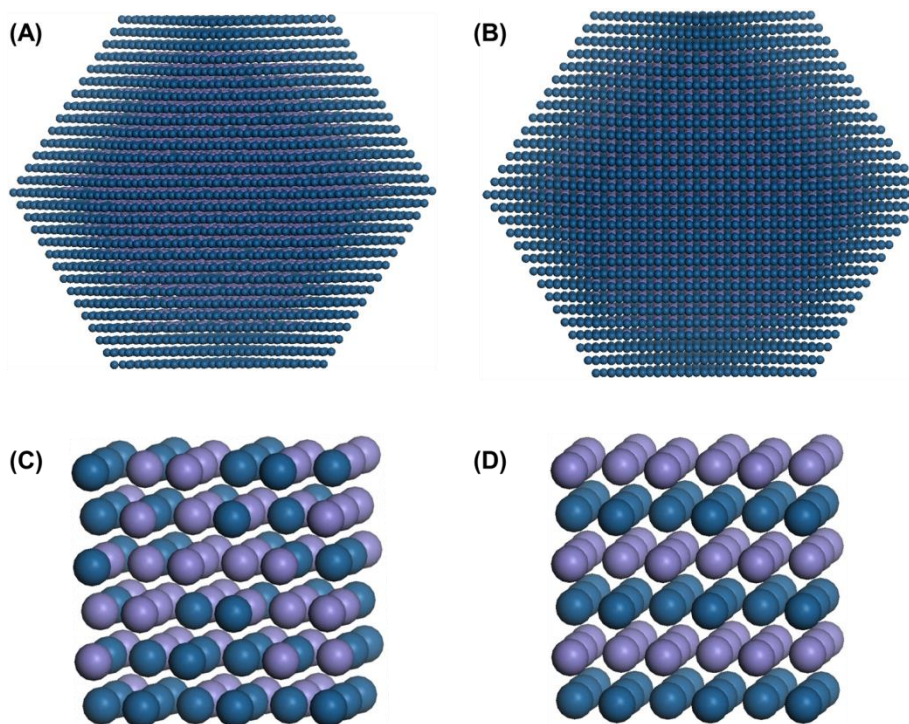
Figure 3-8. (**A**, **B**) 8 nm cuboctahedral FePt/Pt core/shell NPs models constructed for QM-MM calculations. (**A**) model of *fcc*-FePt/Pt core/shell NPs with 7667 Pt atoms and 2512 Fe atoms. (**B**) model of *fct*-FePt/Pt core/shell NPs with 7704 Pt atoms and 2405 Fe atoms. Two models have a core composition of $Fe_{50}Pt_{50}$ and a three-atomic-layer shell of Pt. (**C**, **D**) Periodic supercells consisting of 108 atoms used to simulate atomic structure of *fcc*-FePt (**C**) and *fct*-FePt (**D**). The blue ball stands for Pt atom and purple ball stands for Fe atom.

NPs	E_o (eV)
fcc-FePt/Pt	-0.94
fct-FePt/Pt	-0.97
Ideal value	-1.0
Pt	-1.2

Table 3-2. The calculated E_o of *fcc*-FePt/Pt, *fct*-FePt/Pt, Pt. The ideal value is based on reference [26, 27]

core	$a_{[100]}/a_{Pt}$	$a_{[010]}/a_{Pt}$	$a_{[001]}/a_{Pt}$
fcc-FePt	0.961	0.964	0.965
fct-FePt	0.971	0.971	0.945

Table 3-3. The lattice constant comparison of FePt and Pt. a_{Pt} is the lattice constant of *fcc*-Pt. $a_{[100]}$, $a_{[010]}$, $a_{[001]}$ are the calculated interplanar distances along [100], [010] and [001] directions.

In core/shell NPs, strain effect is one of the paramount impacts on the surface energetics. [14] The mismatch of crystalline lattice constant between core and shell can produce the stretch/compression on surface Pt and therefore change the E_o. Pure Pt has an E_o of -1.2 eV, suggesting that the oxygenate species are too strongly bonded and desorption of catalytic mediate is unfavorable. [26] Previous report on dealloyed CuPt systems described the compression on Pt tended to decrease this E_o. In *fcc*-FePt/Pt NPs, *fcc*-FePt core can compress *fcc*-Pt shell due to smaller lattice parameters (**Table 3-3**). But this Pt shell is so over-compressed (E_o at -0.94 eV) and become resistant to adsorption of oxygenate species. We find the phase

transformation to *fct*-FePt can relieve this over-compression. During the phase transformation, crystalline interplanar distance of FePt is expanded in two directions ([100] and [010]) and shrunk in another direction ([001]). As an overall consequence, the strain of *fct*-FePt/Pt NPs is optimized and E_o is driven to -0.97 eV which supports a better balance in the ORR catalytic adsorption and desorption on the surface of *fct*-FePt/Pt NPs.

3.3 Summary

In summary, we have developed a facile process to synthesize monodisperse FePt NPs loaded on C support with controlled crystalline structures (*fcc* and *fct*). These FePt NPs can be converted into core/shell structured FePt/Pt NPs with a structure-controlled FePt core, and are used as a robust kind of NP catalysts for ORR. With an intermetallic ordered FePt core, *fct*-FePt/Pt NPs exhibit over 200 % specific activity, almost 300% mass activity and much enhanced stability comparing to *fcc*-FePt/Pt NPs. This structure-induced enhancement is simulated by QM-MM calculation and is contributed to the surface strain optimization in FePt/Pt core/shell NPs controlled by FePt intermetallic structure. Correspondingly, *fct*-FePt/Pt NPs have an E_o at -0.97 eV, closer to ideal value of -1.0 eV than *fcc*-FePt/Pt NPs (-0.94 eV). This structure-control strategy provides a new model to optimize NPs catalytic activity and durability for practical ORR and other catalytic applications.

3.4 Experimental

Chemicals and Materials. Oleylamine (OAm, >70%), oleic acid (OA), 1-octadecene (ODE), Pt(acac)$_2$ (acac = aceylacetonate), iron pentacarbonyl (Fe(CO)$_5$), hexane, isopropanol, ethanol, and Nafion (5%) were all purchased from Sigma Aldrich and used without further purification. C-Pt (20% mass loading with a diameter of 2.5-3.5 nm) catalyst was obtained from Fuel Cell Store.

Characterization. XRD characterizations were carried out on a Bruker AXS D8-Advanced diffractometer with Cu Kα radiation (λ =1.5418 Å). TEM images were obtained from a Philips CM 20 operating at 200 kV. STEM analyses were carried out using a Hitachi HD2700C (200kV) with a probe aberration-corrector, in the Center for Functional Nanomaterials at Brookhaven National Lab. The EELS line-scan was obtained by a high resolution Gatan-Enfina ER with a probe size of 1.3Å. A power law function was used for EELS background subtraction. TEM and HRTEM samples were prepared by depositing a single drop of diluted NPs dispersion on amorphous carbon coated copper grids. The inductively coupled plasma-atomic emission spectroscopy (ICP-AES) measurements were carried on a JY2000 Ultrace ICP Atomic Emission Spectrometer equipped with a JY AS 421 autosampler and 2400g/mm holographic grating. Electrochemical measurements were performed on a Autolab 302 potentiostat (6 mm GC). Reversible hydrogen (or Ag/AgCl) was used as a reference electrode and platinum wire as a counter electrode.

Synthesis of FePt Nanoparticles (NPs). Under a gentle flow of N_2, ODE (10 mL), oleic acid (1.28 ml, 2 mmol), oleylamine (1.36 ml, 2 mmol) and $Pt(acac)_2$ (0.2 g, 0.5 mmol) were mixed in a four-necked flask. The mixture was magnetically stirred and heated to 120 °C to generate a light yellow transparent solution. Under a N_2 blanket, 0.16 mL of $Fe(CO)_5$ was added into the solution. The solution was heated to 220 °C at a rate of about 3 °C /min and kept at this temperature for 1 hour before it was cooled to room temperature. The NPs were separated by adding isopropanol (50 mL), followed by centrifugation (8500 rpm, 8 min). The NPs were further purified by dispersing into hexane (20 mL) and centrifugation (5000 rpm, 8 min) to remove any un-dispersed precipitates. The product was precipitated out by adding ethanol (50 mL) and centrifugation (8500 rpm, 8 min) and re-dispersed in hexane. The synthesis yielded $Fe_{51}Pt_{49}$ NPs. Different composition was obtained by varying the amount of $Fe(CO)_5$ and reaction temperature, as summerized in **Table 3-1**.

Catalyst Preparation. The as-synthesized NPs and Ketjen-300 J carbon at the weight ratio of 1:2 were mixed in 20 mL mixture of hexane and sonicated for 1 h to deposit NPs on carbon. The product was separated by centrifugation (8500 rpm, 3 min). The NPs-C were dried under ambient conditions and annealed at different temperatures for 1 h in a gas flow of Ar + 5% H_2. The product was then redispersed in a mixture of deionized water, isopropanol and Nafion (V/V/V = 4/1/0.05). 25 μL catalyst ink (0.5 mg/mL) was deposited on the working electrode (glassy carbon

rotating disk electrode, GC-RDE) that was polished prior to catalyst deposition by 0.1 μm and 0.05 μm alumina powder and rinsed by sonication in ethanol and in deionized water. The catalyst was dried at ambient condition.

Electrochemical Measurements. Cyclic voltammograms (CVs) were obtained by scaning between 0.05 V-1.02 V *vs* RHE at a scan rate of 50 mV/s in N_2-saturated 0.1M $HClO_4$. ORR polarization curves were obtained by scaning the potentials from 1.0 to 0.4 V *vs* RHE at a scan rate of 20 mV/s in O_2-saturated 0.1 M $HClO_4$ with the GC-RDE rotating at 1600 rpm.

Theoretical Calculation.

I. E_O for Core/Shell Nanoparticles (NPs)
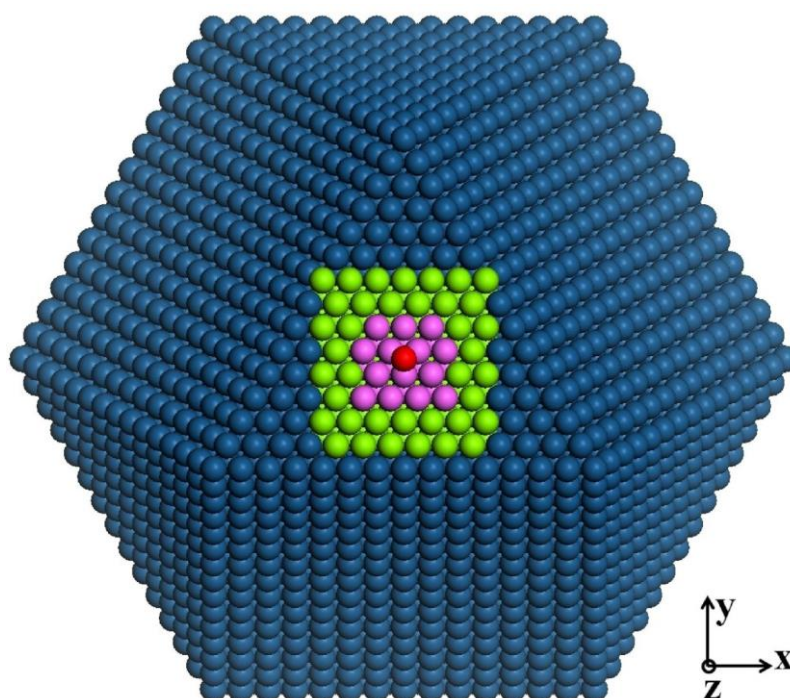
Figure 3-9. Atomic configuration of the cuboctahedron NPs, shown as views perpendicular to the (111) facet. The entire system is partitioned into interior QM region (red and pink spheres), boundary QM region (green spheres) and MM region (blue spheres). The red sphere represent the adsorbed O atom.

Core/shell NPs are modeled by cuboctahedrons with eight (111) facets and six (100) facets as shown in **Figure 3-9**. The core/shell structure consists of pure Pt shell and FePt alloy core. The size of NPs is 8 nm corresponding to 10179 atoms in total. E_O is determined by placing an O atom at the *fcc*-hollow site on the (111) facet, which is calculated by

$$E_O = E_{QM/MM}[NP+O] - E_{QM/MM}[NP] - \frac{1}{2}E_{QM}[O_2] \qquad (1)$$

where $E_{QM/MM}[NP+O]$ and $E_{QM/MM}[NP]$ are total energies of NPs with and without O adsorbate, respectively obtained from quantum mechanics-molecular mechanics (QM-MM) calculations. $E_{QM}[O_2]$ is the total energy of an O_2 molecule calculated by the stand-alone density functional theory (DFT).

In QM/MM calculations, as shown in **Figure 3-9**, the entire modeled system is partitioned into two spatial domains: a QM region treated by constrained DFT and a MM region by empirical atomistic simulations. The QM region is further divided into an interior QM region and a boundary QM region. The former involves bond breaking, chemical reaction and charge transfer, etc. where topological changes of charge density take place. The latter serves as a buffer region where no such topological change to the charge density occurs. The technical details and validations of the QM/MM method can be found elsewhere. [28] The QM region measures

17Å×17Å×8Å in x, y, and z directions, respectively with 195 atoms, where the innermost 8.4Å×7.3Å×4Å is the interior QM region containing the *fcc*-hollow site for oxygen adsorption. The MM region consists of the rest of the system where the strain effect due to the lattice mismatch between core and shell is captured. The DFT calculations are performed using the VASP package [29, 30] with the projector augmented wave pseudopotentials [31] and Perdew-Burke-Ernzerhof generalized gradient approximation (PBE-GGA) [32]. The calculations are performed at Γ point with 400 eV energy cutoff. The embedded atom method (EAM) potentials [33] are used in the MM simulations, which have been rescaled to yield the same lattice constant and bulk modulus as those of DFT. The atomic relaxation is carried out with the conjugate-gradient algorithm and the force convergence criterion is 0.03 eV/Å.

II. Lattice Constant of Two Core Structures

A periodic supercell consisting of 108 atoms is used to simulate atomic structure of FePt core materials. All atoms are fully relaxed under the constant (zero) pressure by using stand-alone DFT calculations with an energy cutoff of 280 eV and a 3×3×3 *k*-point mesh. (i) For *fcc*-FePt, 50% atoms are randomly selected to be Pt atoms and the remaining atoms are Fe atoms. In the model shown in Figure **3-1A**, there are 53 Pt atoms and 55 Fe atoms. (ii) For *fct*-FePt, Pt and Fe atoms are distributed layer by layer as depicted in **Figure 3-1B**.

Reference

1. H. Yang, *Angew. Chem. Int. Ed.* **2011**, *50*, 2674-2676.

2. S. Guo, S. Zhang, S. Sun, *Angew. Chem. Int. Ed.* **2013**, DOI: anie.201207186.

3. C. Wang, H. Daimon, T. Onodera, T. Koda, S. Sun, *Angew. Chem. Int. Ed.* **2008**, *47*, 3588-3591.

4. C. Wang, D. van der Vliet, K.-C. Chang, H. You, D. Strmcnik, J. A. Schlueter, N. M. Markovic, V. R. Stamenkovic, *J. Phys. Chem. C* **2009**, *113*, 19365-19368.

5. C. Wang, M. Chi, D. Li, D. van der Vliet, G. Wang, Q. Lin, J. F. Mitchell, Karren L. More, N. M. Markovic, V. R. Stamenkovic, *ACS Catal.* **2011**, *1*, 1355-1359.

6. J. Zhang, H. Yang, J. Fang, S. Zou, *Nano Lett.* **2010**, *10*, 638-644.

7. J. Wu, L. Qi, H. You, A. Gross, J. Li, H. Yang, *J. Am. Chem. Soc.* **2012**, *134*, 11880-11883.

8. S. Guo, D. Li, H. Zhu, S. Zhang, N. M. Markovic, V. R. Stamenkovic, *Angew. Chem. Int. Ed.* **2013**, *52*, 3465-3468.

9. H. Zhu, S. Zhang, S. Guo, D. Su, S. Sun, *J. Am. Chem. Soc.* **2013**, *135*, 7130-7133.

10. S. Zhang, M. Onder, D. Su, S. Sun, *Angew. Chem. Int. Ed.* **2013**, *52*, 3681-3684.

11. K. Sasaki, H. Naohara, Y. Cai, Y. M. Choi, P. Liu, M. B. Vukmirovic, J. X. Wang, R. R. Adzic, *Angew. Chem. Int. Ed.*, **2010**, *49*, 8602-8607.

12. C. Wang, D. van der Vliet, K. L. More, N. J. Zaluzec, S. Peng, S. Sun, H. Daimon, G. Wang, J. Greeley, J. Pearson, A. P. Paulikas, G. Karapetrov, D. Strmcnik, N. M. Markovic, V. R. Stamenkovic, *Nano Lett.*, 2011, **11**, 919-926.

13. C. Wang, M. Chi, D. Li, D. Strmcnik, D. van der Vliet, G. Wang, V. Komanicky, K.-C. Chang, A. P. Paulikas, D. Tripkovic, J. Pearson, K. L. More, N. M. Markovic, V. R. Stamenkovic, *J. Am. Chem. Soc.* **2011**, *133*, 14396-14403.

14. P. Strasser, S. Koh, T. Anniyev, J. Greeley, K. More, C. Yu, Z. Liu, S. Kaya, D. Nordlund, H. Ogasawara, M. F. Toney, A. Nilsson, *Nat. Chem.* **2010**, *2*, 454-460.

15. Z. R. Dai, S. Sun, Z. L. Wang, *Nano Lett.*, 2001, **1**, 443-447.

16. D. Wang, H. L. Xin, R. Hovden, H. Wang, Y. Yu, D. A. Muller, F. J. DiSalvo, H. D. Abruña, *Nat. Chem.* **2013**, 1*2*, 81-87.

17. M. Watanabe, K. Tsurumi, T. Mizukami, T. Nakamura, P. Stonehart, *J. Electrochem. Soc.* **1994**, *141*, 2659-2668.

18. H. Chen, D. Wang, Y. Yu, K. A. Newton, D. A. Muller, H. Abruña, F. J. DiSalvo, *J. Am. Chem. Soc.* **2012**, *134*, 18453-18459.

19. J. Kim, Y. Lee, S. Sun, *J. Am. Chem. Soc.* **2010**, *132*, 4996-4997.

20. S. Sun, C. B. Murray, D. Weller, L. Folks, A. Moser, *Science* **2000**, *287*, 1989-1992.

21. J. Kim, C. Rong, J. P. Liu, S. Sun, *Adv. Mater.* **2009**, *21*, 906-909.

22. S. Zhang, S. Guo, D. Su, S. Sun, *J. Am. Chem. Soc.* **2012**, *134*, 5060-5063.

23. J. Snyder, T. Fujita, M.W. Chen, J. Erlebacher, *Nat. Mater.* **2010**, *9*, 904-907.

24. R. Srivastava, P. Mani, N. Hahn, P. Strasser, *Angew. Chem. Int. Ed.* **2007**, *46*, 8988-8991.

25. A. V. Crewe, J. Wall, J. Langmore, *Science* **1970**, *168*, 1338-1340.

26. V. Stamenkovic, B. S. Mun, K. J. J. Mayrhofer, P. N. Ross, N. M. Markovic, J. Rossmeisl, J. Greeley, J. K. Nørskov, *Angew. Chem. Int. Ed.* **2006**, *45*, 2897-2901.

27. J. K. Nørskov, J. Rossmeisl, A. Logadottir, L. Lindqvist, J. R. Kitchin, T. Bligaard, H. Jonsson, *J. Phys. Chem. B* **2004**, *108*, 17886-17892.

28. X. Zhang, G. Lu, W. A. Curtin, *Phys. Rev. B* **2013**, *87*, 054113.

29. G. Kresse, J. Hafner, *Phys. Rev. B* **1993**, *47*, 558.

30. G. Kresse, J. Furthmuller, *Phys. Rev. B* **1996**, *54*, 11169.

31. P. E. Blochl, *Phys. Rev. B* **1994**, *50*, 17953.

32. J. P. Perdew, K. Burke, M. Ernzerhof, *Phys. Rev. Lett.* **1996**, *77*, 3865.

33. X. W. Zhou, R. A. Johnson, H. N. G. Wadley, *Phys. Rev. B* **2004**, *69*, 144113.

Chapter 4

Monodisperse Intermetallic FeCuPt Nanoparticles for Oxygen Reduction Reaction Catalysis

Using monodisperse bimetallic FePt nanoparticles (NPs) as an example in Chapter 3, we demonstrated the intermetallic ordered face centered tetragonal (*fct*) FePt NPs could show drastic enhancement in ORR catalysis comparing to traditional disordered face centered cubic (*fcc*) FePt NPs due to the intermetallic-induced optimization in surface strain and its related oxygen adsorption energy (E_o) for ORR. In this chapter, we further improve the NPs catalysis for ORR by extending this methodology to trimetallic FePtCu NPs. Similar to FePt NPs, trimetallic FePtCu NPs can be converted to FePtCu/Pt core/shell NPs by electrochemical dealloying. The Cu-substitution composition effect on structural control and electrochemical performance are also systematically studied. The best ORR catalysis occurs on the intermetallic $Fe_{25}Cu_{23}Pt_{52}$ NPs (half Fe atoms are substituted by Cu in *fct*-$Fe_{51}Pt_{49}$). With proper Cu-substitution in intermetallic FePt core, the strain in Pt shell is further optimized, leading to an E_o of -0.98 eV. This E_o is very close to the theoretical value of the ideal ORR catalyst (-1.0 eV).

4.1 Background and Motivation

Developing highly efficient and stable nanoparticles (NPs) catalysts for oxygen reduction reaction (ORR), the pivotal reaction for low temperature proton exchange membrane fuel cells (PEMFCs) and metal air batteries (MAB), strongly depends on the controlled synthesis of NPs. [1,2] As a typical catalyst choice, Pt-based NPs have been synthetically tuned in size, shape, compositions and even core/shell NPs. [3-13] By rational tuning, the Pt-based NPs can be tailored on the interface/surface energetics, leading to more favorable ORR catalytic dynamics with lower over-potential and energy loss. [2,14,15] Recently, FePt NPs with face-centered cubic (*fcc*) disordered structure and face-centered tetragonal (*fct*) intermetallic structure have been fabricated and further converted to FePt (*fcc* or *fct*)/Pt core/shell NPs through electrochemical dealloying. (Chapter 3) It has been demonstrated that the *fct*-FePt/Pt core/shell NPs show much enhanced ORR activity and durability comparing to *fcc*-FePt/Pt NPs due to the optimized surface Pt strain and the related oxygen adsorption energy (E_o) for ORR (*fct*-FePt/Pt: -0.97 eV, *fct*-FePt/Pt: -0.94 eV). Despite this progress, further advanced NPs catalysts with ideal surface E_o (-1.0 eV) are still highly desired for practical catalytic application. [16,17]

Here we develop a seed-mediated approach to monodisperse trimetallic FeCuPt NPs with Fe substituted by Cu in controlled composition. The trimetallic FeCuPt can be tuned with the *fcc* disordered phase and the *fct* intermetallic phase *via* high temperature annealing, and are further converted to FePtCu/Pt core/shell NPs through

electrochemical dealloying. Our previous study shows the *fct*-FePt/Pt NPs have less over-compression on Pt surface than *fcc*-FePt/Pt NPs. (Chapter 3) The Cu is chosen to substitute the Fe in *fct*-FePt because the proper Cu-substitution is subject to increase the crystalline lattice constant and further lower the over-compression. By studying Cu substitution-dependent and intermetallic-dependent ORR activity, the best ORR performance occurs in *fct*-$Fe_{25}Cu_{23}Pt_{52}$ NPs, which is calculated by the quantum mechanics-molecular mechanics (QM-MM) simulation to have an E_o of -0.98 eV, the closest one to the ideal E_o^a value of -1.0 eV among *fcc*-FePt, *fct*-FePt, *fcc*-FeCuPt NPs in the same condition.

4.2 Results and Discussion

4.2.1 Seed Mediated Synthesis of FeCuPt NPs

FePtCu NPs were produced via a seed mediated growth (see **Experimental**). In this synthesis, FePt NPs were first synthesized as seeds according to the method in Chapter 3. [18-20] These FePt NPs can be controlled in composition to generate different Fe-deficient FePt alloy NPs. For example, we synthesized $Fe_{42}Pt_{58}$, $Fe_{33}Pt_{67}$ and $Fe_{27}Pt_{73}$ NPs as a set of seeds. The as-synthesized FePt NPs seed are nanocubes with a size of 8.5 nm $\pm$ 0.5 nm, as shown in Chapter 3. In the seed mediated synthesis, the copper acetylacetonate, $Cu(acac)_2$, was reduced by oleylamine and simultaneously deposited on these Fe-deficient FePt seeds, while aging solution at high temperature (240 °C) facilitated the atomic diffusion to yield ternary alloy NPs.

(see **Experimental**). [9, 21] Our study showed the trimetallic composition can be readily tuned by choosing FePt NPs with different Fe-deficiency and the ratio of seed/M precursor. **Table. 4-1** summarized the correlation between the synthetic condition and the final FeCuPt product. We can see the FeCuPt NPs nearly preserve the Fe/Pt ratio in the seeds and proper amount of $Cu(acac)_2$ can produce the FeCuPt with a composition of (Fe+Cu):Pt=1:1 ($Fe_{38}Cu_{15}Pt_{47}$, $Fe_{25}Cu_{23}Pt_{52}$ and $Fe_{19}Cu_{35}Pt_{46}$). The Fe:Pt=1:1 NPs ($Fe_{42}Pt_{58}$) were also synthesized as a control. Considering the Fe:Pt=1:1 is the best composition for *fcc-fct* transformation, these (Fe+Cu):Pt=1:1 NPs are ideal for systematic study of Cu-substitution effect on the ORR catalysis of intermetallic FePt NPs.

Sample	FePt seeds	As-synthesized FeCuPt
A	$Fe_{42}Pt_{58}$	$Fe_{38}Cu_{15}Pt_{47}$
B	$Fe_{33}Pt_{67}$	$Fe_{25}Cu_{23}Pt_{52}$
C	$Fe_{27}Pt_{73}$	$Fe_{19}Cu_{35}Pt_{46}$

Table 4-1. The composition control of as-synthesized FeCuPt NPs by choosing the FePt NPs seeds with different Fe-deficiency.
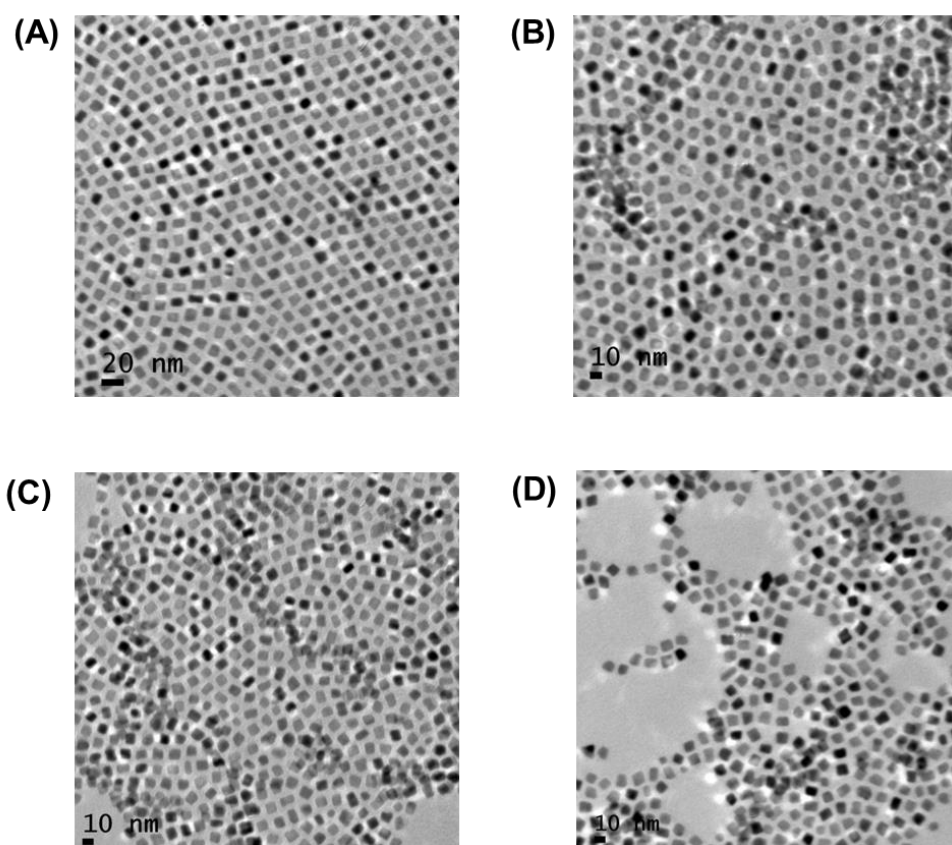
Figure 4-1. TEM images of the as-synthesized $Fe_{51}Pt_{49}$ (**A**), $Fe_{38}Cu_{15}Pt_{47}$ (**B**), $Fe_{25}Cu_{23}Pt_{52}$ (**C**) and $Fe_{19}Cu_{35}Pt_{46}$ (**D**) NPs.

Figure 4-1A-D shows the transmission electron microscopy (TEM) images of the as-synthesized $Fe_{51}Pt_{49}$ (**A**), $Fe_{38}Cu_{15}Pt_{47}$ (**B**), $Fe_{25}Cu_{23}Pt_{52}$ (**C**) and $Fe_{19}Cu_{35}Pt_{46}$ (**D**) NPs. After Cu doping, trimetallic FeCuPt NPs are still the monodisperse cubes with an average size of 8.5 nm ± 0.5 nm. To track the seed mediated growth of trimetallic NPs, the NPs products were separated at 180 °C, 210 °C and 240 °C, and characterized by TEM and ICP-AES, as show in **Figure 4-2** and **Table 4-2**. Apparently, the FeCuPt trimetallic composition and morphology are fixed at 180 °C, and further diffusion at 240 °C can only promote the formation of better alloy.

Temperature, °C	FeCuPt composition
180	$Fe_{25}Cu_{23}Pt_{52}$
210	$Fe_{25}Cu_{23}Pt_{52}$
240	$Fe_{25}Cu_{23}Pt_{52}$

Table 4-2. The composition change of FeCuPt NPs during seed mediated growth. The NPs products were collected in the middle of synthesis at different temperatures.
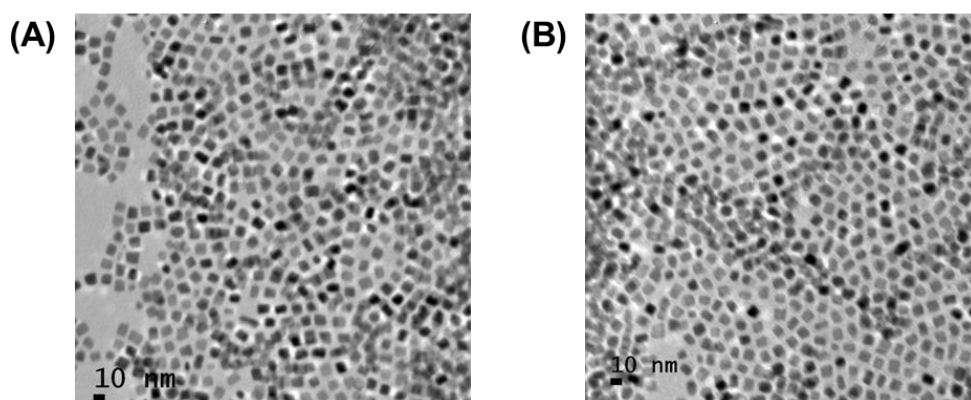
Figure 4-2. TEM images of the $Fe_{25}Cu_{23}Pt_{52}$ NPs collected in the middle of synthesis at 180 °C and 210 °C.

4.2.2 Structural Control of FeCuPt NPs

It is known that high temperature annealing can facilitate the phase transformation from the *fcc*-FePt to *fct*-FePt. [18-21] We loaded our FeCuPt NPs on Ketjen carbon (C) support (C-NPs) and then treated them under 95% Ar + 5% H_2 at 400 °C & 650 °C for 1 h (see **Experimental**), after which we indeed observed the conversion from

disordered NPs to intermetallic NPs. **Figure 4-3** shows the X-ray diffraction (XRD) patterns of $Fe_{38}Cu_{15}Pt_{47}$, $Fe_{25}Cu_{23}Pt_{52}$ and $Fe_{19}Cu_{35}Pt_{46}$ annealed at 400 °C & 650 °C. At 400 °C, the FeCuPt NPs are still in *fcc* phase. After annealing at 650°C, $Fe_{38}Cu_{15}Pt_{47}$, $Fe_{25}Cu_{23}Pt_{52}$ NPs are transformed into *fct* structure with apparent super-lattice peaks at 24, 33°, while $Fe_{19}Cu_{35}Pt_{46}$ NPs show no obvious *fcc-fct* transition. This means substituting too much Fe by Cu can prevent the formation of intermetallic ordering, which was also reported in previous thin film study. [23-26]
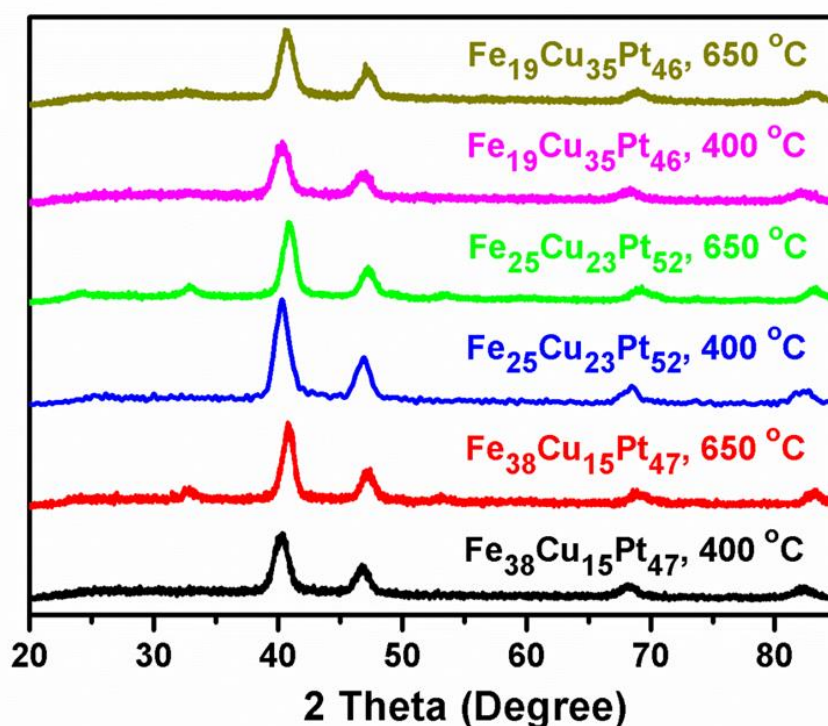
Figure 4-3. XRD patterns of the $Fe_{38}Cu_{15}Pt_{47}$, $Fe_{25}Cu_{23}Pt_{52}$ and $Fe_{19}Cu_{35}Pt_{46}$ NPs annealed at 400 °C, 650 °C. The NPs were first deposited on the Ketjen carbon support and then annealed under 95% Ar + 5% H_2 for 1 h.

Figure 4-4 shows the representative TEM images of the $Fe_{25}Cu_{23}Pt_{52}$ NPs annealed at 400 °C & 650 °C. Because of the protection of C support, there is no sintering/aggregation are found after high temperature treatment, but cubic morphology is changed to polyhedron which was also observed in previous FePt study (Chapter 3). On the other hand, this high temperature annealing also functions to remove the organic surfactant on the NPs, making the clean surface for electrochemical study. [21]
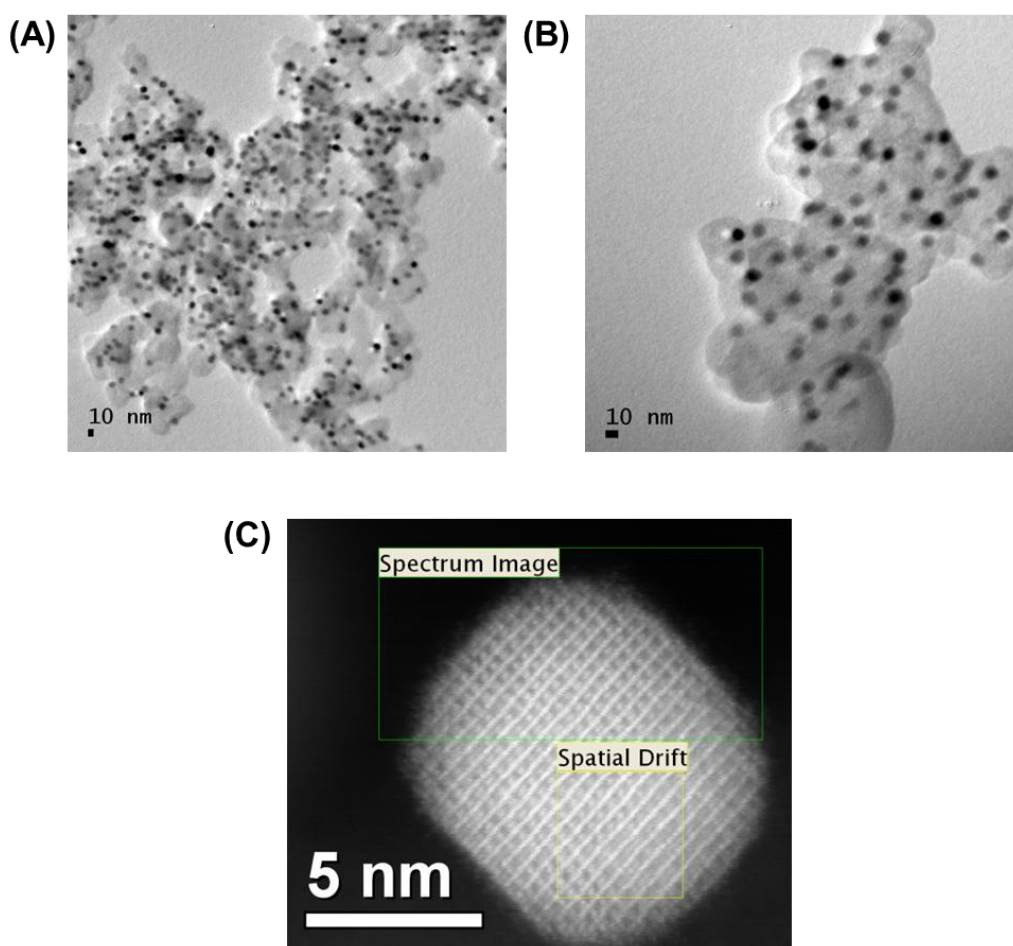
Figure 4-4. (**A**, **B**) TEM images of the $Fe_{25}Cu_{23}Pt_{52}$ NPs annealed at 400 ℃ (**A**), 650 ℃ (**B**). (**C**) HAADF-STEM images of the $Fe_{25}Cu_{23}Pt_{52}$ NPs annealed at 650 ℃.

The formation of intermetallic FeCuPt can also be characterized by atomically resolved aberration-corrected scanning transmission electron microscopy (STEM). **Figure 4-4C** shows the high-angle annular dark field (HAADF)-STEM image of the $Fe_{25}Cu_{23}Pt_{52}$ NPs annealed 650 °C, in which the characteristic intermetallic alloy superlattice view along [001] direction can be clearly seen. Considering the nature of Z-contrast of Fe, Cu and Pt, Pt columns with higher brightness can be easily visualized in this superlattice array. [27]

4.2.3 Electrochemical Dealloying of FeCuPt NPs

Electrochemical dealloying has been demonstrated as an efficient approach to etching active metals M (e. g. Cu, Fe, Co, Ni etc.) from their MPt alloys to form MPt/Pt core/shell structure. [8, 9, 12, 13, 28] We use this method to produce the FeCuPt/Pt core/shell NPs as well as to obtain an electrochemical stable/clean surface (Pt-rich shell). The annealed C-NPs were dispersed in deionized water + isopropanol + 5% Nafion and then were transferred onto the glassy carbon (GC) surface of a rotating disk electrode (RDE). The electrochemical dealloying was consuming by sweeping cyclic voltammograms (CVs) from -0.2 V to 1.0 V (vs. Ag/AgCl) for 100 cycles in the N_2-saturated 0.1 M $HClO_4$ solution. The core/shell structure formation can be

confirmed by the STEM-electron energy loss spectroscopy (STEM-EELS) elemental

mapping. **Figure 4-5** show HADDF-STEM images of dealloyed *fcc-* and *fct*-

$Fe_{25}Cu_{23}Pt_{52}$ NPs and their STEM-EELS line scan. In both NPs, a Pt-rich shell with a

thickness of around 0.6 nm (around 3 atomic layers) can be clearly seen. For the *fct*

fct-$Fe_{25}Cu_{23}Pt_{52}$ NPs, the line scan in the core region exhibits the characteristic

intermetallic Pt, Fe (or Cu) layer-by-layer energy profile, while the line scan in the

shell region confirms the disordered Pt energy profile.
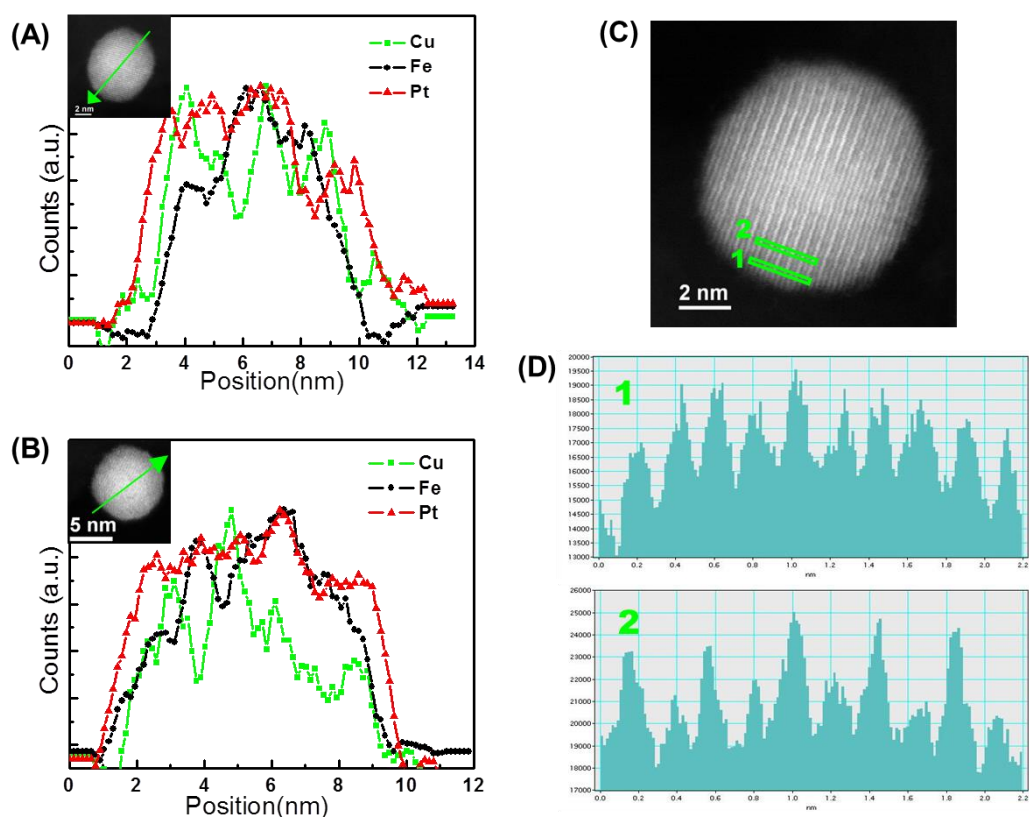
Figure 4-5. (**A, B**) STEM-EELS line scan crossing the dealloyed $Fe_{25}Cu_{23}Pt_{52}$ NPs annealed at 400 ℃ (**A**) and 650 ℃ (**B**). The insets show the NP scanned. (**C**) HAADF-STEM image of a representative dealloyed $Fe_{25}Cu_{23}Pt_{52}$ NPs annealed at 650 ℃. (**D**) STEM-EELS line scan in the core and shell region on the NPs of (C).

4.2.4 Electrocatalysis of *fct*- and *fcc*-FePt NPs

Figure 4-6A & **B** show the CVs of FeCuPt/Pt core/shell NPs obtained from *fcc*-FeCuPt (**A**) and *fct*-FeCuPt (**B**) in the N_2-saturated 0.1 M $HClO_4$ solution with a sweep rate of 50 mV/s. These CV curves present typical peaks related to hydrogen underpotential formation/stripping on Pt surface in the potential range from -0.2 V to 0.2 V (vs Ag/AgCl) and Pt oxidization/reduction above 0.4 V. We use the hydrogen underpotential desorption (H_{upd}) peaks to evaluate the electrochemically active surface area (ECASA) of these Pt-based catalyst. [9, 29] The ORR polarization curves of these NPs catalysts are tested with the same Pt mass loading at room temperature in O_2-saturated 0.1 M $HClO_4$ with a sweep rate of 10 mV/s and a rotation speed of 1600 rpm, as show in **Figure 4-6C** & **D**. The ORR polarization curves include the diffusion-limiting current region ranging from −0.1 to 0.4 V and the mixed kinetic−diffusion control region between ~0.4 and ~0.7 V. We can easily find all the Cu-substituted FeCuPt NPs catalysts exhibit the positive shifted curves comparing to FePt NPs in both *fcc* (**Figure 4-6C**) and *fct* phases (**Figure 4-6D**), suggesting the Cu-substitution in NPs truly increase the ORR activity. On the other hand, the *fct* NPs exhibit the higher half-wave potentials than their *fcc* NPs counterpart in all compositions. Among them, *fct*-$Fe_{25}Cu_{23}Pt_{52}$ shows the highest half-wave potential at 0.574 mV, 43 mV higher than commercial C-Pt catalyst (0.531 mV).

We further evaluated ORR activity of each NPs catalyst by using mass-transport correction and normalizing the kinetic current to ECASA and Pt loading. **Figure**

4-6E&F compare the specific activities (at 531 mV and 574 mV) of NPs in *fcc* (**E**) and *fct* phases (**F**). In *fcc* phase, substituting more Cu leads to the higher specific activity, which is consistent to our prediction that Cu-substitution can relieve the surface Pt over-compression. But in *fct* phase, the specific activity of FeCuPt NPs displays a "volcano" trend with respect to Cu-substitution amount. The proper Cu-substitution ($Fe_{38}Cu_{15}Pt_{47}$ and $Fe_{25}Cu_{23}Pt_{52}$) is favorable to the ORR catalysis. Too much of Cu-substitution ($Fe_{19}Cu_{35}Pt_{46}$) is undesired, which is very likely be caused by the poor *fcc-fct* transition in this composition as indicated by XRD pattern above (**Figure 4-3**). The best *fct*-$Fe_{25}Cu_{23}Pt_{52}$ reaches the specific activity of 2.55 mA/cm^2 at 0.531 V and 0.690 mA/cm^2 at 0.574 V, much higher than *fct*-$Fe_{51}Pt_{49}$ (2.10 mA/cm^2 at 0.531 V and 0.410 mA/cm^2 at 0.574 V) and *fcc*-$Fe_{25}Cu_{23}Pt_{52}$ (1.09 mA/cm^2 at 0.531 V and 0.261 mA/cm^2 at 0.574 V) and commercial C-Pt (0.264 mA/cm^2 at 0.531 V and 0.08 mA/cm^2 at 0.574 V). Moreover, the *fct*-$Fe_{25}Cu_{23}Pt_{52}$ exhibit the mass activity of 549 mA/mg at 0.531 V (148 mA/cm^2 at 0.574 V), while *fct*-$Fe_{51}Pt_{49}$ can only show 484 mA/mg at 0.531 V (95 mA/cm^2 at 0.574 V).
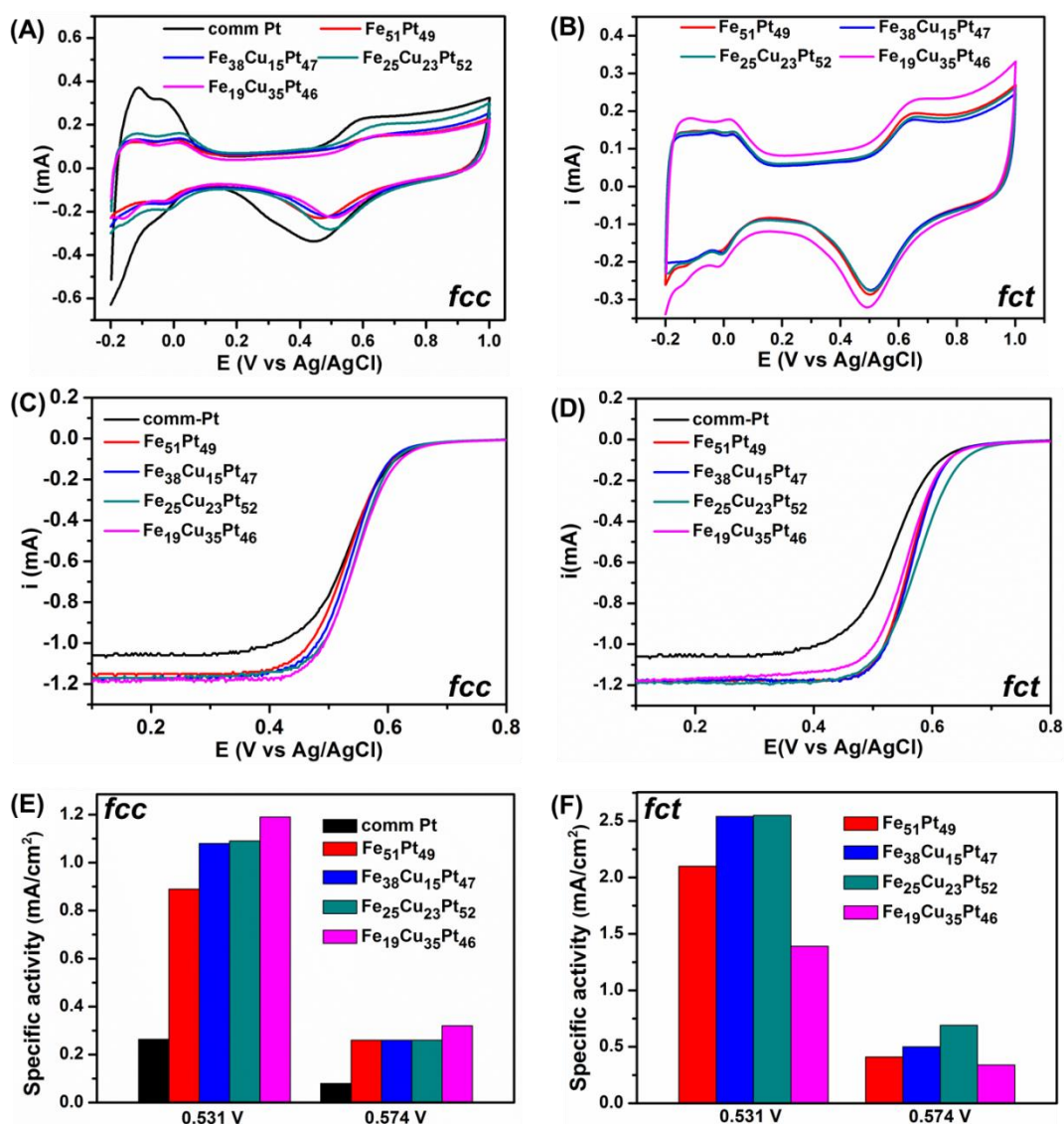
Figure 4-6. (**A**) CVs of the C-Pt, *fcc*-Fe$_{51}$Pt$_{49}$, *fcc*-Fe$_{38}$Cu$_{15}$Pt$_{47}$, *fcc*-Fe$_{25}$Cu$_{23}$Pt$_{52}$ and *fcc*-Fe$_{19}$Cu$_{35}$Pt$_{46}$ NPs in N$_2$-saturated 0.1 M HClO$_4$ with a scan rate of 50 mV/s. (**B**) CVs of the *fct*-Fe$_{51}$Pt$_{49}$, *fct*-Fe$_{38}$Cu$_{15}$Pt$_{47}$, *fct*-Fe$_{25}$Cu$_{23}$Pt$_{52}$ and *fct*-Fe$_{19}$Cu$_{35}$Pt$_{46}$ NPs in N$_2$-saturated 0.1 M HClO$_4$ with a scan rate of 50 mV/s. (**C**) ORR polarization curves of C-Pt, *fcc*-Fe$_{51}$Pt$_{49}$, *fcc*-Fe$_{38}$Cu$_{15}$Pt$_{47}$, *fcc*-Fe$_{25}$Cu$_{23}$Pt$_{52}$ and *fcc*-Fe$_{19}$Cu$_{35}$Pt$_{46}$ NPs in O$_2$-saturated 0.1 M HClO$_4$ with a scan rate of 10 mV/s and a rotation speed of 1600 rpm. (**D**) ORR polarization curves of C-Pt, *fcc*-Fe$_{51}$Pt$_{49}$, *fcc*-Fe$_{38}$Cu$_{15}$Pt$_{47}$, *fcc*-Fe$_{25}$Cu$_{23}$Pt$_{52}$ and *fcc*-Fe$_{19}$Cu$_{35}$Pt$_{46}$ NPs in O$_2$-saturated 0.1 M HClO$_4$ with a scan rate of 10 mV/s and a rotation speed of 1600 rpm. (**E, F**) Specific activities of *fcc* NPs (**E**) and *fct* NPs (**F**) at 0.531V and 0.574 V.

The *fct*-Fe$_{25}$Cu$_{23}$Pt$_{52}$ NPs catalyst also shows good stability in current ORR condition. We sweep the NPs between 0.4 and 0.7 V (vs Ag/AgCl) in the O$_2$-saturated 0.1 M HClO$_4$ with a scan rate of 100 mV/s. After 10000 sweeps, there is

no visible morphology change of NPs as indicated by TEM image in **Figure 4-7A**.

We also studied the CVs and ORR polarization curves of fct-$Fe_{25}Cu_{23}Pt_{52}$ NPs after

10000 sweeps (**Figure 4-7B & C**). Clearly, no drops of H_{upd} peaks and no shift of

ORR polarization curves suggest the good long-term stability of this catalyst.
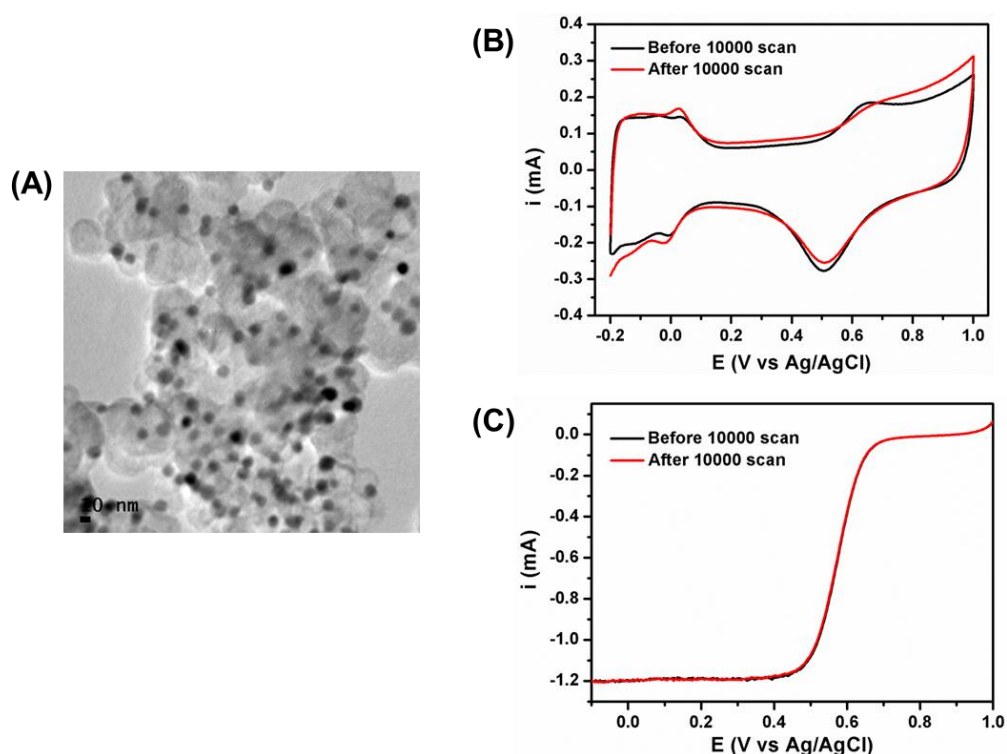
Figure 4-7. (**A**) TEM image of the fct-$Fe_{25}Cu_{23}Pt_{52}$ NPs after stability test of 10000 potential sweeps between 0.4-0.7 V vs. Ag/AgCl. (**B**) CVs and (**C**) ORR polarization curves of the fct-$Fe_{25}Cu_{23}Pt_{52}$ NPs before and after 10000 potential sweeps between 0.4-0.7 V vs. Ag/AgCl.

4.2.5 Theoretical Calculation for Enhancement Mechanism

The best fct-$Fe_{25}Cu_{23}Pt_{52}$ NPs were further simulated by the quantum

mechanics-molecular mechanics (QM-MM) calculations based on core/shell NPs

modal. To simplify the calculation, we constructed the core-shell NPs model with a

shell of of *fcc*-Pt (3 atomic layers) and a core of either *fcc*-Fe$_{25}$Cu$_{25}$Pt$_{50}$ or *fct*-Fe$_{25}$Cu$_{25}$Pt$_{50}$ alloy. The structure of the core FeCuPt is displayed in **Figure 4-8A&B**. We can see the Cu-substitution in FePt indeed expands the crystal interplanar distance, as summarized in **Table 4-2**. We predict this crystalline lattice expansion induced by both Cu-substitution and *fcc-fct* transition could function to lower the overcompression in FePt/Pt core/shell NPs. The 8 nm core/shell FeCuPt/Pt NPs model is provided in **Figure 4-8C&D**. Based on them, the surface oxygen adsorption energy (E$_o$) of *fct*-Fe$_{25}$Cu$_{25}$Pt$_{50}$/Pt is simulated to be -0.98 eV, the closet one to the ideal value of -1.0 among *fcc*-Fe$_{25}$Cu$_{25}$Pt$_{50}$/Pt, *fcc-* and *fct*-Fe$_{50}$Pt$_{50}$/Pt (**Table 4-3**). The optimized E$_o$ make the *fct*-Fe$_{25}$Cu$_{25}$Pt$_{50}$/Pt have the balanced interphase energetics for the contradictory adsoption and desorption to oxygenated intermediate in the ORR. The theoretical E$_o$ also completely supports the ORR actvity trend we observed aforementioned, in which the *fct*-Fe$_{25}$Cu$_{23}$Pt$_{52}$/Pt possess the best ORR performance by combining proper Cu-substitution with the satisfactory formation of intermetallic structure.
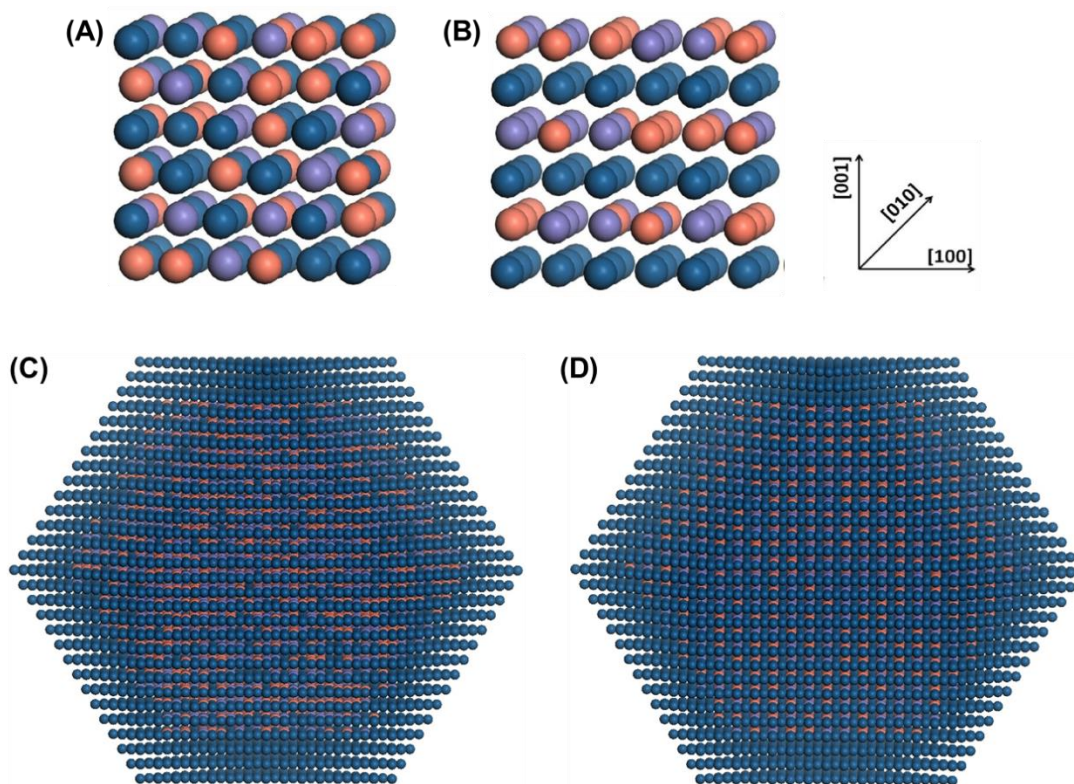
Figure 4-8. (**A**, **B**) 8 nm cuboctahedral FeCuPt/Pt core/shell NPs models constructed for QM-MM calculations. (**A**) model of *fcc*-FeCuPt/Pt core/shell NPs with 7667 Pt atoms, 1283 Fe atoms and 1229 Cu atoms. (**B**) model of *fct*-FePt/Pt core/shell NPs with 7704 Pt atoms 1250 Fe atoms and 1225 Cu atoms. Two models have a core composition of ~$Fe_{25}Cu_{25}Pt_{50}$ and a three-atomic-layer shell of Pt. (**C**, **D**) Periodic supercells consisting of 108 atoms used to simulate atomic structure of *fcc*-FeCuPt (**C**) and *fct*-FeCuPt (**D**). The blue, purpul and orange balls stand for Pt, Fe and Cu atoms, respectively.

core	$a_{[100]}/a_{Pt}$	$a_{[010]}/a_{Pt}$	$a_{[001]}/a_{Pt}$
fcc-FePt	0.961	0.964	0.965
fct-FePt	0.971	0.971	0.945
fcc-FeCuPt	0.967	0.963	0.967
fct-FeCuPt	0.986	0.985	0.950

Table 4-2. The lattice constant comparison of FeCuPt and FePt. a_{Pt} is the lattice constant of *fcc*-Pt.

$a_{[100]}$, $a_{[010]}$, $a_{[001]}$ are the calculated interplanar distances along [100], [010] and [001] directions of each NP.

NPs	E_o (eV)
fcc-FeCuPt/Pt	-0.95
fct-FeCuPt/Pt	-0.98
fcc-FePt/Pt	-0.94
fct-FePt/Pt	-0.97
Ideal value	-1.0
Pt	-1.2

Table 4-3. The calculated E_o of *fcc*-FeCuPt/Pt, *fct*-FeCuPt/Pt, *fcc*-FePt/Pt, *fct*-FePt/Pt, Pt. The ideal value is based on reference [16, 17]

4.3 Summary

In summary, we have developed a robust approach to monodisperse FeCuPt NPs with tunable Cu composition and controlled crystalline structures (*fcc* and *fct*). After electrochemical dealloying, the FeCuPt NPs can be converted into core/shell structured FeCuPt/Pt NPs with a structure-controlled FeCuPt core surrounded by three atomic layers of Pt. These FeCuPt/Pt NPs show unique Cu-substitution dependent and FeCuPt-structure dependent ORR catalytic activities. By combining the proper Cu-substitution amount and desirable intermetallic (*fct*) structure, the fct-

fct-Fe$_{25}$Cu$_{23}$Pt$_{52}$/Pt NPs exhibit the best ORR activity and durability among all the FePt and FeCuPt tested. The QM-MM calculation reveals the *fct*-FeCuPt/Pt NPs have an optimized surface strain and an E$_o$ at -0.98 eV which is the closest to the ideal value of -1.0 eV among *fcc*-FeCuPt/Pt, *fcc*- and *fct*-FePt/Pt NPs. This structure-control and composition-control strategy can potentially extended to other multimetallic alloy systems, providing a new predictable model to optimize NPs catalytic activity and durability for practical catalytic applications.

4.4 Experimental

Chemicals and Materials. Oleylamine (OAm, >70%), oleic acid (OA), 1-octadecene (ODE), Pt(acac)$_2$ (acac = aceylacetonate), Cu(acac)$_2$, iron pentacarbonyl (Fe(CO)$_5$), hexane, isopropanol, ethanol, and Nafion (5%) were all purchased from Sigma Aldrich and used without further purification. C-Pt (20% mass loading with a diameter of 2.5-3.5 nm) catalyst was obtained from Fuel Cell Store.

Characterization. XRD characterizations were carried out on a Bruker AXS D8-Advanced diffractometer with Cu Kα radiation (λ =1.5418 Å). TEM images were obtained from a Philips CM 20 operating at 200 kV. STEM analyses were carried out using a Hitachi HD2700C (200kV) with a probe aberration-corrector, in the Center for Functional Nanomaterials at Brookhaven National Lab. The EELS line-scan was obtained by a high resolution Gatan-Enfina ER with a probe size of 1.3Å. A power

law function was used for EELS background subtraction. TEM and HRTEM samples were prepared by depositing a single drop of diluted NPs dispersion on amorphous carbon coated copper grids. The inductively coupled plasma-atomic emission spectroscopy (ICP-AES) measurements were carried on a JY2000 Ultrace ICP Atomic Emission Spectrometer equipped with a JY AS 421 autosampler and 2400g/mm holographic grating. Electrochemical measurements were performed on a Autolab 302 potentiostat (5 mm GC). Ag/AgCl was used as a reference electrode and platinum wire as a counter electrode.

Synthesis of FeCuPt Nanoparticles (NPs). The FePt NPs seeds are first synthesized according to the method described in Chapter 3. To synthesize the FeCuPt NPs, ODE (15 mL), oleylamine (2 ml) and $Cu(acac)_2$ (14 mg) were mixed in a four-necked flask. The mixture was magnetically stirred and heated to 80 ℃ to generate a bluish green transparent solution under a gentle flow of N_2. Then 40 mg $Fe_{42}Pt_{58}$ NPs (hexane dispersion) was added into the solution. The solution was heated to 240 ℃ at a rate of about 3 ℃ /min and kept at this temperature for 1 hour before it was cooled to room temperature. The NPs were separated by adding isopropanol (50 mL), followed by centrifugation (8500 rpm, 8 min). The NPs were further purified by dispersing into hexane (20 mL) and centrifugation (5000 rpm, 3 min) to remove any un-dispersed precipitates. The product was precipitated out by adding ethanol (50 mL) and centrifugation (8500 rpm, 8 min) and re-dispersed in hexane. The synthesis yielded $Fe_{38}Cu_{15}Pt_{47}$ NPs. In the same reaction condition, 18 mg of $Cu(acac)_2$ and 40 mg of $Fe_{34}Pt_{66}$ seeds led to the formation of $Fe_{25}Cu_{23}Pt_{52}$ NPs. 24 mg of $Cu(acac)_2$ and 40

mg of $Fe_{27}Pt_{73}$ seeds yielded $Fe_{19}Cu_{35}Pt_{46}$ NPs

Catalyst Preparation. The as-synthesized NPs and Ketjen-300 J carbon at the weight ratio of 1:2 were mixed in 20 mL mixture of hexane and sonicated for 1 h to deposit NPs on carbon. The product was separated by centrifugation (8500 rpm, 3 min). The NPs-C were dried under ambient conditions and annealed at different temperatures for 1 h in a gas flow of Ar + 5% H_2. The product was then redispersed in a mixture of deionized water, isopropanol and Nafion (V/V/V = 4/1/0.05). 20 μL catalyst ink (2 mg/mL) was deposited on the working electrode (glassy carbon rotating disk electrode, GC-RDE) that was polished prior to catalyst deposition by 0.1 μm and 0.05 μm alumina powder and rinsed by sonication in ethanol and in deionized water. The catalyst was dried at ambient condition.

Electrochemical Measurements. Cyclic voltammograms (CVs) were obtained by scaning between -0.2 V-1 V *vs* Ag/AgCl at a scan rate of 50 mV/s in N_2-saturated 0.1M $HClO_4$. ORR polarization curves were obtained by scaning the potentials from 1.0 to -0.1 V *vs* Ag/AgCl at a scan rate of 10 mV/s in O_2-saturated 0.1 M $HClO_4$ with the GC-RDE rotating at 1600 rpm.

Theoretical Calculation.

I. E_O **for Core/Shell Nanoparticles (NPs)**

Core/shell NPs are modeled by cuboctahedrons with eight (111) facets and six (100) facets as shown in Chapter 3 and **Figure 3-9**. The core/shell structure consists of pure Pt shell and FePtCu alloy core. The size of NPs is 8 nm corresponding to 10179 atoms in total. E_O is determined by placing an O atom at the *fcc*-hollow site on the (111) facet, which is calculated by

$$E_O = E_{QM/MM}[NP+O] - E_{QM/MM}[NP] - \frac{1}{2}E_{QM}[O_2] \qquad (1)$$

where $E_{QM/MM}[NP+O]$ and $E_{QM/MM}[NP]$ are total energies of NPs with and without O adsorbate, respectively obtained from quantum mechanics-molecular mechanics (QM-MM) calculations. $E_{QM}[O_2]$ is the total energy of an O_2 molecule calculated by the stand-alone density functional theory (DFT).

In QM/MM calculations, as shown in **Figure 4-9**, the entire modeled system is partitioned into two spatial domains: a QM region treated by constrained DFT and a MM region by empirical atomistic simulations. The QM region is further divided into an interior QM region and a boundary QM region. The former involves bond breaking, chemical reaction and charge transfer, etc. where topological changes of charge density take place. The latter serves as a buffer region where no such topological change to the charge density occurs. The technical details and validations of the QM/MM method can be found elsewhere [30]. The QM region measures 17Å×17Å×8Å in x, y, and z directions, respectively with 195 atoms, where the innermost 8.4Å×7.3Å×4Å is the interior QM region containing the *fcc*-hollow site for oxygen adsorption. The MM region consists of the rest of the system where the strain

effect due to the lattice mismatch between core and shell is captured. The DFT calculations are performed using the VASP package [31, 32] with the projector augmented wave pseudopotentials [33] and Perdew-Burke-Ernzerhof generalized gradient approximation (PBE-GGA) [34]. The calculations are performed at Γ point with 400 eV energy cutoff. The embedded atom method (EAM) potentials [35] are used in the MM simulations, which have been rescaled to yield the same lattice constant and bulk modulus as those of DFT. The atomic relaxation is carried out with the conjugate-gradient algorithm and the force convergence criterion is 0.03 eV/Å.

II. Lattice Constant of Two Core Structures

A periodic supercell consisting of 108 atoms is used to simulate atomic structure of FeCuPt core materials. All atoms are fully relaxed under the constant (zero) pressure by using stand-alone DFT calculations with an energy cutoff of 280 eV and a $3 \times 3 \times 3$ k-point mesh. For fcc-FeCuPt, 50%, 25% and 25% atoms are randomly selected to be Pt, Fe and Cu atoms, respectively. As shown in **Figure 4-8A**, there are 52 Pt atoms, 27 Fe atoms and 29 Cu atoms. For fct-FeCuPt, Pt and Fe (or Cu) atoms are distributed layer by layer. There are 54 Pt atoms, 28 Fe atoms and 26 Cu atoms in the model of **Figure 4-8B**.

Reference

1. H. Yang, *Angew. Chem. Int. Ed.* **2011**, *50*, 2674-2676.

2. S. Guo, S. Zhang, S. Sun, *Angew. Chem. Int. Ed.* **2013**, DOI: anie.201207186.

3. C. Wang, H. Daimon, T. Onodera, T. Koda, S. Sun, *Angew. Chem. Int. Ed.* **2008**, *47*, 3588-3591.

4. C. Wang, D. van der Vliet, K.-C. Chang, H. You, D. Strmcnik, J. A. Schlueter, N. M. Markovic, V. R. Stamenkovic, *J. Phys. Chem. C* **2009**, *113*, 19365-19368.

5. C. Wang, M. Chi, D. Li, D. van der Vliet, G. Wang, Q. Lin, J. F. Mitchell, Karren L. More, N. M. Markovic, V. R. Stamenkovic, *ACS Catal.* **2011**, *1*, 1355-1359.

6. J. Zhang, H. Yang, J. Fang, S. Zou, *Nano Lett.* **2010**, *10*, 638-644.

7. J. Wu, L. Qi, H. You, A. Gross, J. Li, H. Yang, *J. Am. Chem. Soc.* **2012**, *134*, 11880-11883.

8. S. Guo, D. Li, H. Zhu, S. Zhang, N. M. Markovic, V. R. Stamenkovic, *Angew. Chem. Int. Ed.* **2013**, *52*, 3465-3468.

9. H. Zhu, S. Zhang, S. Guo, D. Su, S. Sun, *J. Am. Chem. Soc.* **2013**, *135*, 7130-7133.

10. K. Sasaki, H. Naohara, Y. Cai, Y. M. Choi, P. Liu, M. B. Vukmirovic, J. X. Wang, R. R. Adzic, *Angew. Chem. Int. Ed.*, **2010**, *49*, 8602-8607.

11. C. Wang, D. van der Vliet, K. L. More, N. J. Zaluzec, S. Peng, S. Sun, H. Daimon, G. Wang, J. Greeley, J. Pearson, A. P. Paulikas, G. Karapetrov, D. Strmcnik, N. M. Markovic, V. R. Stamenkovic, *Nano Lett.*, 2011, **11**, 919-926.

12. C. Wang, M. Chi, D. Li, D. Strmcnik, D. van der Vliet, G. Wang, V. Komanicky, K.-C. Chang, A. P. Paulikas, D. Tripkovic, J. Pearson, K. L. More, N. M. Markovic, V. R. Stamenkovic, *J. Am. Chem. Soc.* **2011**, *133*, 14396-14403.

13. P. Strasser, S. Koh, T. Anniyev, J. Greeley, K. More, C. Yu, Z. Liu, S. Kaya, D. Nordlund, H. Ogasawara, M. F. Toney, A. Nilsson, *Nat. Chem.* **2010**, *2*, 454-460.

14. V. R. Stamenkovic, B. S. Mun, M. Arenz, K. J. J. Mayrhofer, C. A. Lucas, G. Wang, P. N. Ross, N. M. Markovic, *Nat. Mater.* **2007**, *6*, 241-247.

15. V. R. Stamenkovic, B. Fowler, B. S. Mun, G. Wang, P. N. Ross, C. A. Lucas, N. M. Markovic, *Science* **2007**, *315*, 493-497.

16. V. Stamenkovic, B. S. Mun, K. J. J. Mayrhofer, P. N. Ross, N. M. Markovic, J. Rossmeisl, J. Greeley, J. K. Nørskov, *Angew. Chem. Int. Ed.* **2006**, *45*, 2897-2901.

17. J. K. Nørskov, J. Rossmeisl, A. Logadottir, L. Lindqvist, J. R. Kitchin, T. Bligaard, H. Jonsson, *J. Phys. Chem. B* **2004**, *108*, 17886-17892.

18. J. Kim, Y. Lee, S. Sun, *J. Am. Chem. Soc.* **2010**, *132*, 4996-4997.

19. S. Sun, C. B. Murray, D. Weller, L. Folks, A. Moser, *Science* **2000**, *287*, 1989-1992.

20. J. Kim, C. Rong, J. P. Liu, S. Sun, *Adv. Mater.* **2009**, *21*, 906-909

21. S. Zhang, S. Guo, D. Su, S. Sun, *J. Am. Chem. Soc.* **2012**, *134*, 5060-5063.

22. T. Maeda, T. Kai, A. Kikitsu, T. Nagase, J.-I. Akiyama, *Appl. Phys. Lett.* **2002**, *80*, 2147-2149.

23. T. Kai, T. Maeda, A. Kikitsu, J. Akiyama, T. Nagase, T. Kishi, *J. Appl. Phys.* **2004**, *95*, 609-612.

24. Y. K. Takahashi, M. Ohnuma, K. Hono, *J. Magn. Magn. Mater.* **2002**, *246*, 258.

25. X. C. Sun, S. S. Kang, J. W. Harrell, D. E. Nikles, *J. Appl. Phys.* **2003**, *93*, 7337.

26. D. A. Gilbert, L.-W. Wang, T. J. Klemmer, J.-U. Thiele, C.-H. Lai, K. Liu, *Appl. Phys. Lett.* **2013**, *102*, 132406-132409.

27. A. V. Crewe, J. Wall, J. Langmore, *Science* **1970**, *168*, 1338-1340.

28. R. Srivastava, P. Mani, N. Hahn, P. Strasser, *Angew. Chem. Int. Ed.* **2007**, *46*, 8988-8991.

29. J. Snyder, T. Fujita, M.W. Chen, J. Erlebacher, *Nat. Mater.* **2010**, *9*, 904-907.

30. X. Zhang, G. Lu, W. A. Curtin, *Phys. Rev. B* **2013**, *87*, 054113.

31. G. Kresse, J. Hafner, *Phys. Rev. B* **1993**, *47*, 558.

32. G. Kresse, J. Furthmuller, *Phys. Rev. B* **1996**, *54*, 11169.

33. P. E. Blochl, *Phys. Rev. B* **1994**, *50*, 17953.

34. J. P. Perdew, K. Burke, M. Ernzerhof, *Phys. Rev. Lett.* **1996**, *77*, 3865.

35. X. W. Zhou, R. A. Johnson, H. N. G. Wadley, *Phys. Rev. B* **2004**, *69*, 144113.

Chapter 5

Synthetic Control of FePtM Nanorods (M = Cu, Ni) to Enhance Oxygen Reduction Reaction

In Chapter 3 & 4, we have discussed about the structure-control strategy to enhance the catalytic activity and durability of nanoparticles (NPs) catalysts for oxygen reduction reaction (ORR). In this chapter, we introduced another synthetic tuning parameter-one dimensional NRs and also studied their shape effect in ORR catalysis. We synthesized a new class of 20 nm $\times$ 2 nm ternary alloy FePtM (M = Cu, Ni) nanorods (NRs) with controlled compositions. Supported on carbon support and treated with acetic acid as well as electrochemical etching, these FePtM NRs were converted into core/shell FePtM/Pt NRs. These core/shell NRs, especially FePtCu/Pt NRs, exhibited much improved ORR activity and durability. The $Fe_{10}Pt_{75}Cu_{15}$ NRs showed a mass current density of 1.034 A/mgPt at 512 mV and 0.222 A/mgPt at 557 mV (vs Ag/AgCl), much higher than the commercial Pt catalyst of 0.138A/mgPt and 0.035 A/mgPt at the corresponding potentials. Our controlled synthesis provides a general approach to core/shell NRs with enhanced catalysis for ORR or other chemical reactions.

5.1 Background and Motivation

As we claimed in Chapter 1, developing highly efficient catalyst for oxygen reduction reaction (ORR) is key to fabrication of commercially viable fuel cell devices and even metal-air batteries for future energy applications.[1-3] Recent search for advanced catalysts for ORR has led to some exciting advances in understanding the catalytic nature, allowing more rational tuning of catalytic properties via controlled syntheses. For example, when Pt is alloyed with early transition metal, such as Fe, Co, Ni, its d-band center is down-shifted and its bonding to oxygenated species is weakened, leading to the increase in catalytic activity for ORR.[3-5] More interestingly, when Pt is present as a thin shell in a core/shell structure, both its activity and durability are greatly enhanced due to the simultaneous down-shift of its d-band center and surface strain induced in the Pt shell, which is favorable for O_2 adsorption and activation.[6-8] Pt catalysis for ORR can be further activated when Pt catalysts are prepared in a controlled shape,[9-10] especially in one dimensional (1D) nanostructure,[8-9] where interactions between a crystal facet and oxygenated species as well as carbon support can be optimized to achieve high catalytic activity with increased catalyst stability. These previous studies indicate that a 1D core/shell nanostructure with Pt on shell can combine both alloy and shape effects to enhance ORR catalysis. Therefore a controlled synthesis of core/shell 1D nanostructure may provide a new approach to highly efficient Pt catalyst for ORR.
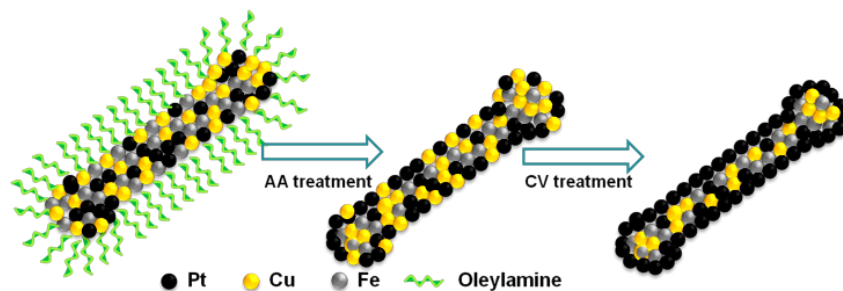
Figure 5-1. Schematic illustration of formation and activation of core/shell-type NR catalyst.

Here we report the synthesis of core/shell nanorods (NRs) to further enhance catalysis for ORR. Previously, our group prepared FePt, CoPt and FePtPd nanowires (NWs) and studied their catalysis for ORR.[11-12] We found that adding Pd to FePt NWs destabilized the catalyst without obvious activity gain. Conversely, these ternary NWs increased the activity for methanol oxidation reaction.[11] Without the presence of Pd, the FePt and CoPt NWs were more active and durable for ORR than the polyhedral NP catalysts.[12] However, upon acetic acid treatment to remove surfactant coating and to activate NW catalyst, a majority of M in MPt NWs was etched away, minimizing the M-effect on the enhancement of Pt catalysis. To fully realize the M-alloy benefits in catalysis, it is necessary to develop a 1D nanostructure with M being preserved in acid solution. With this in mind, we developed a controlled synthesis of 20 nm x 2 nm NRs of FePtM (M = Cu,　Ni) and studied their acid stability. We found that these thin FePtM NRs, especially FePtCu NRs, were much more stable in acid solution. When treated with acetic acid and etched electrochemically in 0.1 M $HClO_4$, these ternary alloy NRs were converted into

core/shell FePtM/Pt NRs with Fe and M (especially Cu) being preserved in the core NRs, as illustrated in **Figure 5-1**. These core/shell NRs combine 1-D shape and core/shell effects on catalysis and show indeed much higher activity and durability for ORR.

5.2 Results and Discussion

5.2.1 Synthesis of FePtM (M = Cu, Ni) NRs

FePtM (M = Cu, Ni) NRs were synthesized by the thermal decomposition of iron pentacarbonyl ($Fe(CO)_5$) and the reduction of metal acetylacetonates ($Pt(acac)_2$ and $Cu(acac)_2$ or $Ni(acac)_2$) (see **Experimental**).[12] The oleylamine and sodium oleate were used to control NR growth and stabilization, while the mixture of oleylamine and octadecene (v/v = 2/3) served as the solvent. In the synthesis, the composition of ternary NRs was controlled by the precursor ratios. Inductively coupled plasma-atomic emission spectroscopy (ICP-AES) analyses indicated that the Cu/Pt or Ni/Pt in the as-synthesized NRs was linearly proportional to the ratio of $Cu(acac)_2/Pt(acac)_2$ (**Table 5-1**). The $Fe_{51}Pt_{49}$ NRs were also made without the addition of $Cu(acac)_2$ and $Ni(acac)_2$ (**Figure 5-2**) and were used as a control. Transmission electron microscopy (TEM) images show that the as-synthesized FePtM (M = Cu, Ni) NRs in different compositions had the same morphology with average length in 20 ± 2 nm and diameter in 2 ± 0.2 nm (**Figure 5-3**). These FePt and FePtM (M = Cu, Ni) NRs show typical face centered cubic (*fcc*) structures, as

indicated by XRD patterns in **Figure 5-4**. **Figure 5-5** shows HRTEM image of the representative $Fe_{29}Pt_{41}Cu_{30}$ NRs, within which the adjacent lattice spacing was measured to be 0.22 nm, corresponding to the (111) interplanar distance of *fcc*-FePtCu. The lattice fringe points away from the NR growth direction by approximately 55°, indicating that the NRs grow along the [100] direction, in consistent to that observed in the growth of FePt and FePtPd NWs.[11-13]

Precursor ratio Fe:Pt:Cu	4:4:1	2:2:1	4:4:3
Composition from ICP-AES	$Fe_{42}Pt_{44}Cu_{14}$	$Fe_{38}Pt_{42}Cu_{20}$	$Fe_{29}Pt_{41}Cu_{30}$
Precursor ratio Fe:Pt:Ni	4:4:1	2:2:1	4:4:3
Composition from ICP-AES	$Fe_{43}Pt_{45}Ni_{12}$	$Fe_{35}Pt_{44}Ni_{21}$	$Fe_{31}Pt_{37}Ni_{32}$

Table 5-1. Composition control of FePtCu and FePtNi NRs by varying the precursor ratio.
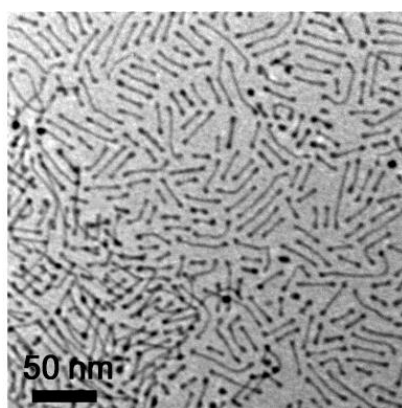
Figure 5-2. TEM image of the $Fe_{51}Pt_{49}$ NRs.
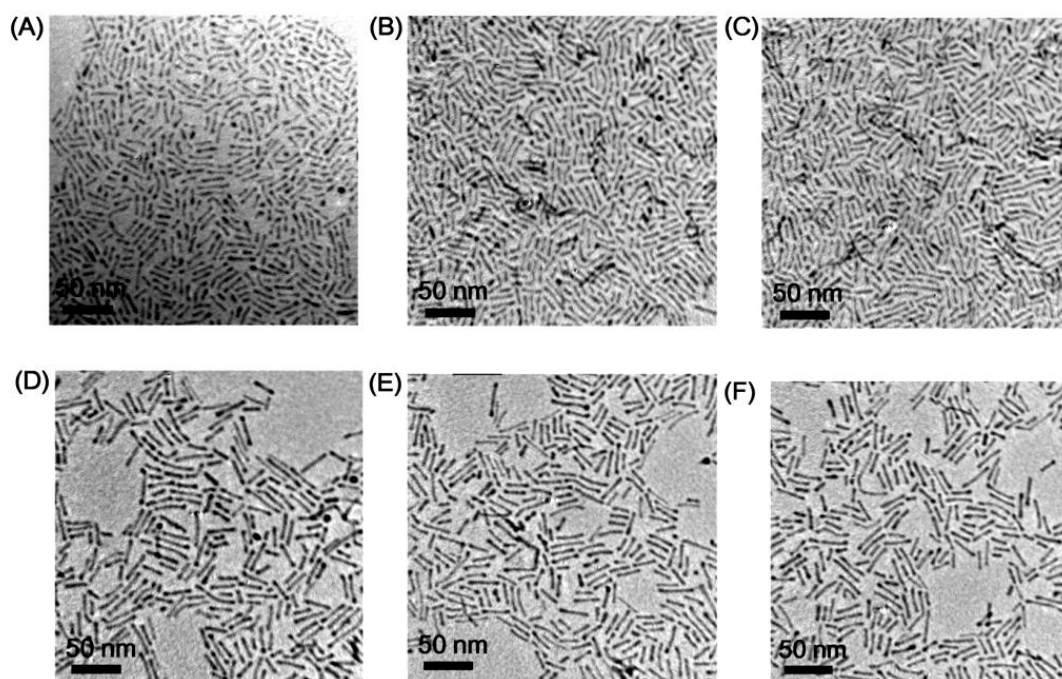
Figure 5-3. TEM images of (A) $Fe_{42}Pt_{44}Cu_{14}$, (B) $Fe_{38}Pt_{42}Cu_{20}$, (C) $Fe_{29}Pt_{41}Cu_{30}$, (D) $Fe_{43}Pt_{45}Ni_{12}$, (E) $Fe_{35}Pt_{44}Ni_{21}$, and (F) $Fe_{31}Pt_{37}Ni_{32}$ NRs.
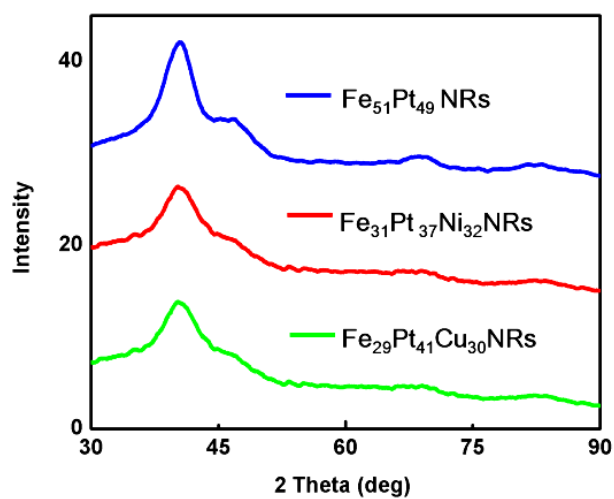
Figure 5-4. XRD patterns of $Fe_{51}Pt_{49}$, $Fe_{31}Pt_{37}Ni_{32}$, $Fe_{29}Pt_{41}Cu_{30}$ NRs.
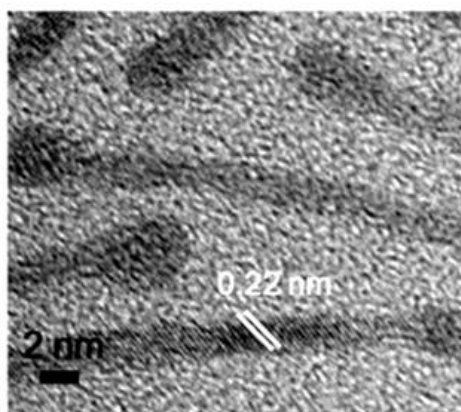
Figure 5-5. HRTEM image of $Fe_{29}Pt_{41}Cu_{30}$ NRs.

Under the current synthetic condition, the 1D FePt NRs were first formed before Cu- or Ni-precursor was added at 160 °C (**Figure 5-6**). It looks that the FePt NRs served as the template and Cu/Ni was incorporated into the NR structure via intermetallic diffusion.[14] The presence of $Fe(CO)_5$ and the formation of FePt was the key to the formation of ternary NRs. Without $Fe(CO)_5$, only irregular CuPt (or NiPt) NPs were produced. If the FePtM NRs were prepared when Fe- and Pt-precursor were in equal amount at 0.25 mmol each, the addition of Cu/Ni-precursors had no effect on the FePt formation as the Fe/Pt ratios in FePt and FePtM NRs were nearly the same. When the precursor Fe/Pt ratio was increased to 2 (0.5 mmol/0.25 mmol), the Fe/Pt ratio remained to be 1 (**Figure 5-7**). Here, Cu- or Ni-salts were mainly reduced by $Fe(CO)_5$ when the excess of $Fe(CO)_5$ was present. But with both $Fe(CO)_5$ and $Pt(acac)_2$ at 0.25 mmol, Cu- or Ni-salts tended to be reduced by oleylamine. The subsequent high-temperature (240 °C) aging promoted the atomic diffusion, producing ternary alloy NRs. We should note that although the excess of $Fe(CO)_5$

had no obvious effect on the final NR composition, it did help to control the length of

NRs. For example, a precursor ratio of Fe:Pt = 2:1 led to the formation of 60 nm x 2

nm NWs (**Figure 5-7**).
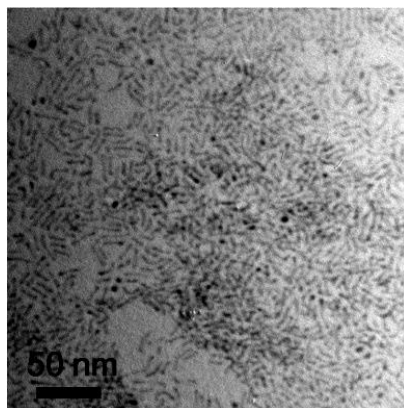
Figure 5-6. TEM image of the sample separated from the 160 ℃ solution in the synthesis of FePtCu NRs before $Cu(acac)_2$ was added.
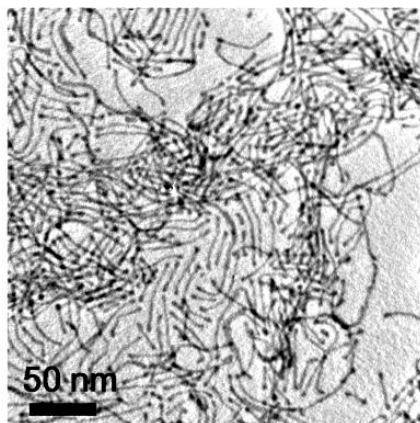
Figure 5-7. TEM image of the $Fe_{38}Pt_{40}Cu_{22}$ NWs.

5.2.2 Formation of FePtM/Pt Core/Shell (M = Cu, Ni) NRs

The 20 x 2 nm NRs were loaded on Ketjen carbon support (C) as reported.[15-16] The C-NRs were washed with acetic acid (AA) at 70 °C to remove oleate/oleylamine coating.[17] ICP-AES analyses showed that this acid treatment led to partial loss of Fe and Ni in all NRs, but negligible loss of Cu in FePtCu NRs (**Table 5-2**). After the washing step, the C-NRs (or commercial C-Pt NPs, 20% mass loading with Pt particle diameter of 2.5-3.5 nm) were suspended in deionized water + isopropanol + 5% Nafion (v/v/v = 4/1/0.05) forming a suspension of 2 mg catalyst/mL. 20 μL of the suspension was deposited on the glassy carbon (GC) surface of a rotating disk electrode (RDE) and dried at ambient environment. The C-NRs deposited on GC-RDE were subject to further CV scanning from -0.2 V to 1.0 V in N_2-saturated 0.1 M $HClO_4$ for "Cu dealloying".[18] **Figure 5-8A** is the CV curves of the 10th and 60th potential cycles. We can see that the CV of the 60th cycle shows a sharper hydrogen underpotential formation/stripping peak in the range of -0.2 to 0.15 V and a positive shift of the reduction peak related to Pt-oxygenated species, suggesting the Cu depletion of the near surface region and the formation of a Pt-enrichment shell.[19-21] After these CV scans, the NR composition was changed from $Fe_{12}Pt_{54}Cu_{34}$ to $Fe_{10}Pt_{75}Cu_{15}$. The core/shell FePtCu/Pt NRs were characterized by atomically resolved aberration-corrected scanning transmission electron microscopy (STEM) and STEM-electron energy loss spectroscopy (STEM-EELS). **Figure 5-8B** show the high-angle annular dark field (HAADF) image of the NRs after 60 CV cyclings

(Inset) and the related EELS line scan, confirming the formation of a thin Pt-shell after surface dealloying.

Before acetic acid wash	$Fe_{42}Pt_{44}Cu_{14}$	$Fe_{38}Pt_{42}Cu_{20}$	$Fe_{29}Pt_{41}Cu_{30}$
After acetic acid wash	$Fe_{25}Pt_{58}Cu_{17}$	$Fe_{21}Pt_{54}Cu_{25}$	$Fe_{12}Pt_{54}Cu_{34}$
Before acetic acid wash	$Fe_{43}Pt_{45}Ni_{12}$	$Fe_{35}Pt_{44}Ni_{21}$	$Fe_{31}Pt_{37}Ni_{32}$
After acetic acid wash	$Fe_{24}Pt_{69}Ni_{7}$	$Fe_{20}Pt_{67}Ni_{13}$	$Fe_{20}Pt_{64}Ni_{16}$

Table 5-2. Composition change of FePtCu and FePtNi NRs before and after acetic acid wash.
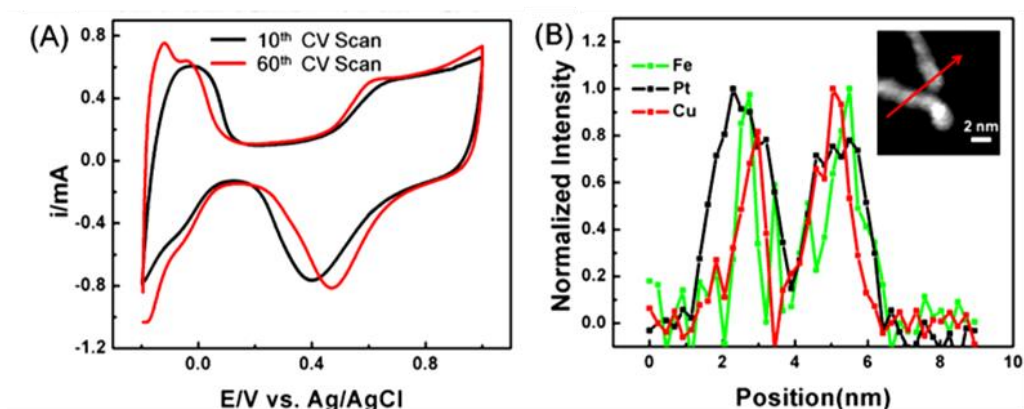
Figure 5-8. (A) CVs at the beginning and at the end of the electrochemical etching process. The potentials were from -0.2 V to 1.0 V at a scan rate of 100 mV/s in N_2-saturated 0.1 M $HClO_4$. **(B)** STEM-HAADF image (**Inset**) and STEM-EELS line scan of the representative $Fe_{10}Pt_{75}Cu_{15}$ NRs obtained after the CV-cycling of $Fe_{29}Pt_{41}Cu_{30}$ NRs.

5.2.3 ORR Catalysis of FePtM/Pt Core/Shell (M = Cu, Ni) NRs

Figure 5-9A shows the CVs of the core/shell NRs (from $Fe_{29}Pt_{41}Cu_{30}$ NRs) and C-Pt in N_2-saturated 0.1 M $HClO_4$. The peaks in the range of -0.2 to 0.15 V are from the common hydrogen underpotential formation/stripping and are used to estimate the electrochemically active surface area (ECASA) of the catalyst.[22] The metal oxidation/reduction peaks appear in the range of 0.4-0.9 V. The composition-dependent ORR activity of the FePtCu NRs was studied. **Figure 5-9B** shows the ORR polarization curves of the core/shell NRs of FePtCu NRs and commercial Pt NPs in O_2-saturated 0.1 M $HClO_4$. The ORR polarization curves depict the diffusion-limiting current region ranging from -0.05 to 0.4 V and the mixed kinetic$-$diffusion control region between $\sim$0.4 and $\sim$0.7 V. With the increase in Cu, the half-wave potential of the FePtCu NRs shifts positively, indicating that the NRs with the initial composition of $Fe_{29}Pt_{41}Cu_{30}$ (0.557 V) have a better catalytic activity towards ORR than $Fe_{38}Pt_{42}Cu_{20}$ (0.551 V), $Fe_{42}Pt_{44}Cu_{14}$ (0.537 V) and $Fe_{51}Pt_{49}$ NRs (0.520 V) at the same NR loading by weight. The ORR activity of the $Fe_{10}Pt_{75}Cu_{15}$ NRs was compared with the C-Pt NPs (**Figure 5-9C**). The ORR half potential from the $Fe_{10}Pt_{75}Cu_{15}$ NRs is 45 mV more positive than that of the C-Pt catalyst (0.512 V). The $Fe_{10}Pt_{75}Cu_{15}$ NRs have a mass activity (MA) of 1.034 A/mgPt and a specific activity (SA) of 1.369 mA/cm^2 at 512 mV (*vs* Ag/AgCl), which is 7 and 5 times higher than that of the commercial C-Pt (0.138A/mgPt and 0.271 mA/cm^2). At 557 mV, the $Fe_{10}Pt_{75}Cu_{15}$ NRs have an MA of 0.222 A/mgPt and a SA

of 0.299 mA/cm^2, while the commercial C-Pt shows only 0.035 A/mgPt and 0.068

mA/cm^2.
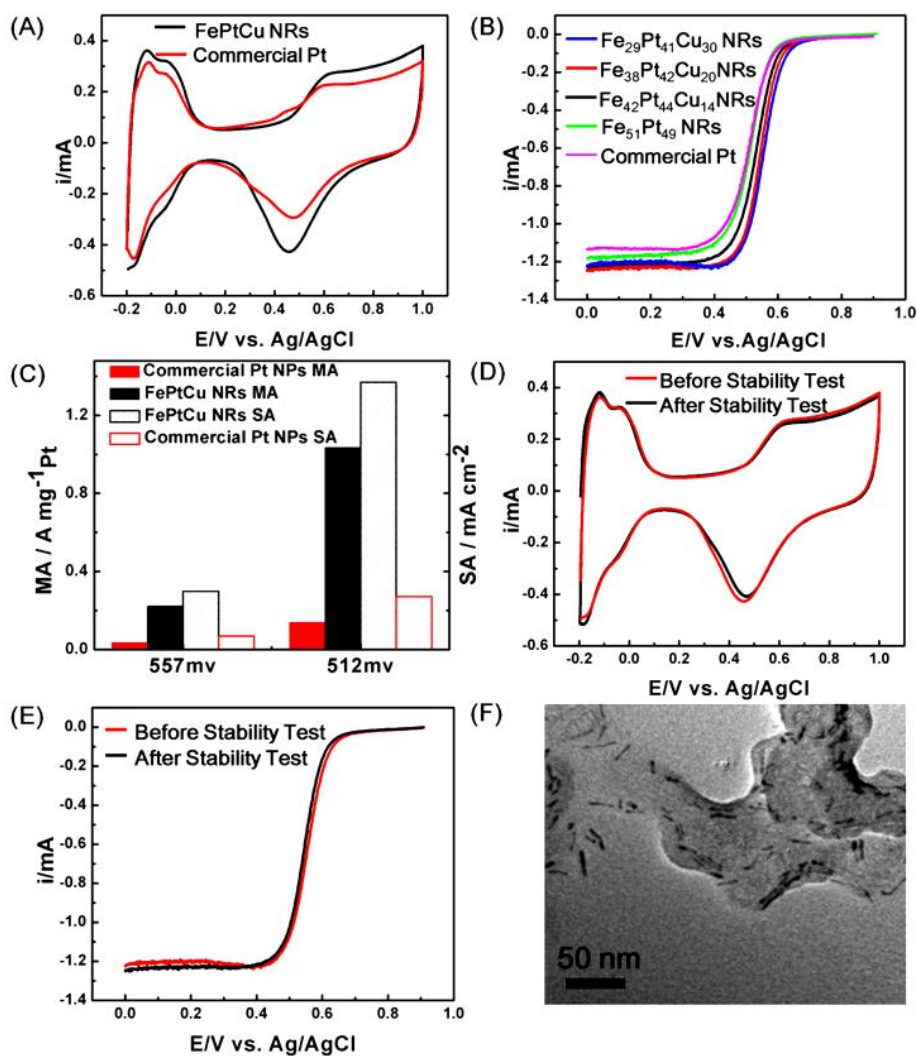
Figure 5-9. (**A**) CVs of the C-Fe$_{10}$Pt$_{75}$Cu$_{15}$ NRs and C-Pt NPs in N$_2$-saturated 0.1 M HClO$_4$ at a scan rate of 50 mV/s. (**B**) Polarization curves of the FePtCu NRs with different initial compositions and commercial Pt NPs in O$_2$-saturated 0.1 M HClO$_4$ at 295 K. (**C**) ORR mass activity (MA) and specific activity (SA) of Fe$_{10}$Pt$_{75}$Cu$_{15}$ NRs and commercial Pt NPs. (**D**) CVs of Fe$_{10}$Pt$_{75}$Cu$_{15}$ NRs in N$_2$-saturated 0.1 M HClO$_4$ before and after 5000 potential cycles between 0.4-0.8 V in O$_2$-saturated 0.1 M HClO$_4$. (**E**) Polarization curves of the Fe$_{10}$Pt$_{75}$Cu$_{15}$ NRs in O$_2$-saturated 0.1 M HClO$_4$ at 295 K before and after 5000 potential cycles between 0.4-0.8 V in O$_2$-saturated 0.1 M HClO$_4$. (**F**) TEM image of the Fe$_{10}$Pt$_{75}$Cu$_{15}$ NRs on carbon support after 5000 cycles of stability test.

Durability of the core/shell NR catalyst was tested by cycling potentials between 0.4-0.8 V (vs. Ag/AgCl) at a sweep rate of 100 mV/s in O_2-saturated 0.1 M $HClO_4$. The CVs (**Figure 5-9D**) and polarization curves (**Figure 5-9E**) of the $Fe_{10}Pt_{75}Cu_{15}$ NRs before and after 5000 potential cycles nearly overlap. Correspondingly, the core/shell NRs show no obvious morphology and composition change before and after the durability test, as demonstrated by their TEM image (**Figure 5-9F)** and their slight composition drop in Fe/Cu from $Fe_{10}Pt_{75}Cu_{15}$ to $Fe_8Pt_{78}Cu_{14}$. These suggest that the FePtCu/Pt core/shell NRs are highly stable in the current ORR condition.

The FePtNi NRs also displayed composition-dependent ORR activities (**Figure 5-10**). More FeNi present in FePtNi NRs led to higher activity. However, after the acetic acid treatment, a substantial amount of Ni was lost (**Table 5-2**). Therefore, FePtNi NRs were less stable in acid and less active for catalyzing ORR than FePtCu NRs.
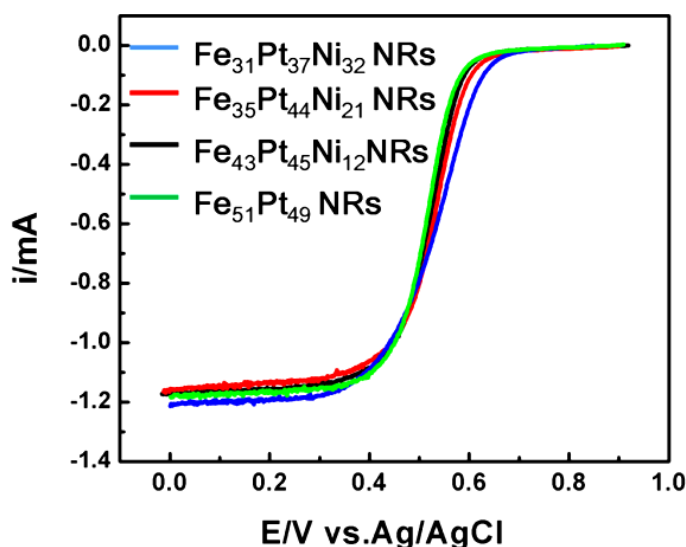
Figure 5-10. Polarization curves of the FePtNi and FePt NRs with different initial compositions in O_2-saturated 0.1 M $HClO_4$ at 295 K.

5.3 Summary

In summary, we have developed a facile solution-phase process to synthesize ternary alloy FePtM (M = Cu, Ni) NRs with their dimension controlled to be 20 x 2 nm and their compositions tuned by the precursor ratios. These NRs are more stable in acid than their binary counterparts. When treated with acetic acid and electrochemical etching in 0.1 M $HClO_4$, these ternary alloy NRs are converted into core/shell structured FePtM/Pt NRs. These core/shell NRs, especially FePtCu/Pt NRs, are a new class of ORR catalyst superior to their binary counterparts and the commercial Pt catalyst. The core/shell NRs obtained from the $Fe_{29}Pt_{41}Cu_{30}$ alloy NRs show much enhanced durability and have the mass and specific activities that are 7- and 5-fold higher than the commercial Pt NP catalyst. Our controlled synthesis of

core/shell 1D nanostructure provides a new approach to highly efficient Pt catalyst for ORR. The same structure may also offer an alternative catalyst model to study electronic and strain effect for tuning NP catalysis for other chemical reactions.

5.4 Experimental

Chemicals and Materials. Sodium oleate, oleylamine (OAm, >70%), oleic acid (OA), 1-octadecene (ODE), $Pt(acac)_2$ (acac = aceylacetonate), $Cu(acac)_2$, $Ni(acac)_2$, iron pentacarbonyl ($Fe(CO)_5$), hexane, isopropanol, ethanol, acetic acid (99%) and Nafion (5%) were all purchased from Sigma Aldrich. C-Pt (20% mass loading with a diameter of 2.5-3.5 nm) catalyst was obtained from Fuel Cell Store.

Instrumentation. TEM images were obtained from a Philips CM 20 operating at 200 kV. High-resolution TEM (HRTEM) images were obtained from a JEOL 2010 with an accerating votalage of 200 kV. TEM and HRTEM samples were prepared by depositing a single drop of diluted nanorod (NR) dispersion in hexane on amorphous carbon coated copper grids. The inductively coupled plasma-atomic emission spectroscopy (ICP-AES) measurements were carried on a JY2000 Ultrace ICP Atomic Emission Spectrometer equipped with a JY AS 421 autosampler and 2400g/mm holographic grating. Electrochemical measurements were performed on a Fuel Cell Electrocatalyst RDE bundle from PINE Instrument Company with a model AFCBP1 with a three-electrode system consisting of a glassy carbon (GC) working

electrode (5-mm in diameter), an Ag/AgCl reference electrode (10% KNO_3), and a platinum wire counter electrode.

Synthesis of FePtCu and FePtNi Nanorods (NRs). A mixture solution of sodium oleate (0.3g) and ODE (12 mL) in a four-necked flask was heated to 200 ℃ under nitrogen flow and magnetic stirring to make sodium oleate dissolved thoroughly. Then the solution was cooled down to room temperature and a mixture of $Pt(acac)_2$ (98 mg) and OAm (8 mL) was added into the solution and heated to 120 ℃. Under the blanket of nitrogen, $Fe(CO)_5$ (0.03 mL) was added into the solution that was then further heated to 160 ℃. At this temperature, a mixture of $Cu(acac)_2$ (32 mg) and OAm (3 mL) was added into the solution followed by heating to 240 ℃ and keeping at this temperature for 1 h. After cooled down to room temperature, the FePtCu NRs were collected and washed by addition of isopropanol (20 mL) and subsequent centrifugation at 8500 rpm for 8 min. The product was redispersed into hexane and precipitated out by addition of ethanol and centrifugation to remove all residual impurities. Final product was FePtCu NRs and was dispersed in hexane for further use. Under the identical condition, by changing $Cu(acac)_2$ to $Ni(acac)_2$, FePtNi NRs were prepared. Different composition was obtained by varying the amount of $Cu(acac)_2$ or $Ni(acac)_2$ at a fixed ratio between $Fe(CO)_5$ and $Pt(acac)_2$, as summerized in **Table S1**.

FePtCu NWs. The synthetic procedure of FePtCu NWs was samilar to that of NRs except 0.07ml of Fe(CO)$_5$ was added at 120 ℃.

FePt NRs. Similar to the synthesis of FePtCu NRs, FePt NRs were obtained by direct injection of Fe(CO)$_5$ and by heating the mixture to 240 ℃ for 60 min at the heating rate of about 4-5 ℃/min without the presence of Cu(acac)$_2$.

Catalyst Preparation. The as-synthesized NRs and Ketjen-300 J carbon at the weight ratio of 4:6 were mixed in 20 mL mixture of hexane and acetone (V/V=1/1) and sonicated for 1 h to deposit NRs on carbon. The product was separated from teh solvent by centrifugation and was suspended in 30 ml acetic acid at 70 ℃ for overnight to remove the surfactant. The resultant solid product was separated from the acid by centrifugation and washed with ethanol and deionized water. The product was then redispersed in a mixture of deionized water, isopropanol and Nafion (V/V/V = 4/1/0.05). 20 μL catalyst ink was deposited on the working electrode (glassy carbon rotating disk electrode, GC-RDE) that was polished prior to catalyst deposition by 0.1 μm and 0.05 μm alumina powder and rinsed by sonication in ethanol and in deionized water. The catalyst was dried at ambient condition.

Electrochemical Measurements. Cyclic voltammograms (CVs) were obtained by scaning between -0.2 V-1.0 V *vs* Ag/AgCl at a scan rate of 50 mV/s in N$_2$-saturated

0.1M $HClO_4$. ORR polarization curves were obtained by scaning the potentials from

1.0 to -0.2 V *vs* Ag/AgCl at a scan rate of 10 mV/s in O_2-saturated 0.1 M $HClO_4$ with

the GC-RDE rotating at 1600 rpm.

Reference

1. J. Zhang, PEM Fuel Cell Electrocatalysts and Catalysts Layers Fundamentals and Application. Springer **2008**.

2. C. Wang, H. Daimon, T. Onodera, T. Koda, S. Sun, *Angew. Chem. Int. Ed.* **2008**, *47*, 3588-3591.

3. H. Lee, S. E. Habas, S. Kweskin, D. Butcher, G. A. Somorjai, P. Yang, *Angew. Chem., Int. Ed.* **2006**, *45*, 7824-7828.

4. (a) V. A. Sethuraman, J. W. Weidner, A. T. Haug, S. Motupally, L.V. Protsailo, *J. Electrochem. Soc.* **2008**, *155*, B50-B57. (b) R. R. Adz, J. X. Wang, *J. Phys. Chem. B.***1998**, *102*, 8988-8993.(c) B. N. Wanjala, B. Fang, J. Luo, Y. Chen, J. Yin, M. H. Engelhard, R. Loukrakpam, C. J. Zhong, *J. Am. Chem. Soc.* **2011**, *133*, 12714-12727.

5. V. R. Stamenkovic, B. S. Mun, M. Arenz, K. J. J. Mayrhofer, C. A. Lucas, G. Wang, P. N. Ross, N. M. Markovic, *Nat. Mater.* **2007**, *6*, 241-247.

6. V. Mazumder, M. Chi, K. L. More, S. Sun, *J. Am. Chem. Soc.* **2010**, *5*, 7848-7849.

7. C. Wang, D. Vliet, K. More, N. Zaluzec, S. Peng, S. Sun, H. Daimon, G. Wang, J. Greeley, J. Pearson, A. Paulikas, G. Karapetrov, D. Strmcnik, N. M. Markovic, V. R. Stamenkovic, *Nano Lett.* **2011**, *11*, 919-926.

8. (a) C. Cui, S. Yu, *Acc. Chem. Res.* **2013,** 46, DOI: 10. 1021/ar300254b. (b)C. Cui, H. Li, J. Yu, M. Gao, S. Yu, *Angew. Chem. Int. Ed.* **2010**, 49, 9149-9152. (c) H.

Li, C. Cui, S. Zhao, H. Yao, M. Gao, F. Fan, S. Yu, *Adv. Energy. Mater.* **2012**, 2, 1182-1187. (d) C. Koenigsmann, A. C. Santulli, K. Gong, M. B. Vukmirovic, W. Zhou, E. Sutter, S. S. Wong, *J. Am. Chem. Soc*. **2011**, *133*, 9783-9795.

9. H. Zhou, W. Zhou, R. R. Adzic, S. S. Wong, *J. Phys. Chem. C.* **2009**, *113*, 5460-5466.

10. S. Sun, G. Zhang, D. Geng, Y. Chen, R. Li, M. Cai, X. Sun, *Angew. Chem. Int. Ed.* **2011**, *50*, 422-426.

11. S. Guo, S. Zhang, X. Sun, S. Sun, *J. Am. Chem. Soc.* **2011**, *133*, 15354-15357.

12. S. Guo, D. Li, H. Zhu, S. Zhang, N. M. Markovic, V. R. Stamenkovic, *Angew. Chem. Int. Ed.* **2013**, *52*, 3465-3468.

13. C. Wang, Y. Hou, J. Kim, S. Sun. *Angew. Chem. Int. Ed.* **2007**, *46*, 6333-6335..

14. S. Liu, C. Zhang, L. Yuan, J. Bao, W. Tu, M. Han, Z. Dai, *Part. Part. Syst. Charact.* **2013**, DOI: 10. 1002/ppsc.201200150.

15. V. Mazumder, S. Sun, *J. Am. Chem. Soc*. **2009**, *131*, 4588-4589.

16. S. Zhang, S. Guo, H. Zhu, D. Su, S. Sun, *J. Am. Chem. Soc*. **2012**, *134*, 5060-5063.

17. S. Guo, S. Sun, *J. Am. Chem. Soc.* **2012**, *134*, 2492-2495.

18. S. Koh, T. Anniyev, J. Greeley, K. More, C. Yu, Z. Liu, P. Strasser, *Nature Chem.* **2010**, *2*, 458-460.

19. C. Wang, M. Chi, D. Li, D. Strmcnik, G. Wang, V. Komanicky, N. M. Markovic, V. R. Stamenkovic, *J. Am. Chem. Soc.* **2011**, *133*, 14396-14403.

20. V. R. Stamenkovic, B. Fowler, B. S. Mun, G. Wang, P. N. Ross, C. A. Lucas, N. M. Markovic, *Science* **2007**, *315*, 493-497.

21. F. Maillard, L. Dubau, J. Durst, M. Chatenet, J. Andre, E. Rossinot, *Electrochem. Commun.* **2010**, *12*, 1161-1164.

22. J. Snyder, T. Fujita, M. W. Chen, J. Erlebacher, *Nat. Mater.* **2010**, *9*, 904−907.

Chapter 6

Co/CoO Nanoparticles Assembled on Graphene for Electrochemical Reduction of Oxygen

In Chapter 3-5, we have investigated the Pt-based nanoparticles (NPs) catalysts for oxygen reduction reaction (ORR) in acidic solution. These intermetallic FePt NPs, FePtCu NPs, FePtCu/FePtNi nanorods (NRs) have shown ever increased activity and durability towards ORR. But as an ultimate goal, efficient and durable non-Pt catalysts for ORR have attracted numerous efforts recently. In this chapter, we introduced a solution-phase self-assembly approach leading to Co/CoO core/shell nanoparticles deposited on graphene (G–Co/CoO NPs), which served as a new kinds of non-Pt NPs catalysts for ORR in alkaline condition. Their catalytic activity for the ORR in O_2-saturated KOH solution depends on the thickness of the CoO shell. The optimized G–Co/CoO NPs have a comparative activity and better stability than the commercial Pt NP catalyst supported on carbon (C–Pt).

6.1 Background and Motivation

Platinum (Pt) has been the best metal found to catalyze the oxygen reduction reaction (ORR) which occurs in in polymer membrane electrolyte fuel cells (PEMFCs). [1] However, the use of Pt is costly, and in corrosive PEMFC reaction conditions, Pt-based catalysts tend to have very limited durability. [2-6] In searching for more robust and practical catalysts with comparative or even better catalytic performance than Pt, early transition metals supported on graphene (G) have attracted much attention. G is a single-layer, two-dimensional honeycomb type carbon sheet that has large surface area, excellent conductivity, and good chemical stability. [7-9] It has been explored extensively either as nonmetal catalyst through molecular engineering [10-14] or as a unique support for metal catalysts. [15-18] Studies on G–metal interactions reveal that depending on the G–metal spacing and the Fermi level difference between G and the metal, there often exist a charge transfer across the G–metal interface. [19] Such a charge transfer may be the main reason why certain nanoparticles (NPs) supported on a G surface show enhanced catalytic activities, as demonstrated in the catalysts of G–Co_3O_4, [15] G–Fe_3O_4, [16] G–Co_xS_{1-x}, [17] and G–$MnCo_2O_4$ [18] for the ORR in alkaline [15, 16, 18] or acid [17] media. In these G–metal oxide catalyst systems, metal oxide NPs were deposited directly onto G surfaces through in situ chemical depositions. [15-18] Despite the fact that the depositions led to a tight G–NP contact, NPs prepared from these methods lacked the desired size and morphology control, thereby making it difficult to tune the G–NP interaction for

better catalyst performance. Recently, our group demonstrated a direct self-assembly method to deposit preformed monodisperse FePt NPs on a G surface, [19] and G–FePt showed much enhanced catalysis for the ORR in $HClO_4$ solution, thus indicating the G–NP interaction can indeed be tuned to enhance NP catalysis.

Herein we report that monodisperse Co/CoO NPs can be pre-synthesized and deposited on a G surface through the solution-phase self-assembly method, and the resulting G–Co/CoO is a high-performance electrocatalyst for the ORR in KOH (0.1 m) solution. We demonstrate that their high catalytic performance originates not only from the G–Co/CoO interaction, but also from the dimension tuning of Co and CoO. The optimum G–Co/CoO NP catalyst with an 8 nm Co core and a 1 nm CoO shell is even better than the commercial Pt NP catalyst supported on carbon (C–Pt) concerning the ORR current density near the diffusion-limit current region, and this G–Co/CoO NP catalyst is more stable than the C–Pt catalyst.

6.2 Results and Discussion

6.2.1 Synthesis of G-Co/CoO assembly

G was produced by heating graphene oxide (GO) in dimethylformamide (DMF) at 150 ℃ for six hours (see **Experimental**). [19] Co NPs were synthesized through thermal decomposition of $[Co_2(CO)_8]$ in 1,2,3,4-tetrahydronaphthalene solution in the presence of oleic acid and dioctylamine (DOA, see **Experimental**). [20] The Co-based NPs and G–Co/CoO NPs were characterized by transmission electron microscopy

(TEM). **Figure 6-1A** shows the typical TEM images of the as-prepared Co NPs. They are monodisperse 10 nm NPs with a narrow size distribution at 0.7 nm. When exposed to air at ambient condition, the top surface layers of Co were oxidized, thereby forming Co/CoO core/shell NPs. TEM analysis revealed that this CoO shell reached a thickness of approximately 1 nm (**Figure 6-1B** & **6-2A**) and the thickness did not increase in nine days of continuous air exposure (**Figure 6-2B**), thus indicating that the CoO shell was able to protect Co from further oxidization in air at room temperature. However, Co in the Co/CoO NPs could be further oxidized when the NPs were heated at 70 ℃ in air. TEM images of the Co/CoO NPs heated at 70 ℃ for 17 and 96 h are shown in **Figure 6-1C&D**. After heating for 17 h in air, the CoO layer grew to about 3 nm, while heating for 96 h led to higher-degree oxidation of Co, thereby giving a NP mixture of Co/CoO and hollow CoO NPs. When Co NPs were oxidized by an excess of trimethylamine N-oxide (Me$_3$NO) at 230 ℃, hollow CoO NPs were obtained (**Figure 6-3**). Here the hollow CoO NPs are formed through the nanoscale Kirkendall effect, which causes faster Co diffusion outwards than oxygen diffusion inwards. [21, 22] All Co-based NPs could be assembled onto G by simply mixing the hexane dispersion of the NPs with a DMF solution of G under sonication (see **Experimental**). **Figure 6-1E** shows the typical TEM image of the Co/CoO NPs assembled on G. Similarly, the Co/CoO NPs were also deposited on Ketjen carbon (C) (C–Co/CoO). These C–Co/CoO NPs were used as a control to compare with G–Co/CoO NPs in the ORR studies.
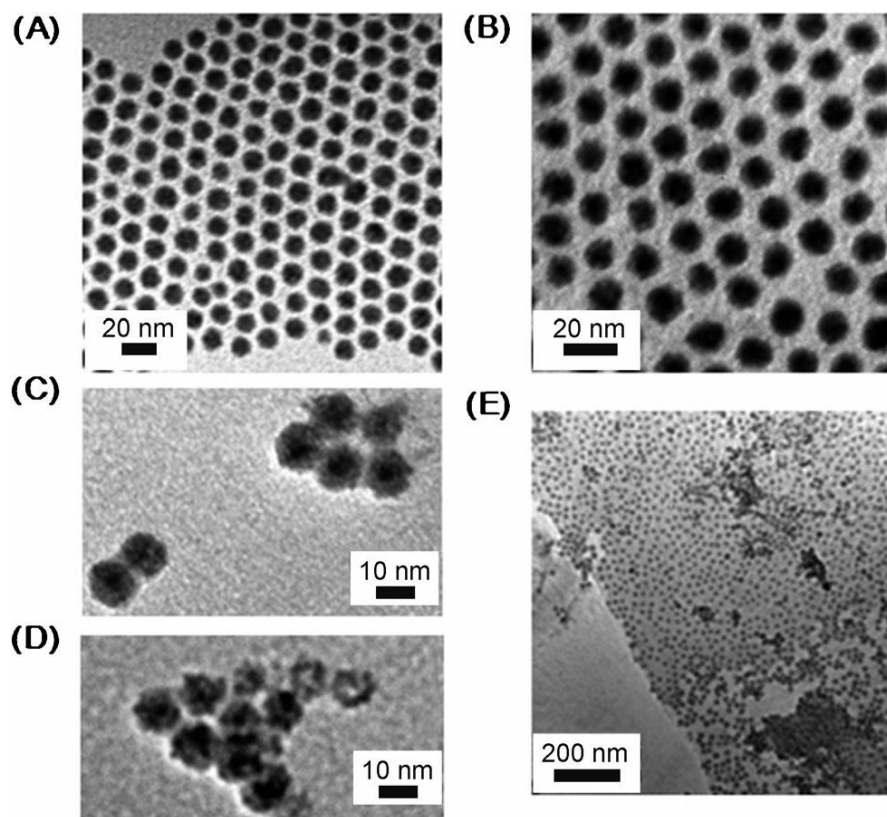
Figure 6-1. TEM images of Co NPs (A), Co/CoO core/shell NPs (B), Co/CoO NPs treated for 17 h (C) and 96 h (D) in air, and the Co/CoO core/shell NPs deposited on G surface (G–Co/CoO, E).
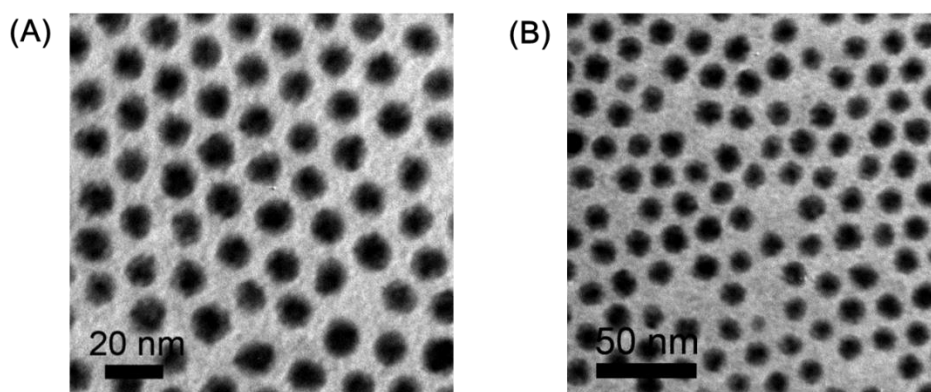
Figure 6-2. TEM image of the Co/CoO core/shell NPs stored under air for 5 days (A) and 9 days (B).
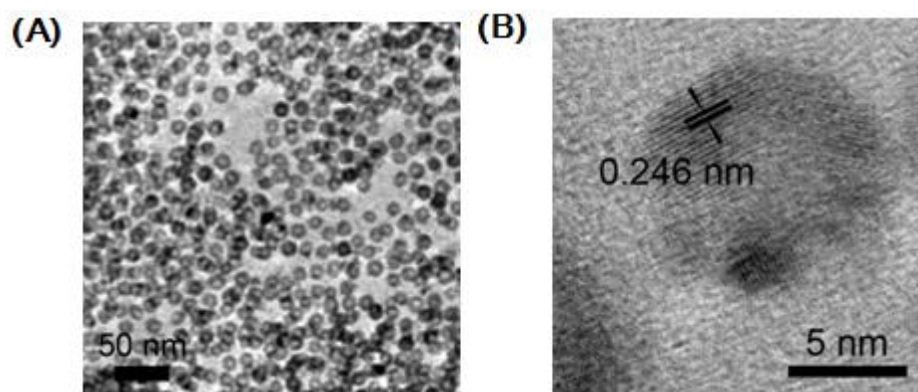
Figure 6-3. (A) TEM and **(B)** HRTEM images of the hollow CoO NPs. The spacing of the adjacent fringes is 0.246 nm, corresponding to the {111} interplanar distance of face centered cubic (*fcc*) CoO.

X-ray diffraction (XRD) analyses indicate that the as-synthesized Co NPs have a multi-twinned *fcc* structure with the (111) peak appearing at 44.3 °(**Figure 6-4**). This structure is similar to what has been reported on Co NPs obtained from thermal decomposition of [$Co_2(CO)_8$]. [20] After Co NPs were transferred into hollow CoO NPs, new diffraction peaks at 36.7, 42.7, and 62.1 °, which belong to (111), (200), and (220) diffractions of the *fcc*-CoO, were observed (**Figure 6-4**). The Co/CoO NPs show typical Co and CoO dimension-dependent magnetization behavior, as shown in the room-temperature hysteresis loops of a series of Co/CoO NPs measured by vibrating sample magnetometer (VSM; **Figure 6-5A**). The as-synthesized Co NPs show a superparamagnetic hysteresis loop with a saturation moment of 70.4 emu/g $_{NPs}$ (**Figure 6-5**). When Co NPs were exposed to air for five days, forming 8 nm/1 nm Co/CoO NPs, their moment was reduced to 40.4 emu/g $_{NPs}$ (**Figure 6-5B**). Once further heated at 70 °C in air for 17 h and 96 h, the saturation moment of the resultant

110

Co/CoO NPs was reduced to 24.2 and 16.2 emu/g $_{NPs}$ (**Figure 6-5C, D**). When the Co NPs were completely oxidized, the hollow CoO NPs were paramagnetic (**Figure 6-5E**). Clearly, the moment reduction and magnetic property change was caused by the higher degree of Co oxidation in the Co/CoO structure.
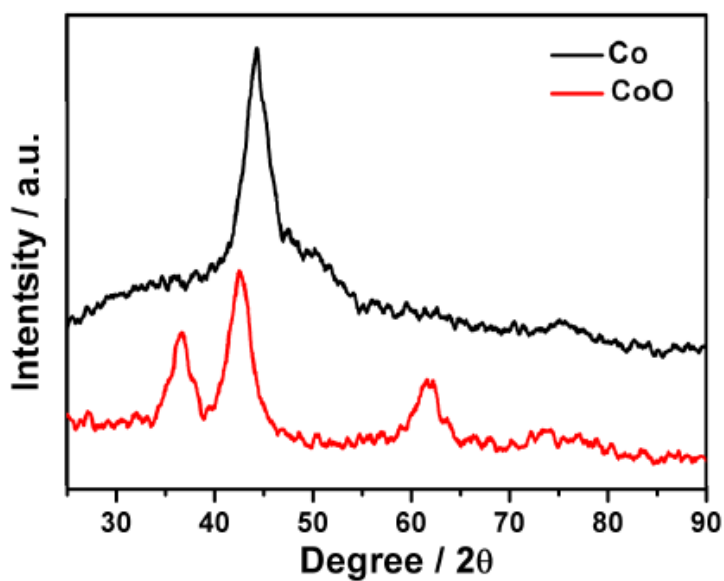
Figure 6-4. XRD patterns of the Co NPs and hollow CoO NPs. Note that the thin CoO coating on the Co NPs cannot be detected under the current XRD analysis condition.
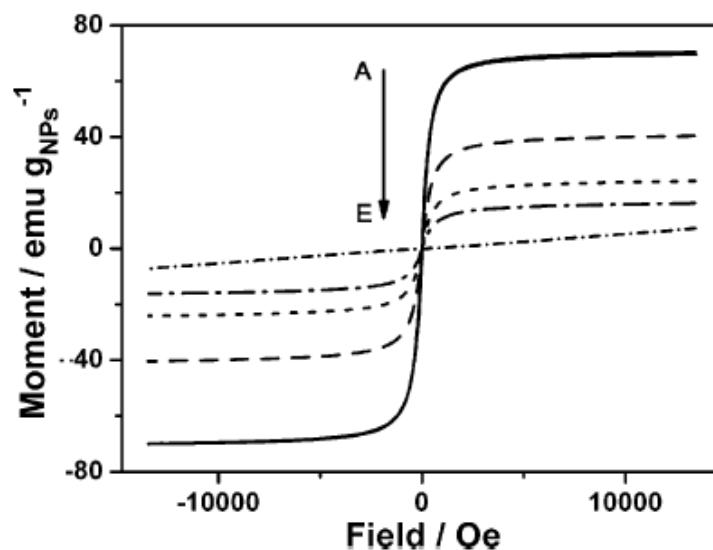
Figure 6-5. Room-temperature hysteresis loops measured by VSM of Co NPs (A), Co/CoO core/shell NPs (B), Co/CoO core/shell NPs heated at 70 ℃ in air for 17 h (C) and 96 h (D), and hollow CoO NPs (E, ×5 in moment).

6.2.2 Electrocatalysis for ORR of G-Co/CoO Assembly

The as-synthesized G–Co/CoO NPs and C–Co/CoO NPs were treated with butylamine (see **Experimental**) to remove the original long-chain surfactant. [23] This room temperature treatment was an important step to produce active Co/CoO catalysts. **Figure 6-6** shows the typical ORR polarization curves of the C–Co/CoO NPs from different treatments. After washed with butylamine, the C–Co/CoO NPs exhibited a more positive half-wave potential for the ORR than those washed with ethanol under the same condition. Furthermore, energy dispersive X-ray (EDX) analysis on the Co/CoO NPs showed the reduced C/Co ratio after the butylamine treatment (**Figure 6-7**). These results indicate that washing with butylamine was efficient to remove oleate/DOA. **Figure 6-8A** shows the typical cyclic

voltammograms (CVs) of oxygen reduction on the G-, C–Co/CoO-, and G–Co/CoO-modified glassy carbon (GC) electrodes in O_2-saturated KOH (0.1 M) solution with each catalyst having a mass loading of 20 mg. On the G-modified GC electrode, only a weak peak is seen at -0.360 V (vs. Ag/AgCl; **Figure 6-8A-i**). When C–Co/CoO is present on the electrode, the peak becomes stronger and appears at -0.276 V (**Figure 6-8Aii**). Compared to G and the C–Co/CoO NPs, the G–Co/CoO NPs show a much stronger cathodic peak with the peak potential at -0.198 V (**Figure 6-8A-iii**). These indicate that O_2 can be reduced much more easily on G–Co/CoO NPs than on G and C–Co/CoO NPs.
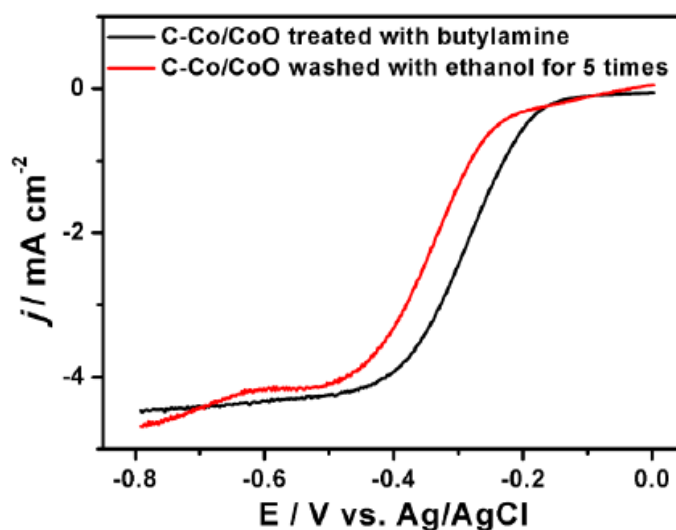
Figure 6-6. ORR polarization curves of the C-Co/CoO NPs
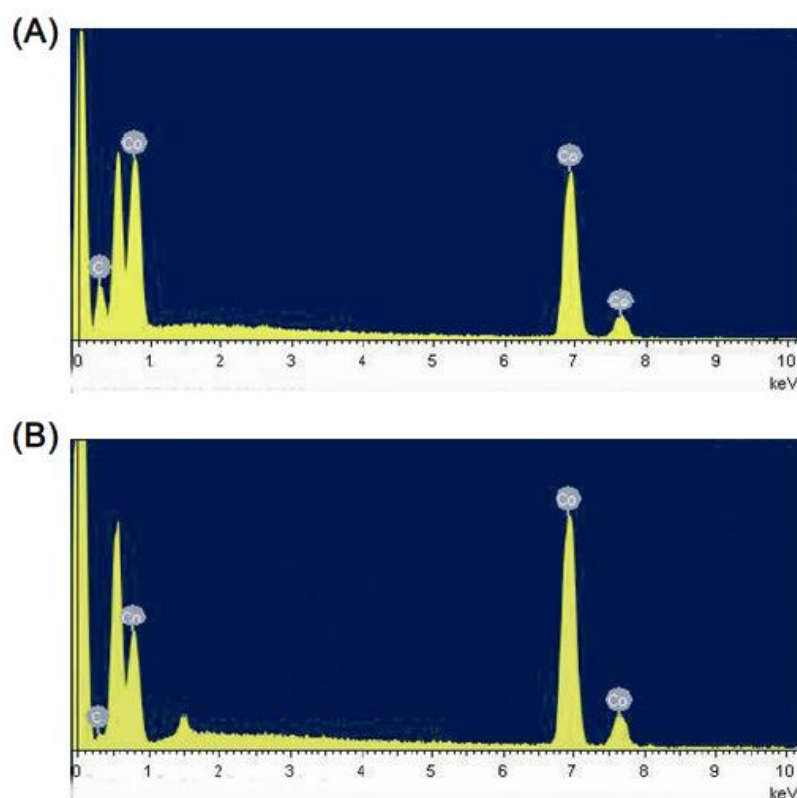
Figure 6-7. EDX spectra of the Co/CoO NPs after **(A)** ethanol and **(B)** butylamine washing.

Rotating-disk electrode (RDE) measurements were further carried out to study ORR activity and kinetics on G, C–Co/CoO NPs, and G–Co/CoO NPs in the O_2-saturated KOH (0.1M) solution. Figure 3B shows the ORR polarization curves obtained at a rotation rate of 1600 rpm. The curve from G has a slow current increase and no current plateau (**Figure 6-8B-i**), thus indicating that the ORR process on G is mainly a two-electron reduction of O_2 to OOH⁻. [24] In contrast, ORR polarization curves from both C–Co/CoO and G–Co/CoO NPs have a sharp increase and reach quickly saturation (**Figure 6-8B-ii, iii**). The G–Co/CoO NPs show a more positive half-wave potential (-0.176 V) for the ORR than the C–Co/CoO NPs (-0.290 V), thus

114

indicating that G as a support indeed leads to a significant enhancement in Co/CoO catalysis for the ORR. RDE measurements also show that the limiting current density increases with increasing rotation rate (**Figure 6-8C**). The corresponding Koutecky–Levich (K–L) plots show the inverse current density (j^{-1}) as a function of the inverse of the square root of the rotation speed ($\omega^{-1/2}$) at different potential values (**Figure 6-8D**). The number of electrons involved per O_2 in the ORR on G–Co/CoO NPs were determined by the Koutecky–Levich equation: [25]

$$1/j = 1/j_k + 1/B\omega^{-1/2} \qquad (1)$$

where j_k is the kinetic current and ω is the electrode rotating rate. B is determined from the slope of the K–L plots based on the Levich equation:

$$B = 0.2nF(D_{O2})^{2/3}v^{-1/6}C_{O2} \qquad (2)$$

where n represents the number of electrons gained per O_2, F is the Faraday constant (F=96485 C/mol), D_{O2} is the diffusion coefficient of O_2 in 0.1m KOH (1.9×10^{-5} cm^2s^{-1}), [25b] n is the kinetic viscosity (0.01 cm^2s^{-1}), and C_{O2} is the bulk concentration of O_2 (1.2×10^{-6} mol/cm^3). **Figure 6-8D** shows three linear K–L plots at different potentials, suggesting the first order reaction kinetics toward the concentration of O_2 on G–Co/CoO NPs from -0.3 V to -0.7 V. n in Equation (2) can be calculated to be between 4.08–4.15, thereby indicating that the ORR from -0.3 V to -0.7 V is dominated by a four-electron (4e⁻) process and O_2 is reduced to OH⁻. Similarly, the ORR kinetics on the C–Co/CoO NPs can be analyzed (**Figure 6-8E**). The corresponding K–L plots (**Figure 6-8F**) give n=3.9 at -0.5 V, thus revealing that the

C–Co/CoO NPs still favor a 4e oxygen reduction process. Furthermore, compared to those from the C–Co/CoO NPs (**Figure 6-8E**), the ORR polarization curves from the G–Co/CoO NPs (**Figure 6-8C**) have steeper slopes in the kinetic region, thereby further confirming that the G–Co/CoO NPs are more favorable for oxygen reduction than the C–Co/CoO NPs.
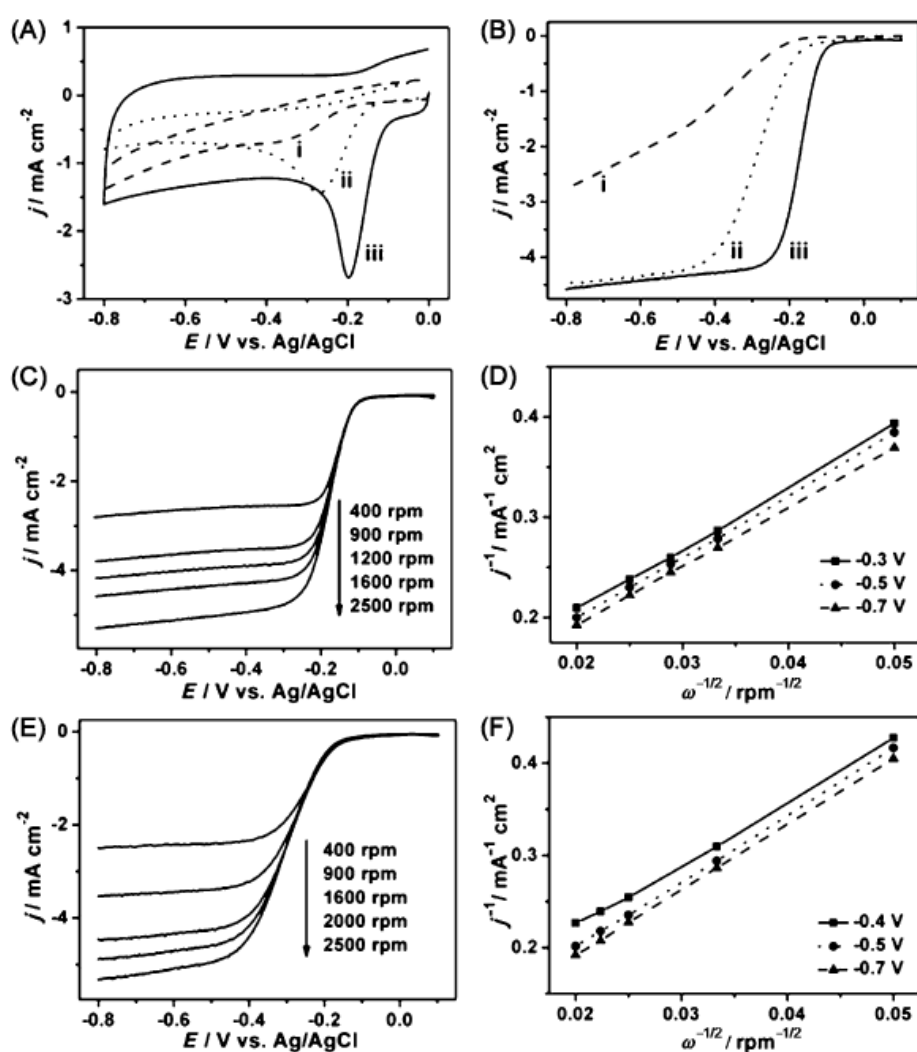
Figure 6-8. (**A**, **B**) CVs (**A**) and ORR polarization curves (**B**) of GC electrodes modified with G (i), C–Co/CoO (ii), and G–Co/CoO (iii). (**A**): scan rate: 50 mV/s; (**B**): scan rate: 10 mV/s and rotation rate: 1600 rpm. (**C**, **E**) ORR polarization curves of G–Co/CoO (**C**) and C–Co/CoO (**E**) at different rotation rates. (**D,F**) K–L plots of the ORR from G–Co/CoO (**D**) and C–Co/CoO (**F**).

The measurements were performed in O_2-saturated KOH (0.1M) solution.

When considering that the Co core in Co/CoO NPs may have an important role in enhancing the catalytic activity in the ORR, we further studied the activities of the G–Co/CoO NPs with different CoO thicknesses under the same condition (**Figure 6-9A**). With the increased CoO coating from 1 to 3 nm and even thicker, the G–Co/CoO NPs exhibited negative polarization shifts, thus indicating that the thin CoO shell facilitates the oxygen reduction. We should note that although the G–Co/CoO NPs with a thick CoO shell have a lower half-wave potential for the ORR, they can still catalyze the ORR through a 4e process (**Figure 6-10 & 6-11**).
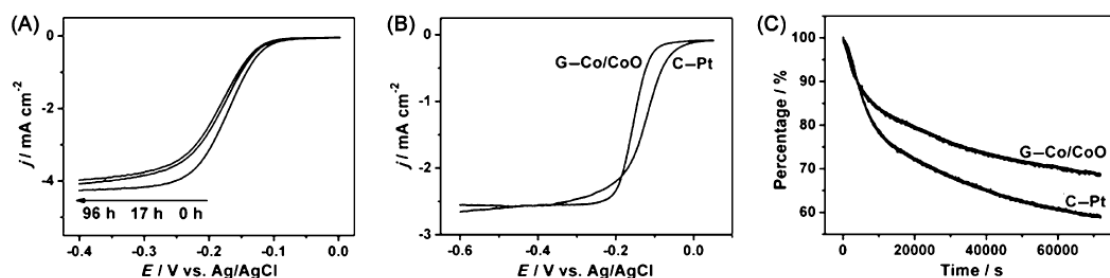
Figure 6-9. (A) ORR polarization curves of G–Co/CoO NPs heated at 70 ℃ in air for 0 h, 17 h, and 96 h. (B) ORR polarization curves of the G–Co/CoO NPs and commercial C–Pt catalyst. Scan rate: 10 mV/s in (A) and (B), and rotation rate: 1600 rpm in (A) and 400 rpm in (B). (C) The chronoamperometric responses for the ORR on the G–Co/CoO NPs and commercial C–Pt catalyst at -0.3 V. Rotation rate: 200 rpm. The measurements were performed in O_2-saturated KOH (0.1m) solution.
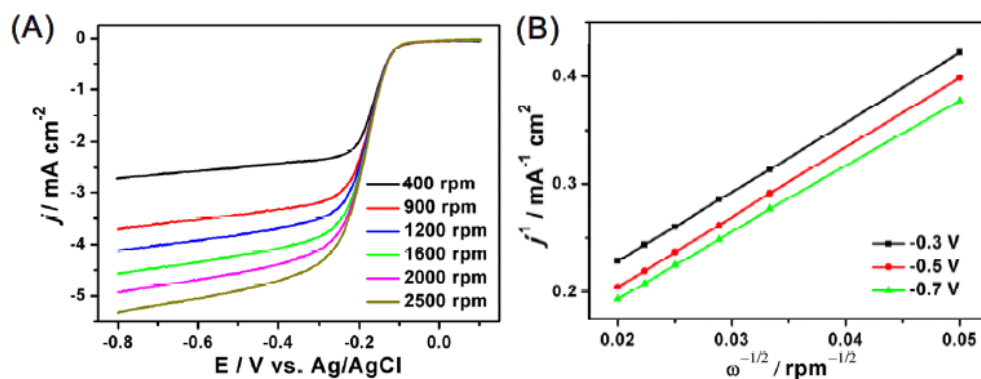
Figure 6-10. (**A**) ORR polarization curves at various rotation rates and (**B**) K-L plots on G-Co/CoO NPs treated at 70 ℃ in air for 17 h. The measurements were performed in the O_2-saturated 0.1 M KOH solution.
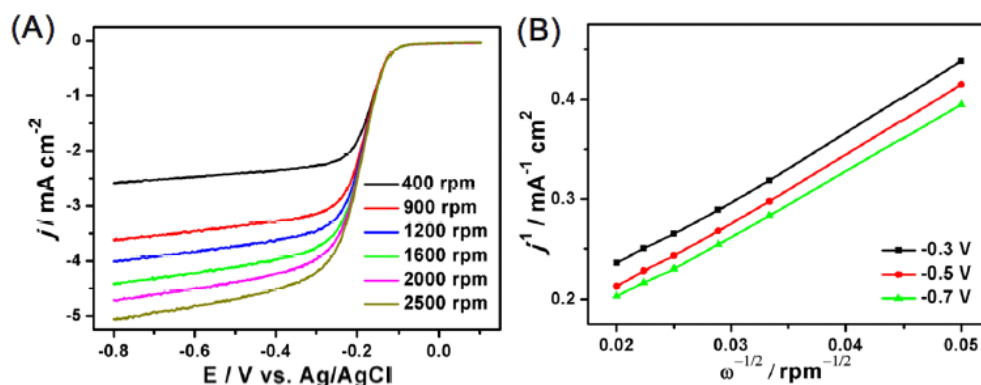
Figure 6-11. (**A**) ORR polarization curves at various rotation rates and (**B**) K-L plots on G-Co/CoO NPs treated at 70 ℃ in air for 96 h. The measurements were performed in the O2-saturated 0.1 M KOH solution.

The ORR catalytic activity of the G–Co/CoO NPs was compared with that of the commercial C–Pt catalyst in the O_2-saturated KOH (0.1M) solution. The half-wave potential difference between G–Co/CoO and C–Pt is 25 mV under the same condition (**Figure 6-9B**). However, the G–Co/CoO NPs have a steeper polarization curve and a higher current density than the C–Pt catalyst from -0.185 V to -0.6 V, thereby indicating that G–Co/CoO and C–Pt have a comparative activity in the ORR. The

durability of the G–Co/CoO NPs and C–Pt was also evaluated by using a chronoamperometric method at -0.3 V (**Figure 6-9C**). The current densities from both G–Co/CoO and C–Pt decrease with time in the same pace initially. But G–Co/CoO shows a slower decrease than C–Pt after 20 h stability test, demonstrating a longer-term stability of the G–Co/CoO over the C–Pt/catalyst. A similar study indicates that G–Co/CoO is also more stable than C–Co/CoO (**Figure 6-12**). These results prove that G can activate and stabilize Co/CoO NPs more efficiently for the ORR and the present G–Co/CoO NPs are a promising alternative to the C–Pt catalyst in KOH.
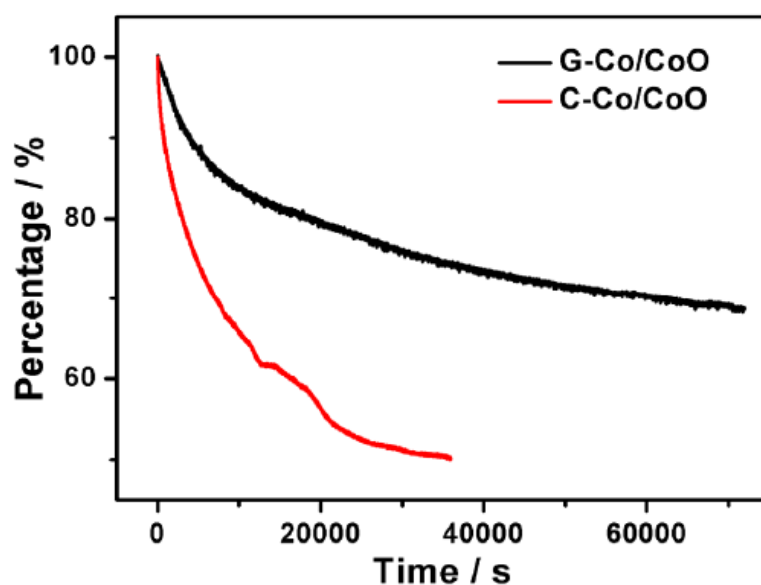
Figure 6-12. The chronoamperometric responses of the G-Co/CoO NPs and C-Co/CoO NPs in the O_2-saturated 0.1 M KOHsolution at -0.3 V. Electrode rotation rate: 200 rpm.

6.3 Summary

In summary, the G–Co/CoO NPs have been synthesized by self-assembly of Co NPs onto the surface of G. The Co NPs tend to form a layer (ca. 1 nm) of natural CoO once they are exposed to ambient environment. This CoO layer prevents Co from deep oxidation unless the Co/CoO NPs (1 nm shell) are heated at an elevated temperature (70 °C). With this controlled oxidation, we have obtained a series of G–Co/CoO NPs with tunable Co size and CoO thickness. Co in Co/CoO NPs can be completely oxidized by an excess of Me_3NO, thereby forming hollow CoO NPs. Compared to G and C–Co/CoO NPs, the G–Co/CoO NPs show much enhanced catalytic activity for the ORR in O_2-saturated KOH (0.1M) solution, and their activity depends on the CoO thickness; the G–Co/CoO NPs with a 1 nm CoO shell show the maximum activity. The work demonstrates the importance of Co/CoO dimension and G as a support in tuning electrocatalysis for efficient ORR. The optimized G–Co/CoO NPs have a comparative activity and better stability than the commercial C–Pt NPs and may serve as a promising alternative to C–Pt catalysts for the ORR in alkaline solutions.

6.4 Experimental

Chemicals. Dicobalt octacarbonyl ($Co_2(CO)_8$, stabilized with 1-10% hexane), 1-octadecene ODE (90%), oleylamine (OAm, >70%), dimethylformamide (DMF, 99.9%), trimethylamine N-oxide (Me_3NO, 98%), butylamine (99%), dioctylamine (DOA, 98%), 1,2,3,4-tetrahydronaphthalene (99%), oleic acid (OA, technical grade,

90%), hexane (98.5%), ethanol (100%) and Nafion (5% in a mixture of lower aliphatic alcohols and water) were all purchased from Aldrich. The C-Pt (20% mass loading, 2.5-3.5 nm Pt nanoparticles (NPs)) catalyst was obtained from Fuel Cell Store.

Synthesis of Graphene. The mixture containing 100 mL of DMF dispersion of GO (1 mg/mL) and 4 mL ammonium hydroxide (25% wt.) was heated and the solution was refluxed for 6 h and cooled down to room temperature to convert GO to G.

Synthesis of Co and CoO Hollow NPs. (a) First, a mixture containing 0.35 mL of OA, 0.5 mL of DOA and 18 mL of 1,2,3,4-tetrahydrophthalene was heated at 110 ℃ for 0.5 h under nitrogen protection and then cooled down to room temperature. 0.54 g of $Co_2(CO)_8$ was quickly added into the above solution and the mixture was reheated to 100 ℃ for 30 min, followed by rapidly heating to 208 ℃ for 30 min at the heating rate of 15 ^{o}C/min under nitrogen protection. After cooled to room temperature, the obtained Co NPs were precipitated by adding 60 mL of ethanol. The product was separated by centrifugation at 9000 rpm for 10 min. The Co NPs were dispersed in hexane before use. **(b)** In a typical synthesis of CoO hollow NPs, a mixture containing 20 mL of ODE, 1 mL of OAm and 50 mg of Me3NO was heated to 130 ℃ under a constant N_2 flow for 1 h. A dispersion of 25 mg of Co NPs in hexane was added to the mixture, and kept at 130 ℃ for 20 min to remove hexane and then

heated at 230 ℃ for 2 h. The reaction solution was cooled to room temperature and the hollow CoO NPs were separated by 40 mL ethanol.

Synthesis of G-Co/CoO and C-Co/CoO. Co NPs (60 mg) dispersed in hexane (60 mL) were added into a DMF solution (60 mL) of G (1 mg/mL) under sonication, and the mixture was further sonicated for one hour. Similarly, Co NPs (60 mg) were also deposited on Ketjen carbon (60 mg) by sonication to make C–Co/CoO NPs. [26] After ethanol (120 mL) was added, the precipitate was separated from the solvents by centrifuging for ten minutes at 9500 rpm. The as-obtained NP catalyst was dispersed in butylamine (60 mL) through sonication, and further stirred for three days at ambient temperature. [23] After ethanol (60 mL) was further added into the above butylamine solution, the catalyst was centrifuged at 9000 rpm for ten minutes. After that, the catalyst was further dried and divided into several parts. Two parts of catalysts were heated at 70 ℃ in air for 17 h and 96 h to get G–Co/CoO core/shell NPs with different shell thickness.

Catalyst Preparation and Deposition on The Working Electrode. The NP catalyst was redispersed in a mixture of solvents containing water, isopropanol, and Nafion (5%) (v/v/v=4:1:0.025) to form a 2 mg/mL suspension. The GC working electrode was first polished with 1.0 and 0.05 mm alumina powder, rinsed with deionized water, and sonicated first in ethanol and then in double-distilled water. The catalyst ink (10

mL) was casted on the electrode and dried at ambient condition. CVs of different catalysts were carried out in a KOH (0.1 M) solution at a scan rate of 50 mV/s. The RDE measurements of different catalysts were conducted in O_2-saturated KOH (0.1 M) solution at the scan rate of 10 mV/s and different rotation rates.

Characterization. TEM images were acquired on a Philips CM 20 EM microscope operating at 200 kV. X-ray diffraction (XRD) characterization was carried out on a Bruker AXS D8-Advanced diffractometer with Cu Ka radiation (λ =1.5418 Å). HRTEM image was obtained on a JEOL 2010 with an accelerating voltage of 200 kV. Magnetic studies were carried out using a Lakeshore 7404 highsensitivity vibrating sample magnetometer (VSM) with fields up to 1.5 T. The electrochemical measurements were performed on a potentiostat (Autolab 302) with Ag/AgCl (vs. 4M KCl) as a reference electrode and Pt wire as a counter electrode.

Reference

1. Y. Bing, H. Liu, L. Zhang, D. Ghosh, J. Zhang, *Chem. Soc. Rev.* **2010**, *39*, 2184 – 2202.

2. Z. Peng, H. Yang, *J. Am. Chem. Soc.* **2009**, *131*, 7542 – 7543.

3. M.-H. Shao, K. Sasaki, R. R. Adzic, *J. Am. Chem. Soc.* **2006**, *128*, 3526 – 3527.

4. V. R. Stamenkovic, B. Fowler, B. S. Mun, G. J. Wang, P. N. Ross, C. A. Lucas, N. M. Markovic, *Science* **2007**, *315*, 493 – 497.

5. S. Guo, E. Wang, *Nano Today* **2011**, *6*, 240 – 264.

6. G. Wu, K. L. More, C. M. Johnston, P. Zelenay, *Science* **2011**, *332*, 443 – 447.

7. S. Guo, S. Dong, *Chem. Soc. Rev.* **2011**, *40*, 2644 – 2672.

8. S. Guo, S. Dong, E. Wang, *ACS Nano* **2010**, *4*, 547 – 555.

9. S. Guo, D. Wen, S. Dong, E. Wang, *ACS Nano* **2010**, *4*, 3959 – 3968.

10. Y. Li, Y. Zhao, H. Cheng, Y. Hu, G. Shi, L. Dai, L. Qu, *J. Am. Chem. Soc.* **2012**, *134*, 15 – 18.

11. L. Qu, Y. Liu, J.-B. Baek, L. Dai, *ACS Nano* **2010**, *4*, 1321 – 1326.

12. Z.-H. Sheng, L. Shao, J.-J. Chen, W.-J. Bao, F.-B. Wang, X.-H. Xia, *ACS Nano* **2011**, *5*, 4350 – 4358.

13. Z. Yao, H. Nie, Z. Yang, X. Zhou, Z. Liu, S. Huang, *Chem. Commun.* **2012**, *48*, 1027 – 1029.

14. Y. Li, W. Zhou, H. Wang, L. Xie, Y. Liang, F. Wei, J.-C. Idrobo, S. J. Pennycook, H. Dai, *Nat. Nanotechnol.* **2012**, *7*, 394 – 400.

15. Y. Liang, Y. Li, H. Wang, J. Zhou, J. Wang, T. Regier, H. Dai, *Nat. Mater.* **2011**, *10*, 780 – 786.

16. Z.-S. Wu, S. Yang, Y. Sun, K. Parvez, X. Feng, K. M_llen, *J. Am. Chem. Soc.* **2012**, *134*, 9082 – 9085.

17. H. Wang, Y. Liang, Y. Li, H. Dai, *Angew. Chem.* **2011**, *123*, 11161 – 11164; *Angew. Chem. Int. Ed.* **2011**, *50*, 10969 – 10972.

18. Y. Liang, H.Wang, J. Zhou, Y. Li, J. Wang, T. Z. Regier, H. Dai, *J. Am. Chem. Soc.* **2012**, *134*, 3517 – 3523.

19. S. Guo, S. Sun, *J. Am. Chem. Soc.* **2012**, *134*, 2492 – 2495.

20. S. Peng, J. Xie, S. Sun, *J. Solid State Chem.* **2008**, *181*, 1560 – 1564.

21. S. Peng, S. Sun, *Angew. Chem.* **2007**, *119*, 4233 – 4236; *Angew. Chem. Int. Ed.* **2007,** *46*, 4155 – 4158.

22. Y. Yin, R. M. Rioux, C. K. Erdonmez, S. Hughes, G. A. Somorjai, A. P. Alivisatos, *Science* **2004**, *304*, 711 – 714.

23. J. Wu, J. Zhang, Z. Peng, S. Yang, F. T. Wagner, H. Yang, *J. Am. Chem. Soc.* **2010**, *132*, 4984 – 4985.

24. Y. Zheng, Y. Jiao, J. Chen, J. Liu, J. Liang, A. Du, W. Zhang, Z. Zhu, S. C. Smith, M. Jaroniec, G. Q. Lu, S. Z. Qiao, *J. Am. Chem. Soc.* **2011**, *133*, 20116 – 20119.

25. a) S. Wang, D. Yu, L. Dai, *J. Am. Chem. Soc.* **2011**, *133*, 5182 –5185; b) S. Wang, D. Yu, L. Dai, D.W. Chang, J.-B. Baek, *ACS Nano* **2011**, *5*, 6202 – 6209;

c) S.Wang, E. Iyyamperumal, A. Roy, Y. Xue, D. Yu, L. Dai, *Angew. Chem.* **2011**, *123*, 11960 – 11964; *Angew. Chem. Int. Ed.* **2011**, *50*, 11756 – 11760; d) K. Gong, F. Du, Z. Xia, M. Durstock, L. Dai, *Science* **2009**, *323*, 760 – 764.

26. a) V. Mazumder, S. Sun, *J. Am. Chem. Soc.* **2009**, *131*, 4588 – 4589; b) S. Guo, S. Zhang, X. Sun, S. Sun, *J. Am. Chem. Soc.* **2011**, *133*, 15354 – 15357.

Chapter 7

Structure-Induced Enhancement in Electrooxidation of Trimetallic FePtAu Nanoparticles

In the chapter 3-6, I have discussed about the synthetic tuning nanoparticles (NPs) for oxygen reduction reaction (ORR) which happens at the cathode of the proton exchange membrane fuel cells. In this chaper, we demonstrate the structure-control strategy to tune and optimize NP catalysis for electrooxidation reactions using FePtAu nanoparticles (NPs) as an example. The presence of Au in FePtAu facilitates FePt structure transformation from chemically disordered face centered cubic (*fcc*) structure to chemically ordered face centered tetragonal (*fct*) structure, and further promotes formic acid oxidation reaction (FAOR). In 0.5 M H_2SO_4 + 0.5 M HCOOH solution, The *fct*-FePtAu NPs have the mass activity as high as 2809.9 mA/mg Pt and retain 92.5% of this activity after 13 h stability test. They become the most efficient NP catalyst ever reported for FAOR. This structure-control strategy can be extended to other multi-metallic NP systems and other electrooxidation reactions, providing a general approach to advanced NP catalysts with desired activity and durability control for practical applications.

7.1 Background and Motivation

Recent advance in nanoparticle (NP) synthetic methodology has led to the formation of various monodisperse metallic NPs with ever increased activity to catalyze oxidation of fuel (hydrogen, formic acid, or alcohol) and reduction of oxygen in polymer electrolyte membrane fuel cell conditions.[1-3] Among all the NPs studied, Pt and its alloy NPs have constantly been the catalyst choice due to their high activity for fuel oxidation and oxygen reduction reactions.[4-12] However, these Pt-based NPs have shown serious limitations in their fuel cell catalysis: they are unstable in the corrosive electrochemical environment and prone to deactivation by reaction intermediate species such as carbon monoxide (CO).[13] As a result, NP catalysts based on elemental Pt and composition-controlled Pt-alloys are far from optimized for fuel cell applications. Very recently, core/shell type NPs with a thin (< 2 nm) uniform coating of Pt-shell were prepared and demonstrated to be a robust class of catalyst for oxygen reduction reaction.[14-16] Despite this progress, there is still no reliable approach to NP catalysts with simultaneous enhancement in both activity and durability for practical fuel oxidation reactions.

This chapter presents a new structure-control strategy to tune and optimize NP catalysis for fuel oxidations. NPs, especially multimetallic NPs, can adopt different crystal structures. For example, as synthesized from a high temperature solution-phase reaction, monodisperse binary FePt NPs have the chemically disordered face centered cubic (*fcc*) structure in which Fe and Pt atoms occupy

randomly the *fcc* crystal lattice.[17] When further annealed, the *fcc*-structure can be converted into chemically ordered face centered tetragonal (*fct*) structure in which Fe and Pt atoms form alternating atomic layers stacked along one specific direction.[17] Such a structure conversion in FePt can result in drastic magnetic property change from superparamagnetism to ferromagnetism[18] and in ORR catalytic enhancement in acid solutions as we discussed in Chapter 3.[19] It is these interesting phenomena in *fct*-FePt that leads to the current work to explore structure-induced NP catalysis for electrooxidation reactions with simultaneous enhancement in both activity and durability. The catalyst described here is monodisperse trimetallic FePtAu NPs. The presence of Au in FePtAu facilitates FePt structural transformation from *fcc* to *fct* with Au segregating on the *fct*-FePt surface and further promotes formic acid oxidation reaction (FAOR) - the anode reaction that is used to power direct formic acid fuel cells.[20] Compared to Pt and FePt NPs catalysts, the *fct*-FePtAu NPs show high CO poisoning-resistance, achieve mass activity of 2809.9 mA/mg Pt and retain 92.5% of this activity after 13 h stability test. They become the most active and durable catalyst ever reported for FAOR.

7.2 Results and Discussion

7.2.1 Synthetic Control of FePtAu NPs

FePtAu NPs were synthesized by co-reduction of platinum acetylacetonate, Pt(acac)$_2$, and chloroauric acid hydrate, HAuCl$_4$•xH$_2$O, and thermal decomposition of

iron pentacarbonyl, $Fe(CO)_5$ (**see Experimental**). The excess of $Fe(CO)_5$ was added to function both as a reducing agent and as a Fe precursor for its alloying with Pt and Au. Oleylamine and tetradecylphosphonic acid were used to stabilize the NPs. FePtAu compositions were controlled by varying the molar ratios of $Pt(acac)_2$, $HAuCl_4 \cdot xH_2O$, and $Fe(CO)_5$ and were analyzed by inductively coupled plasma-atomic emission spectroscopy (ICP-AES) (**Table 7-1**). 4 nm $Fe_{55}Pt_{45}$ NPs were also synthesized similarly without the presence of Au salt. Transmission electron microscopy (TEM) images show that the as-synthesized FePt and FePtAu NPs have an average size of 4 nm ± 0.2 nm for $Fe_{55}Pt_{45}$ (**Figure 7-1A**), 4 nm ± 0.2 nm for $Fe_{42}Pt_{44}Au_{14}$ (**Figure 7-1B**), 4 nm ± 0.2 nm for $Fe_{43}Pt_{37}Au_{20}$ (**Figure 7-2A**) and 4 nm ± 0.3 nm for $Fe_{34}Pt_{34}Au_{32}$ NPs (**Figure 7-1C**).

Sample	$Pt(acac)_2/HAuCl_4$ molar ratio	As-synthesized NPs
A	3:1	$Fe_{42}Pt_{44}Au_{14}$
B	3:2	$Fe_{43}Pt_{37}Au_{20}$
C	3:3	$Fe_{34}Pt_{34}Au_{32}$

Table 7-1. The composition control of as-synthesized FePtAu NPs by varying the molar ratios of $Pt(acac)_2/HAuCl_4$.
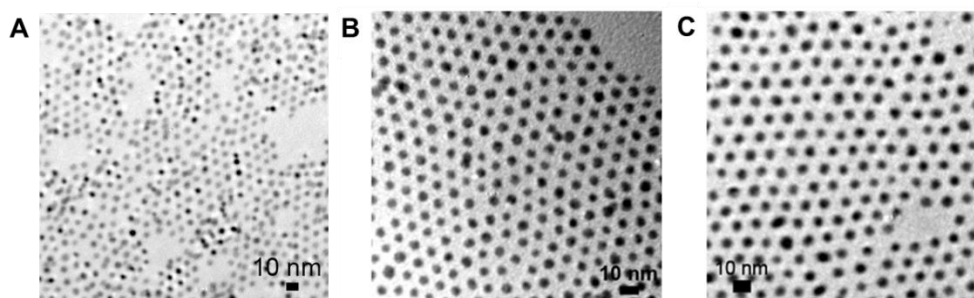
Figure 7-1. TEM images of (**A**) the 4 nm $Fe_{55}Pt_{45}$, (**B**) the 4 nm $Fe_{42}Pt_{44}Au_{14}$ and (**C**) the 4 nm $Fe_{34}Pt_{34}Au_{32}$ NPs.
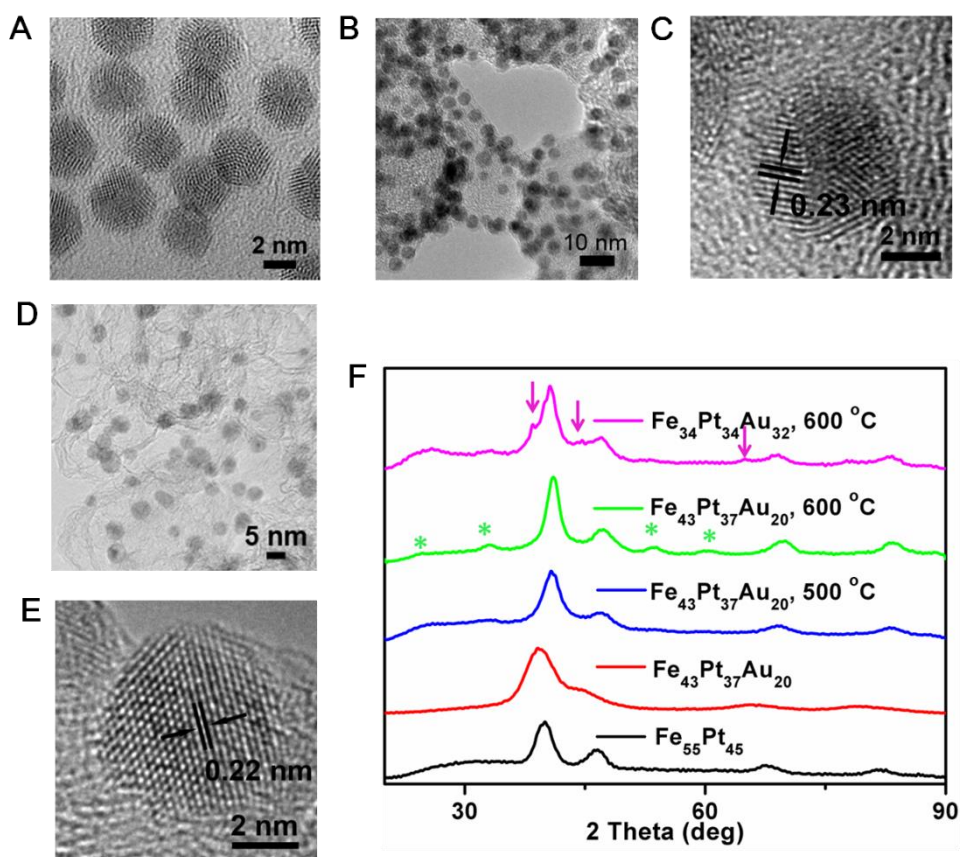
Figure 7-2. TEM images of (**A**) the as-synthesized 4 nm $Fe_{43}Pt_{37}Au_{20}$ NPs, (**B**) the *fcc*-$Fe_{43}Pt_{37}Au_{20}$/C NPs, (**C**) a representative *fcc*-$Fe_{43}Pt_{37}Au_{20}$/C NP, (**D**) the *fct*-$Fe_{43}Pt_{37}Au_{20}$/C NPs and (**E**) a representative *fct*-$Fe_{43}Pt_{37}Au_{20}$/C NP. The as-synthesized NPs were deposited on the amorphous carbon coated Cu grid and the other NPs were deposited on the Ketjen carbon support and annealed under 95% Ar + 5% H_2 at 400 °C (**B, C**) and 600 ℃ (**D, E**) for 1 h. (**F**) XRD patterns of the as-synthesized $Fe_{55}Pt_{45}$ NPs, $Fe_{43}Pt_{37}Au_{20}$ NPs, and the $Fe_{43}Pt_{37}Au_{20}$ NPs annealed at 500 ℃, 600 ℃ (stars denote the *fct*-FePt peaks) as well as the $Fe_{34}Pt_{34}Au_{32}$ NPs

131

annealed at 600 ℃ (arrows denote the Au peaks). The NPs were deposited on the Ketjen carbon support and annealed under 95% Ar + 5% H_2 for 1 h.

Previously, FePt NPs are often synthesized by reduction of $Pt(acac)_2$ and thermal decomposition of $Fe(CO)_5$ in the presence of oleic acid and oleylamine.[17] This same recipe does not work for the current synthesis of FePtAu NPs with the desired size and Fe/Pt/Au composition controls. However, when oleic acid is replaced by tetradecylphosphonic acid, co-reduction of $Pt(acac)_2$ and $HAuCl_4$ and decomposition of $Fe(CO)_5$ yields monodisperse 4 nm FePtAu NPs with Fe/Pt/Au compositions readily controlled by the metal precursor ratios. In this work, the Fe/Pt ratio is kept at near 1/1 to facilitate *fcc-fct* phase transformation,[17] while Au is made to have three different percentages so that Au composition-dependent *fcc-fct* transition and Au-dependent FAOR catalysis can be studied.

High temperature annealing was applied to remove the surfactants around NPs and to convert the *fcc*-FePtAu to *fct*-FePtAu, similar to what we demonstrated in Chapter 3-4. To prevent NPs from aggregation under these annealing conditions and to facilitate the catalytic studies, the as-synthesized NPs were deposited on Ketjen carbon (C) support before the annealing (see Experiment). **Figure 7-2B, 7-2C** show the typical TEM (**B**) and HRTEM (**C**) images of the *fcc*-$Fe_{43}Pt_{37}Au_{20}$ NPs annealed under 95% Ar + 5% H_2 at 400 °C for 1 h. The *fcc*-$Fe_{43}Pt_{37}Au_{20}$ NPs have the average size of 4 $\pm$ 0.2 nm and (111) lattice fringe distance at 0.23 nm. Upon annealing at 600

°C for 1 h, the fcc-Fe$_{43}$Pt$_{37}$Au$_{20}$ NPs are converted to fct-Fe$_{43}$Pt$_{37}$Au$_{20}$ NPs, as shown in the TEM image (**Figure 7-2D**) and high resolution TEM (HRTEM) image (**Figure 7-2E**) of the NPs. The NP morphology integrity observed in these TEM images indicate that the FePtAu NPs deposited on the carbon support are well-protected against aggregation/sintering during the high temperature annealing treatments.

The structure transition of the FePt and FePtAu NPs was monitored by X-ray diffraction patterns of the NPs deposited on C (**Figure 7-2F**). The as-synthesized Fe$_{43}$Pt$_{37}$Au$_{20}$ NPs show a typical fcc pattern with broadened and small angle-shifted peaks compared to the 4 nm fcc-Fe$_{55}$Pt$_{45}$ NPs, suggesting that Au-doping in FePt induces the reduction of crystal coherence length and increase of crystal lattice spacing. When annealed at 400 °C and 500 °C for 1 h, the Fe$_{43}$Pt$_{37}$Au$_{20}$ NPs remain to be fcc, but at 600 °C for 1 h, the fcc-Fe$_{43}$Pt$_{37}$Au$_{20}$ is converted to partially ordered fct-Fe$_{43}$Pt$_{37}$Au$_{20}$. Associated with this structure change, the 4 nm fct-Fe$_{43}$Pt$_{37}$Au$_{20}$ NPs become ferromagnetic and show a coercivity of ~1000 Oe at room temperature while the 4 nm Fe$_{55}$Pt$_{45}$ NPs annealed under the same condition have a coercivity of only ~300 Oe (**Figure 7-3**).[21] These indicate that Au segregation from the FePtAu structure helps to create lattice vacancies within the 4 nm FePtAu structure, promoting Fe, Pt rearrangement. This supports what has been proposed in Au doping effect on FePt structure transformation.[22, 23] Our studies further show that the fct-structure formation within FePtAu is Au composition-dependent with Au in 20% (by atomic percentage) range forming better chemical order within the FePt structure.

Adding more Au to the FePtAu structure seems to have no benefit for *fcc-fct* transition as the $Fe_{34}Pt_{34}Au_{32}$ NPs annealed at 600 ℃ exhibit weaker/broader *fct* peaks than the $Fe_{43}Pt_{37}Au_{20}$ NPs (**Figure 7-2F**).
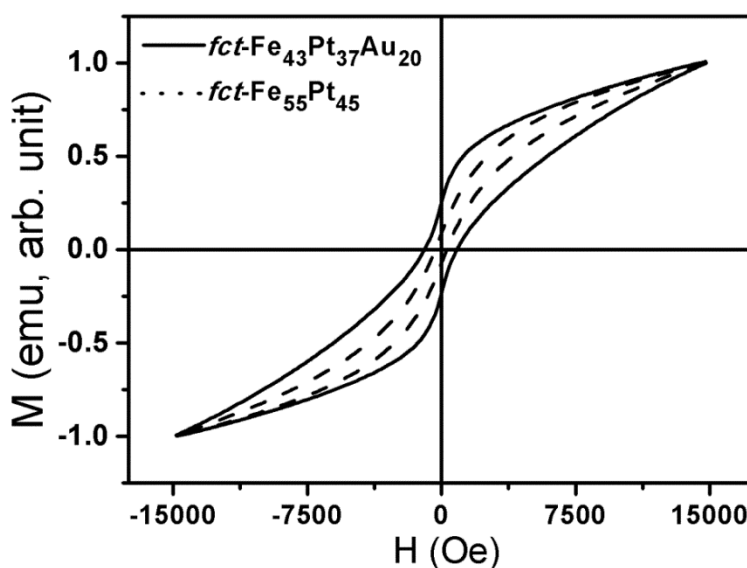
Figure 7-3. Room temperature hysteresis loops of the 4 nm *fct*-$Fe_{55}Pt_{45}$ NPs (dot curve) and *fct*-$Fe_{43}Pt_{37}Au_{20}$ NPs (solid curve).

The carbon-supported $Fe_{43}Pt_{37}Au_{20}$ NPs annealed at 400 °C and 600 °C respectively were further characterized by atomically resolved aberration-corrected scanning transmission electron microscopy (STEM), STEM-electron energy-loss spectroscopy (STEM-EELS) and STEM-energy dispersive X-ray spectroscopy (STEM-EDS). **Figure 7-4A** is the high-angle annular dark field (HAADF) image of a

representative fcc-Fe$_{43}$Pt$_{37}$Au$_{20}$ NP and **Figure 7-4B-D** are the corresponding Fe elemental mapping of this NP using STEM-EELS method. These analyses indicate that Fe in the fcc-structure is uniformly distributed. In contrast, HAADF image and the corresponding Fe elemental mapping of the fct-Fe$_{43}$Pt$_{37}$Au$_{20}$ NP (**Figure 7-4E-H**) show that Fe is concentrated in the core region and Au/Pt are rich in the shell structure. The STEM-EDS line scans confirm that Au alloys uniformly with Fe and Pt in the fcc-Fe$_{43}$Pt$_{37}$Au$_{20}$ NPs (**Figure 7-4I**) but in the fct-Fe$_{43}$Pt$_{37}$Au$_{20}$ structure, it diffuses out and concentrates around the shell (**Figure 7-4J**). Based on the STEM-EELS and STEM-EDS analyses, the annealing-induced structure change of FePtAu can be illustrated in **Figure 7-5**. When annealed at 400 °C, the fcc structure is better formed in FePtAu NPs. At 600 °C, the fcc-FePtAu is converted to fct-FePtAu with Au-segregating on the FePt NP surface.[24] Such a unique structure pattern is essential for fct-FePtAu NPs to show the enhanced activity and durability for FAOR.
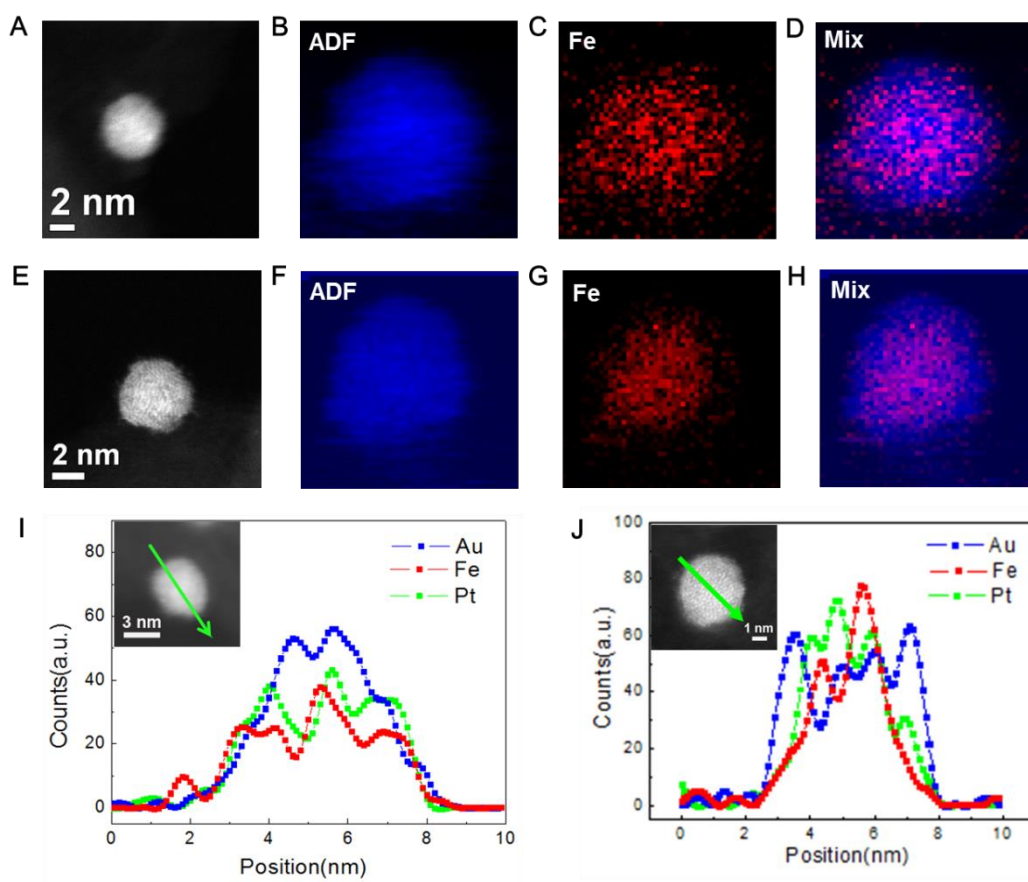
Figure 7-4. (A) STEM imaging and (B)-(D) simultaneous 2D STEM-EELS mapping from a representative *fcc*-Fe$_{43}$Pt$_{37}$Au$_{20}$ NP. (E) STEM imaging and (F)-(H) simultaneous 2D STEM-EELS mapping from a representative *fct*-Fe$_{43}$Pt$_{37}$Au$_{20}$ NP. (I, J) STEM-EDS line scans crossing *fcc*-Fe$_{43}$Pt$_{37}$Au$_{20}$ (I) and *fct*-Fe$_{43}$Pt$_{37}$Au$_{20}$ (J) NPs. The insets show the NPs scanned.
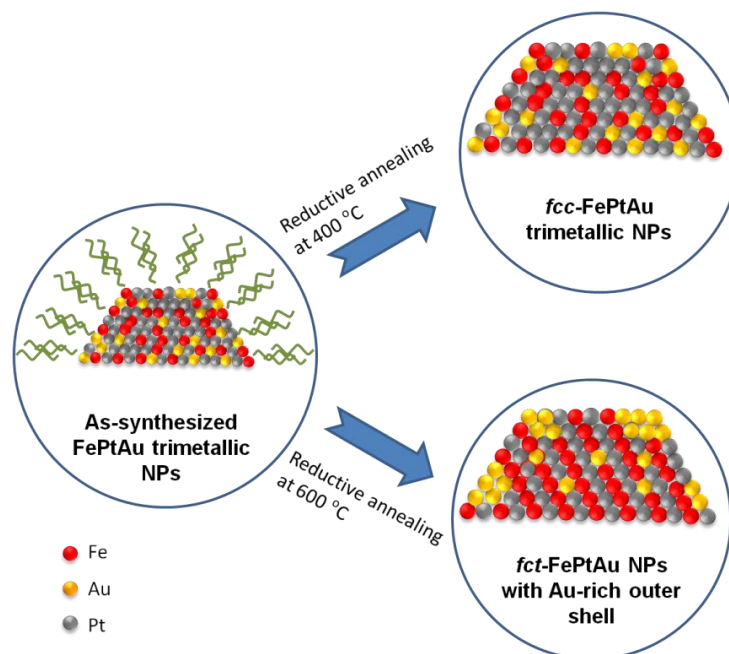
Figure 7-5. Schematic illustration of the structural change of the FePtAu NPs upon annealing. When annealed at 400 °C, the FePtAu NPs are *fcc* structured, but at 600 °C, the *fct*-FePtAu structure is formed with Au-segregating on the NP surface.

7.2.2 Electrocatalysis of Structure/Composition-Controlled FePtAu NPs

The Au composition effect of the 4 nm *fct*-FePtAu NPs on FAOR was first studied to obtain the optimum Au composition for further catalytic studies. **Figure 7-6A** and **Figure 7-6B** show the cyclic voltammograms (CVs) of three different kinds of *fct*-FePtAu NPs in the N_2-saturated 0.5 M H_2SO_4 solution. The peaks appearing in the range of -0.25 to 0.15 V are attributed to hydrogen underpotential formation/stripping (H_{UPD}) and are used to estimate the electrochemical active surface area of the NPs

(Figure 6-6A).[25] The peaks in 0.3-0.9 V are from metal oxidation/reduction - more Au content in the NP structure leads to stronger Au reduction peaks at 0.80 V (**Figure 7-6B**). The electro-oxidation activity of these fct-FePtAu NPs in 0.5 M H_2SO_4 and 0.5 M HCOOH is normalized against NP surface area and is plotted as curves of the current density (j) $vs.$ the applied potentials (V) (**Figure 7-6C**). For the fct-$Fe_{42}Pt_{44}Au_{14}$ NPs, the first current maximum at 0.47 V in the forward scan is due to the direct oxidation of HCOOH to CO_2 (dehydrogenation reaction), while the second current maximum at 0.71 V corresponds to oxidation of CO generated from the dehydration reaction of HCOOH.[11] The stability of these fct-FePtAu NPs was tested by chronoamperometry (CA) as shown in the j change of FAOR over time (t) at 0.2 V (**Figure 7-6D**).[26] Among three different kinds of fct-FePAu NPs studied, the fct-$Fe_{43}Pt_{37}Au_{20}$ NPs have the best long-term stability.
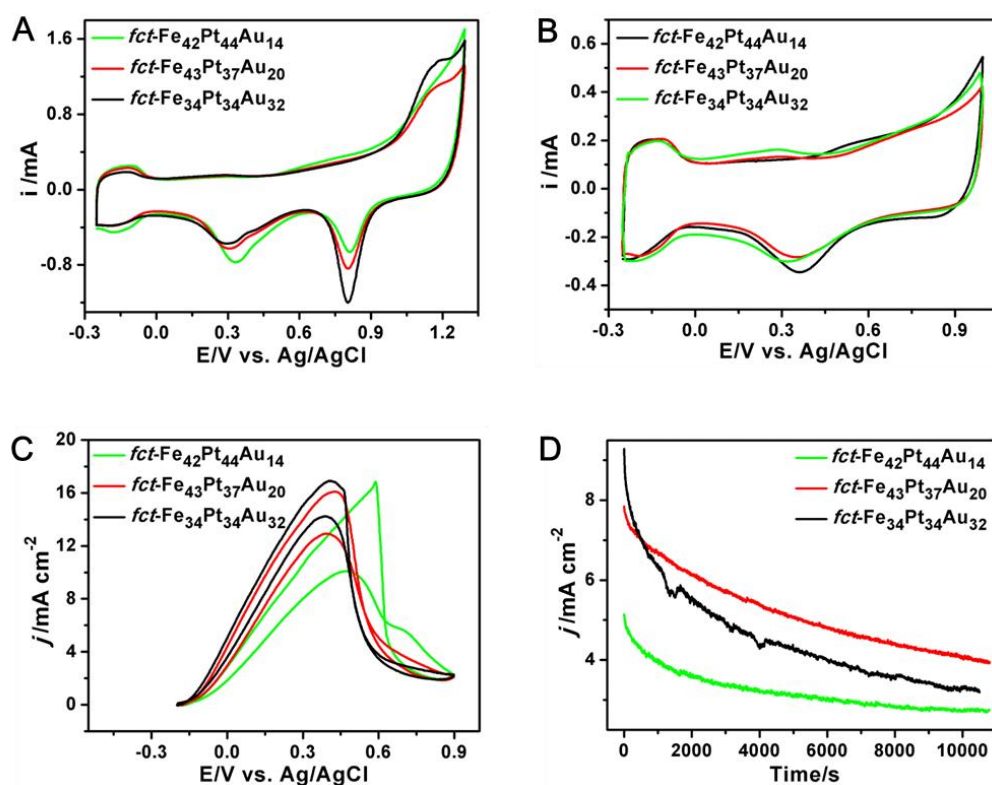
Figure 7-6. (**A, B**) CVs of the *fct*-FePtAu NPs with different compositions in the N$_2$-saturated 0.5 M H$_2$SO$_4$ solution with the potentials scanned from -0.25 to 1.0 V (**A**) and -0.25 to 1.30 V (**B**). (**C**) *j-V* curves of the *fct*-FePtAu NPs with different compositions in the N$_2$-saturated 0.5 M H$_2$SO$_4$ + 0.5 M HCOOH solutions. (**D**) *j-t* curves of the *fct*-FePtAu NPs with different compositions reflecting the specific activity change over time.

The structure effect of the Fe$_{43}$Pt$_{37}$Au$_{20}$ NPs on FAOR catalysis was investigated. **Figure 7-7A&7-7B** show the CVs of the Fe$_{43}$Pt$_{37}$Au$_{20}$ NPs annealed at different temperatures. With the increase in annealing temperatures from 400 to 600 ℃, the Pt-based reduction peak potentials shift negatively, indicating the better Fe-alloy effect to Pt in *fct*-FePt than in *fcc*-FePt structure. The FAOR catalyzed by the Fe$_{43}$Pt$_{37}$Au$_{20}$ NPs annealed at different temperatures are shown in **Figure 7-7C**. The

fcc-Fe$_{43}$Pt$_{37}$Au$_{20}$ NPs obtained from 400 ℃ annealing display an obvious CO-oxidation peak at 0.7 V. Increasing the annealing temperature to 500 ℃ results in the intensity drop of this oxidation peak. The NPs annealed at 600 ℃ for 1 h show no CO-oxidation peak, suggesting that the segregation of Au on the surface of the *fct*-Fe$_{43}$Pt$_{37}$Au$_{20}$ NPs helps CO removal. The FAOR stability of the Fe$_{43}$Pt$_{37}$Au$_{20}$ NPs annealed at different temperatures are shown in **Figure 7-7D**. The Fe$_{43}$Pt$_{37}$Au$_{20}$ NPs annealed at 600 ℃ are more stable for FAOR than any of the other two kinds of NPs treated at 400 and 500 ℃, indicating once again that the *fct* structure favors the durability enhancement of FePtAu NPs for FAOR.
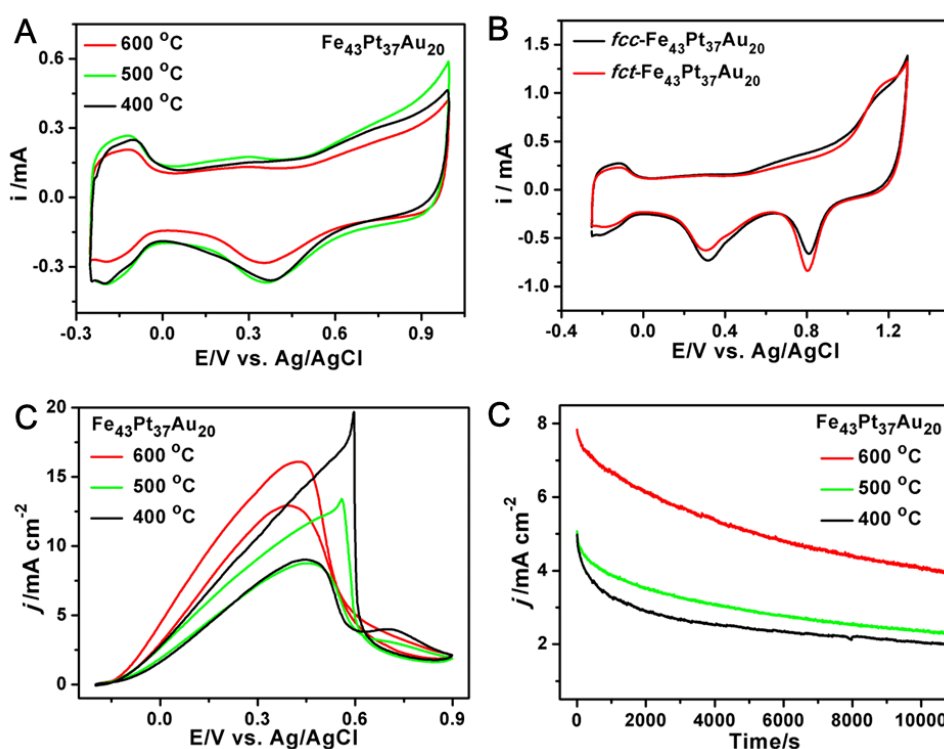
Figure 7-7. (A, B) CVs of the Fe$_{43}$Pt$_{37}$Au$_{20}$ NPs annealed at different temperatures with the

potentials scanned from -0.25 to 1.0 V (**A**) and -0.25 to 1.30 V (**B**) in the N_2-saturated 0.5 M H_2SO_4 solution. (**C**) j-V curves of the $Fe_{43}Pt_{37}Au_{20}$ NPs annealed at different temperatures in the N_2-saturated 0.5 M H_2SO_4 + 0.5 M HCOOH solutions. (**D**) j-t curves of the $Fe_{43}Pt_{37}Au_{20}$ NPs annealed at different temperatures reflecting the specific activity change over time.

The fct-$Fe_{43}Pt_{37}Au_{20}$ NPs are much more active and durable catalyst for FAOR than the fct-$Fe_{55}Pt_{45}$ NPs and the commercial Pt NPs. **Figure 7-8A** and **Figure 7-8B** show the comparison of CVs and j-V curves respectively for these NPs. As expected, the Pt catalyst has a very strong CO-oxidation peak at 0.67 V whereas the fct-$Fe_{55}Pt_{45}$ shows a relatively weak peak at 0.69 V, and the fct-$Fe_{43}Pt_{37}Au_{20}$ NPs have no CO-oxidation peak. Without the CO-poisoning effect, the fct-$Fe_{43}Pt_{37}Au_{20}$ NPs have an onset FAOR potential at -0.2 V, which is 0.12 V lower than that of the commercial Pt (-0.08 V). The mass activity of the 4 nm fct-$Fe_{43}Pt_{37}Au_{20}$ NPs reaches 2809.9 mA/mg Pt (Figure 6-9A), which is the highest among all NP catalysts ever reported. Furthermore, the fct-$Fe_{43}Pt_{37}Au_{20}$ NPs are also the most stable NP catalysts for FOAR − their specific activity, drops about 50% at the end of 3 h j-t test (**Figure 7-8C**). Even after 13 h j-t test, their mass activity is still at 2600 mA/mg Pt (92.5% of the original value of 2809.9 mA/mg Pt) (**Figure 7-9B**). As a comparison, under the same measurement conditions, the state-of-art PtBi NPs have the mass activity of about 1720 mA/mg Pt and can keep only about 11% of their initial activity at the end of 3 h j-t test.[11]
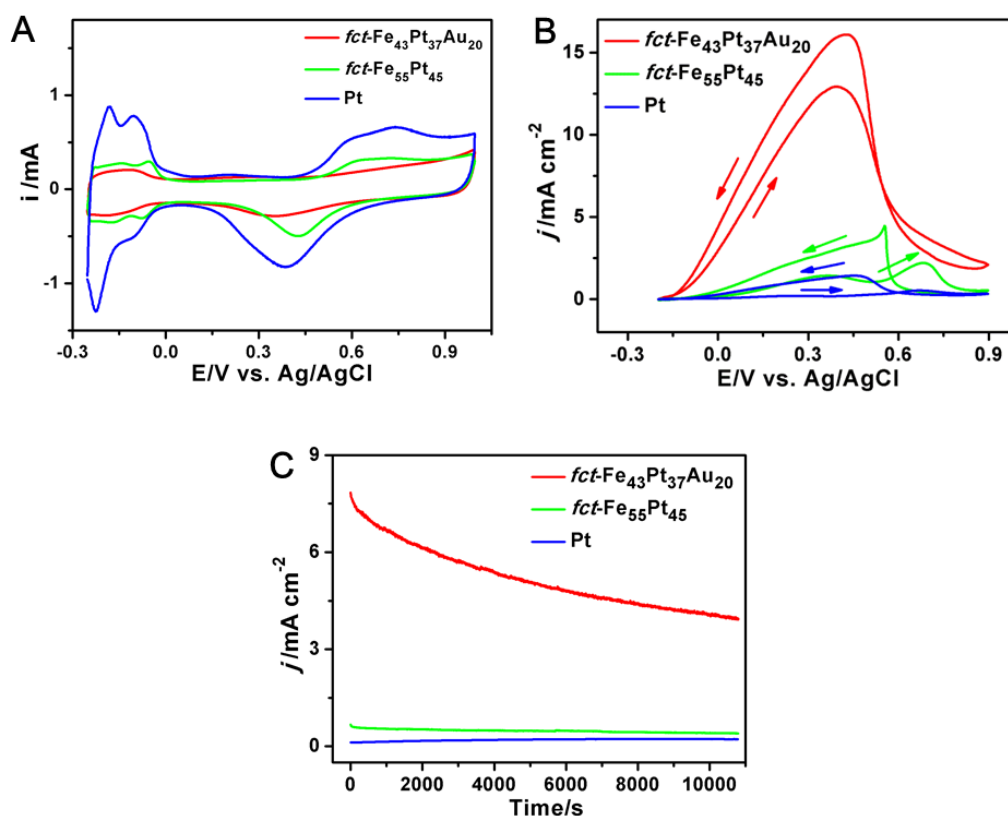
Figure 7-8. (**A**) CVs of the *fct*-Fe$_{43}$Pt$_{37}$Au$_{20}$, *fct*-Fe$_{55}$Pt$_{45}$, and commercial Pt NPs in the N$_2$-saturated 0.5 M H$_2$SO$_4$ solution. (**B**) *j-V* curves of the specific activity of the *fct*-Fe$_{43}$Pt$_{37}$Au$_{20}$, *fct*-Fe$_{55}$Pt$_{45}$ and commercial Pt catalysts in the N$_2$-saturated 0.5 M H$_2$SO$_4$ + 0.5 M HCOOH solutions. (**C**) *j-t* curves of the *fct*-Fe$_{43}$Pt$_{37}$Au$_{20}$, *fct*-Fe$_{55}$Pt$_{45}$, and commercial Pt catalysts.
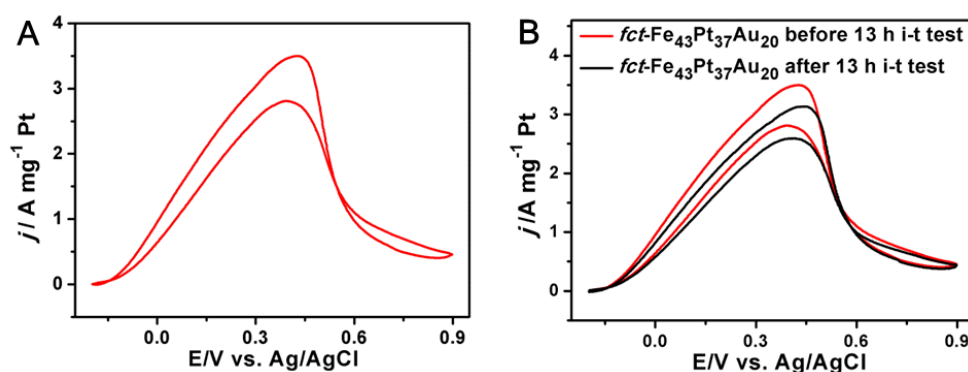
Figure 7-9. (**A**) *j-V* curves of the mass activity of the *fct*-Fe$_{43}$Pt$_{37}$Au$_{20}$ NPs; and (**B**) *j-V* curves of the *fct*-Fe$_{43}$Pt$_{37}$Au$_{20}$ NPs before and after 13 h *i-t* stability test. The studies were performed in the N$_2$-saturated 0.5 M H$_2$SO$_4$ + 0.5 M HCOOH solution.

142

The *fct*-FePtAu structure with Au segregating on the FePt surface is essential for the NPs to show the enhanced activity and durability for FAOR. With the increase of the Au amount to 20% and 32% in the *fct*-$Fe_{43}Pt_{37}Au_{20}$ and *fct*-$Fe_{34}Pt_{34}Au_{32}$ NPs, the CO-related peak in FAOR disappears, indicating that Au on the NP surface promotes the dehydrogenation reaction of HCOOH and inhibits the dehydration reaction that leads to the formation of CO. It seems that Au helps to boost the formation of $HCOO_{ads}$ and its spillover to Pt to facilitate dehydrogenation pathway.[27] The enhanced stability comes likely from the formation of *fct* structure within *fct*-FePtAu NPs promoted by Au doping and segregation. Without the presence of Au and the formation of *fct*-structure, NPs such as Pt, FePt or *fcc*-FePtAu NPs, are all subject to easy CO poisoning and acid dissolution, exhibiting much lower activity and stability for FAOR than the *fct*-FePtAu NPs.

Our study shows that the *fct*-$Fe_{43}Pt_{37}Au_{20}$ NPs are also active for catalyzing methanol oxidation reaction (MOR) with a high CO-tolerance activity (**Figure 7-10**). In the MOR, two oxidation peaks are usually observed. The stronger peak in the forward scan is related to the direct methanol oxidation. The smaller peak in the backward scan is likely associated the oxidation of the carbonaceous species formed on the catalyst surface in the forward scan. The ratio of the forward peak current (I_f) to the backward peak current (I_b), I_f/I_b, is often used as an index to measure the catalyst tolerance to the poisoning species (like CO). A higher ratio indicates more

effective removal of the poisoning species on the catalyst surface. [7, 28] The CV from the fct-Fe$_{43}$Pt$_{37}$Au$_{20}$ NPs has an I_f/I_b value of 2.8, while for the fcc-Fe$_{43}$Pt$_{37}$Au$_{20}$, fct-Fe$_{55}$Pt$_{45}$ and commercial Pt NP catalysts, the values drop to 1.62, 1.20, and 0.71 respectively.
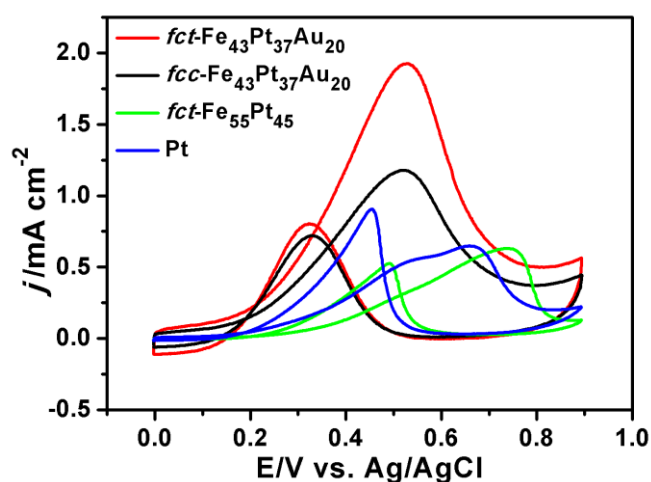
Figure 7-10. CVs of the fct-Fe$_{43}$Pt$_{37}$Au$_{20}$, fcc-Fe$_{43}$Pt$_{37}$Au$_{20}$, fct-Fe$_{55}$Pt$_{45}$ and commercial Pt NPs in the N$_2$-saturated 0.5 M H$_2$SO$_4$ and 0.5 M methanol solution.

7.3 Summary

This work presents a structure-control strategy to tune and optimize FePtAu NP catalysis for FAOR. These NPs are synthesized by a facile solution-phase process with their compositions controlled by the molar ratios of the metal precursors. The presence of Au in FePt facilitates the FePt structure transformation from fcc to fct and further promotes the FAOR in the H$_2$SO$_4$ solution. Among all Pt, FePt and FePtAu NPs tested, the 4 nm fct-Fe$_{43}$Pt$_{37}$Au$_{20}$ NPs are the most active and durable catalyst -

they have the mass activity of 2809.9 mA/mg Pt and retain 92.5% of this activity after 13 h stability test. The high CO-resistant activity of the fct-$Fe_{43}Pt_{37}Au_{20}$ NPs is attributed to surface segregation of Au from the fct-FePt, while the high durability is the result of the formation of the fct structure promoted by Au-segregation within the FePtAu NPs. The work demonstrates the great potentials of fct-FePtAu NPs as highly efficient catalysts for electro-oxidation reactions of organic molecules. More importantly, the structure-control strategy is not limited to FePtAu NPs, but can be extended to other M-doped FePtM (M = Ag, Sb for example),[18] or Pt- and Pd-based multi-metallic NPs, providing a general approach to advanced NP catalysts with simultaneous enhancement in both activity and durability for practical applications.

7.4 Experimental

Synthesis of FePtAu NPs. Under a gentle flow of N_2, 73 mg of platinum acetylacetonate ($Pt(acac)_2$, 0.188 mmol, Aldrich, 98%) and 22 mg of chloroauric acid hydrate ($HAuCl_4 \cdot xH_2O$, 0.063 mmol, 99.9%, Strem Chemicals) were mixed in 20 mL of octadecene (ODE, Aldrich, 90%) in the presence of 0.68 mL of oleylamine (OAm, 2 mmol, Aldrich, 70%) and 140 mg of tetradecylphosphonic acid (TDPA, 1 mmol, Alfa Aesar, 98%). The mixture was magnetically stirred and heated to 100 ℃ to generate a light yellow transparent solution. Under a N_2 blanket, 0.10 mL of iron pentacarbonyl ($Fe(CO)_5$, 0.75 mmol, Aldrich, 99.9+%) was added into the solution, inducing an immediate color change to black in the solution. The solution was heated

to 250 ℃ at a rate of about 20 ℃/min and kept at this temperature for 10 min before it was cooled to room temperature. The NPs were separated by adding isopropanol (50 mL), followed by centrifugation (8500 rpm, 8 min). The NPs were further purified by dispersing into hexane (20 mL) and centrifugation (5000 rpm, 8 min) to remove any un-dispersed precipitates. The product was precipitated out by adding ethanol (50 mL) and centrifugation (8500 rpm, 8 min) and re-dispersed in hexane. The synthesis yielded $Fe_{42}Pt_{44}Au_{14}$ NPs. In the same reaction condition, 61 mg of $Pt(acac)_2$ (0.156 mmol) and 32 mg of $HAuCl_4$ (0.094 mmol) led to the formation of $Fe_{43}Pt_{37}Au_{20}$ NPs. 49 mg of $Pt(acac)_2$ (0.125 mmol) and 43 mg of $HAuCl_4$ (0.125 mmol) yielded $Fe_{34}Pt_{34}Au_{32}$ NPs and 98 mg of $Pt(acac)_2$ (0.25 mmol), and no addition of $HAuCl_4$ gave $Fe_{55}Pt_{45}$ NPs.

NP Structure Characterization. The ICP-AES measurements were carried on a JY2000 Ultrace ICP Atomic Emission Spectrometer equipped with a JY AS 421 autosampler and 2400g/mm holographic grating. XRD characterizations were carried out on a Bruker AXS D8-Advanced diffractometer with Cu Kα radiation (λ =1.5418 Å). Samples for TEM analysis were prepared by depositing a single drop of diluted NP dispersion in hexane on amorphous carbon coated copper grids. TEM images were obtained using a Philips CM 20 (200 kV). HRTEM images were obtained using a FEI Titan 80-300 (300 kV) with an aberration (image) corrector and STEM analyses were carried out using a Hitachi HD2700C (200kV) with a probe

aberration-corrector, in the Center for Functional Nanomaterials at Brookhaven National Lab. The 2D EELS mapping were collected using a high resolution Gatan-Enfina ER with a probe size of 1.3Å and the EDX line-scan was obtained by a Bruker-AXS X-Flash 5030 silicon drift detector with an electron probe of ~2 Å. A power law function was used for EELS background subtraction.

The Preparation of C/NP Catalysts. An equal amount (20 mg each) of NPs and Ketjen carbon support were mixed in 50 mL of hexane/acetone (v/v 1/1) and sonicated with a Fischer Scientific FS 110 for 1 h. The catalyst was separated by centrifugation and washed with hexane twice. The C/NPs were dried under ambient conditions and annealed at different temperatures for 1 h in a gas flow of Ar + 5% H_2. The commercial C/Pt (20% mass loading, 2.5-3.5 nm in diameter) catalysts were obtained from Fuel Cell Store.

Electrochemical measurements. The electrochemical measurements were performed on a Pine Electrochemical Analyzer, Model AFCBP1 with a three-electrode system consisting of a glassy carbon (GC) working electrode (5-mm in diameter), an Ag/AgCl reference electrode (10% KNO_3), and a platinum wire counter electrode. To prepare C/NP-modified GC working electrodes, C/NP NPs were dispersed in a mixture of water/2-propanol/5% Nafion (v/v/v = 1/4/0.025) under sonication to form a 4 mg/mL (for commercial C/Pt or C/Pd catalyst) or 2 mg/mL (for

all the other catalysts) catalyst ink[26]. 20 μL of this ink was dropped onto the surface of the GC electrode, and then dried under ambient conditions. The N_2-saturated 0.5 M H_2SO_4 was used as the test solution. In the CV measurements, the electrode potential was scanned in the range from -0.2 to 0.9 V (*vs.* Ag/AgCl). Chronoamperometry was carried out at the constant potential of 0.2 V in an electrolyte solution containing 0.5 M H_2SO_4 and 0.5 M HCOOH. All the catalyst electrodes were cleaned before data collection with a steady-state CV in the range from -0.25 to 1.0 V (*vs* Ag/AgCl). The scan rate was fixed at 50 mV/s.

References:

1. N. Tian, Z.-Y.Zhou, S.-G. Sun, Y. Ding, Z. L. Wang, *Science* **2007**, *316*, 732-735.

2. B. Lim, M. Jiang, P. H. C. Camargo, E. C. Cho, J. Tao, X. Lu, Y. Zhu, Y. Xia, *Science* **2009**, *324*, 1302-1305.

3. K. Gong, D.Su, R. R. Adzic, *J. Am. Chem. Soc.* **2010**, *132*, 14364-14366.

4. C. Wang, H. Daimon, T. Onodera, T. Koda, S. Sun, *Angew. Chem. Int. Ed.* **2008**, *47*, 3588-3591.

5. Y. Kang, C. B. Murray, *J. Am. Chem. Soc.* **2010**, *132*, 7568-7569.

6. Y.-C. Lu, Z. Xu, H. A. Gasteiger, S. Chen, K. Hamad-Schifferli, S.-H. Yang, *J. Am. Chem. Soc.* **2010**, *132*, 12170-12171.

7. A.-X. Yin, X.-Q. Min, Y.-W. Zhang, C.-H. Yan, *J. Am. Chem. Soc.* **2011**, *133*, 3816-3819.

8. H. Zhang, M. Jin, J. Wang, W. Li, P. H. C. Camargo, M. J. Kim, D. Yang, Z. Xie, Y. Xia, *J. Am. Chem. Soc.* **2011**, *133*, 6078-6089.

9. J. Zhang, H. Yang, J. Fang, S. Zou, *Nano Lett.* **2010**, *10*, 638-644.

10. J. Wu, A. Gross, H. Yang, *Nano Lett.* **2011**, *11*, 798-802.

11. X. Ji, K. T. Lee, R. Holden, L. Zhang, J. Zhang, G. A. Botton, M. Couillard, L. F. Nazar, *Nature Chem.* **2010**, *2*, 286-293.

12. Y. Bing, H. Liu, L. Zhang, D. Ghosh, J. Zhang, *Chem. Soc. Rev.* **2010**, *39*, 2184-2202.

13. A. Cheng, P. Holt-Hindle, *Chem. Rev.* **2010**, *110*, 3767-3804.

14. V. Mazumder, M. Chi, K. L. More, S. Sun, *J. Am. Chem. Soc.* **2010**, *132*, 7848-7849.

15. K. Sasaki, H. Naohara, Y. Cai, Y. M. Choi, P. Liu, M. B. Vukmirovic, J. X. Wang, R. R. Adzic, *Angew. Chem. Int. Ed.* **2010**, *49*, 8602-8607.

16. C. Wang, D. V. D. Vliet, K. L. More, N. J. Zaluzec, S. Peng, S. Sun, H. Daimon, G. Wang, J. Greeley, J. Pearson, A. P. Paulikas, G. Karapetrov, D. Strmcnik, N. M. Markovic, V. R. Stamenkovic, *Nano Lett.* 2011, *11*, 919-926.

17. S. H. Sun, C. B. Murray, D. Weller, L. Folks, A. Moser, *Science* **2000**, *287*, 1989-1992.

18. S. H. Sun, *Adv. Mater.* **2006**, *18*, 393-403.

19. J. Kim, Y. Lee, S. Sun, *J. Am. Chem. Soc* **2010**, *132*, 4996-4997.

20. X. Yu, P. G. Pickup, *J. Power Sources* **2008**, *182*, 124-132.

21. Since these NPs are not magnetically saturated, the coercivity values measured from the hysteresis loops are the low-end numbers and are used only to demonstrate the FePt structure conversion. The coervicity values should be larger than the reported once these NPs are magnetically saturated under a stronger magnetic field.

22. S. Kinge, T. Gang, W. J. M. Naber, H. Boschker, G. Rijnders, D. N. Reinhoudt, W. G. van der Wiel, *Nano Lett.* **2009**, *9*, 3220-3224.

23. S. Kang, A. Jia, D. E. Nikles, J. W. Harrell, *IEEE Trans. Magn.* **2003**, *39*, 2753-2757.

24. We should note that to achieve a complete fcc-fct transition within 4 nm FePtAu NPs is difficult as the small NP size tends to restrict the Fe and Pt mobility unless even higher annealing temperate and longer annealing time are applied, which can cause carbon support degradation and FePtAu NP aggregation/sintering.

25. J. Snyder, T. Fujita, M.W. Chen, J. Erlebacher, *Nat. Mater.* **2010**, *9*, 904-907.

26. S. Guo, S. Zhang, X. Sun, S. Sun, *J. Am. Chem. Soc.* **2011**, *39*, 15354-15357.

27. S. Zhang, Y. Shao, G. Yin, Y. Lin, *Angew. Chem. Int. Ed.* **2010**, *49*, 2211-2214.

28. Y. Mu, H. Liang, J. Hu, L. Jiang, L. Wan, *J. Phys. Chem. B* **2005**, *109*, 22212.

Chapter 8

Ultrathin FePtPd Nanowires as Active Catalyst for Methanol Oxidation Reaction

In Chapter 7, I have introduced the structural tuning of FePtAu nanoparticles (NPs) for highly efficient catalysis in formic acid electrooxidation reaction. Here I am focused on a facile synthesis to ultrathin (2.5 nm) FePtPd alloy nanowires (NWs) with tunable compositions and controlled length (less than 100 nm). The NWs were made by thermal decomposition of $Fe(CO)_5$ and sequential reduction of $Pt(acac)_2$ (acac = acetylacetonate) and $Pd(acac)_2$ at temperatures from 160 °C to 240 °C. These FePtPd NWs showed composition-dependent catalytic activity and stability for methanol oxidation reaction. Among FePtPd, FePt NWs as well as Pd, Pt, and PtPd nanoparticles (NPs) studied in the 0.2 M methanol and 0.1 M $HClO_4$ solution, the $Fe_{28}Pt_{38}Pd_{34}$ NWs showed the highest activity with their mass current density reaching 488.7 mA/mg Pt and peak potential for methanol oxidation decreased to 0.614 V from 0.665 V (Pt NP catalyst). The NW catalysts were also more stable than the NP ones with the $Fe_{28}Pt_{38}Pd_{34}$ NWs retaining the highest mass current density (98.1 mA/mg Pt) after 2 h i-t test at 0.4 V. These trimetallic NWs are a promising new class of catalyst for methanol oxidation reaction and for direct methanol fuel cell

8.1 Background and Motivation

Synthesis of ultra-thin (less than 10 nm) metallic nanowires (NWs) has attracted considerable interest due to the unique magnetic, electronic, and catalytic properties induced by the confined one-dimensional nanostructure.[1-6] FePt alloy NWs with a wire diameter of ~2 nm are made by thermal decomposition of $Fe(CO)_5$ and reduction of $Pt(acac)_2$ (acac = acetylacetonate) in oleylamine.[2] These FePt NWs can be assembled/converted into ferromagnetic FePt arrays with preferred magnetic alignment. Single crystalline Au NWs with diameters less than 10 nm are synthesized by the reduction of $HAuCl_4$ using oleylamine or other reducing agents[3] and the 9 nm Au NWs show good electron conductivity with the breakdown current density reaching 3.5×10^{12} A/m^2.[3a] Recently, ultra-thin NWs are also found to be robust catalyst for various chemical reactions. For example, Pt NWs, made by chemical reduction of H_2PtCl_6 using formic acid as reductant, and core/shell type Pd/Pt NWs, prepared by Cu underpotential deposition on Pd NWs and followed by galvanic displacement of Cu, are more efficient in catalyzing oxygen reduction reaction (ORR) than other forms of the Pt catalysts.[4,5] Pt-based PtM (M = Pd, Ru, Au, Fe, Co) alloy NWs and their network are made available *via* a soft template formed by cetyltrimethylammonium bromide in a two-phase water-chloroform system for hydrogenation and composition-dependent catalytic studies.[6] Our group also report the ultrathin FePt, CoPt, FePtCu and FePtNi NWs or nanorods (NRs) can be used as highly efficient catalysts for ORR due to 1-D effect.[7]

153

Herein, we report a one-pot synthesis of ultrathin trimetallic FePtPd alloy NWs with controllable length, diameter and compositions as more efficient catalyst for methanol oxidation reaction (MOR). We recently developed a facile synthesis of 2 nm wide FePt NWs *via* decomposition of $Fe(CO)_5$ and reduction of $Pt(acac)_2$ in the presence of oleylamine (OAm) or the mixture of OAm and 1-octadecene (ODE).[2] The composition of FePt NWs was tuned by the molar ratio of $Fe(CO)_5/Pt(acac)_2$ and their length was controlled by the volume ratio of OAm/ODE. By adding sodium oleate and adjusting addition sequence of the precursors, we succeeded in making composition-tunable FePtPd NWs with controlled diameter (2.5 nm) and length (less than 100 nm). We found that these FePtPd NWs had a strong interaction with carbon supports and were less vulnerable than conventional nanoparticles (NPs) to dissolution, Ostwald ripening, and aggregation in strong acidic electrocatalytic conditions. They showed high activity and good stability for MOR in 0.1 M $HClO_4$ solution and their activity/stability were composition-dependent with $Fe_{28}Pt_{38}Pd_{34}$ NWs having the lowest methanol oxidation peak potential and being the most efficient catalyst for MOR.

8.2 Results and Discussion

8.2.1 Synthesis of FePtPd NWs

The FePtPd alloy NWs were synthesized by thermal decomposition of $Fe(CO)_5$ and controlled reduction of $Pt(acac)_2$ and $Pd(acac)_2$ (see **Experimental**). Briefly, 0.3

g of sodium oleate was dissolved in 12 mL of 1-octadecene (ODE) by heating the mixture to 180 ℃. The solution was cooled down to 60 °C, added 0.1 g (0.25 mmol) of Pt(acac)$_2$ dissolved in 8 mL of oleylamine (OAm), and re-heated to 120 ℃. After the introduction of Fe(CO)$_5$ (0.07 mL, 0.532 mmol), the solution was heated to 160 ℃, added 75 mg (0.25 mmol) of Pd(acac)$_2$ dissolved in 2 mL OAm + ODE (volume ratio of 2:3), further heated to 240 ℃ at the heating rate of 4-5 ℃/min, and kept at 240 °C for 30 min before it was cooled down. The product was separated and re-dispersed in hexane.

Inductively coupled plasma-atomic emission spectroscopy (ICP-AES) was used to characterize the composition of the as-prepared NWs. In the above synthesis, Fe$_{28}$Pt$_{38}$Pd$_{34}$ NWs were obtained. If no Pd(acac)$_2$ was added, Fe$_{68}$Pt$_{32}$ NWs were separated. With the fixed amount of Fe(CO)$_5$, the composition of FePtPd NWs was tuned by controlling the molar ratio of Pt(acac)$_2$ and Pd(acac)$_2$. Under the same reaction condition as in the synthesis of Fe$_{28}$Pt$_{38}$Pd$_{34}$ NWs, 50 mg (0.167 mmol) and 25 mg (0.0835 mmol) of Pd(acac)$_2$ resulted in Fe$_{43}$Pt$_{34}$Pd$_{23}$ and Fe$_{58}$Pt$_{32}$Pd$_{10}$ NWs, respectively.

The NWs were characterized by transmission electron microscopy (TEM), high-resolution TEM (HRTEM) and X-ray diffraction (XRD). **Figure 8-1A-D** shows the typical TEM images of the as-prepared Fe$_{68}$Pt$_{32}$, Fe$_{58}$Pt$_{32}$Pd$_{10}$, Fe$_{43}$Pt$_{34}$Pd$_{23}$ and Fe$_{28}$Pt$_{38}$Pd$_{34}$ NWs. These NWs have a diameter of 2.5 ±0.3 nm. HRTEM image of a single NW, as shown in **Figure 8-1E**, reveals that the spacing of the adjacent fringes

along the wire growth direction is 0.22 nm, corresponding to the {111} interplanar distance of face-centered cubic (fcc) FePtPd. Another feature of these NWs is that each NW has two larger tips on both ends. This is similar to what is seen in FePt NWs, indicating that the growth of Pd over FePt NWs does not change the overall NW morphology and the large tips are formed by the preferential growth of FePt and Pd at the end due to the low packing density of the surfactant at the tip.[2] XRD patterns of FePt and FePtPd NWs with different compositions and PtPd NPs are shown in **Figure 8-2**. Compared with that of PtPd alloy NPs, the diffraction peaks of FePtPd and FePt NWs shift to larger diffraction angles, indicating the reduction of crystal lattice induced by alloying Fe with Pt or PtPd structure. FePtPd and FePt NWs have very similar diffraction patterns due to the close lattice spacing between Pd- and Pt-based structures. The broadened diffraction peaks from NWs reveal the small dimension of the crystal domains, further proving the ultra-thin character of these NWs.[8]
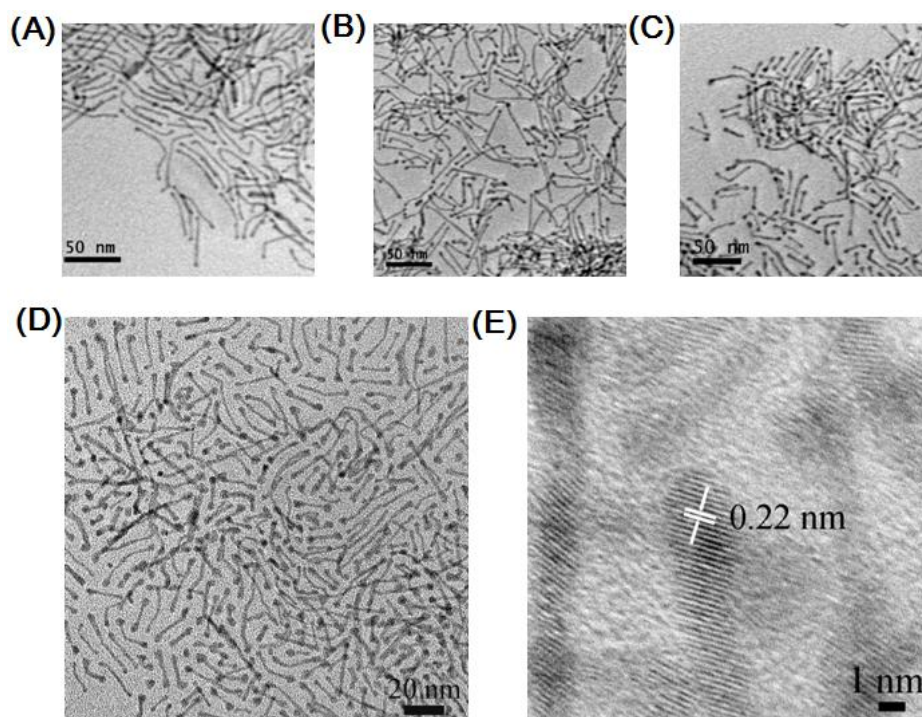
Figure 8-1. TEM (**A-D**) and HRTEM (**E**) images of $Fe_{68}Pt_{32}$ (**A**), $Fe_{58}Pt_{32}Pd_{10}$ (**B**), $Fe_{43}Pt_{34}Pd_{23}$ (**C**) and $Fe_{28}Pt_{38}Pd_{34}$ NWs (**D, E**).
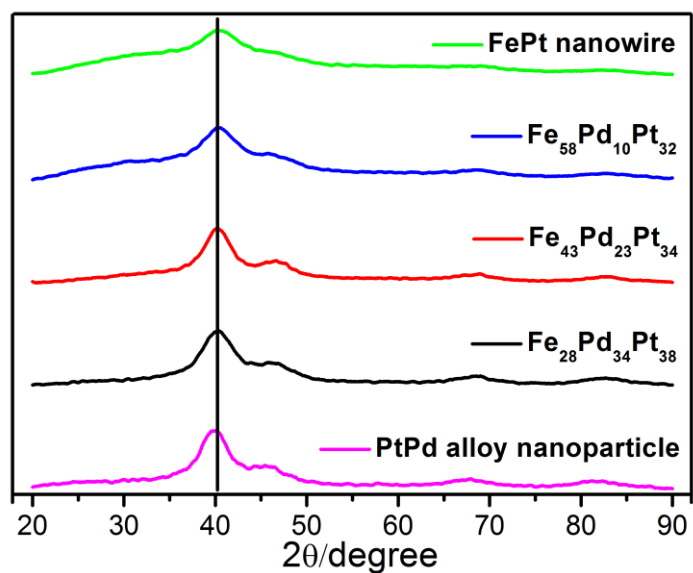
Figure 8-2. XRD patterns of PtPd NPs, FePt NWs and FePtPd NWs with different compostions.

The growth of FePtPd NWs was closely monitored during the synthesis. Before Pd(acac)$_2$ was added to the reaction mixture, the FePt product was separated from the solution heated at 160 °C and characterized by TEM (**Figure 8-3A**). We can see that thin FePt NWs are already present. Furthermore, the molar ratio of Fe/Pt between two precursors is carried over to the final FePt product. This infers that the current synthesis has a high yield formation of FePt NWs. With the addition of Pd(acac)$_2$ in the reaction mixture containing FePt NWs, the percentage of Fe in the final product is decreased and its change in atomic ratio is correlated with the amount of Pd(acac)$_2$ added. For example, in the synthesis of Fe$_{28}$Pt$_{38}$Pd$_{34}$ NWs, if the original molar ratio of the precursors is carried over to the final FePtPd, then we would expect the formation of Fe$_{52}$Pt$_{24}$Pd$_{24}$ NWs. The actual formation of Fe$_{28}$Pt$_{38}$Pd$_{34}$ NWs seems to indicate that upon the addition of Pd(acac)$_2$, Pd(II) is reduced by Fe in FePt NWs *via* galvanic replacement reaction (Fe + Pd^{2+} → Fe^{2+} + Pd), forming Pd-coated FePt NWs. With the extended heating at 240 °C for 30 min, Pd diffuses into FePt NWs and form trimetallic Fe$_{28}$Pt$_{38}$Pd$_{34}$ alloy NWs. This galvanic replacement induced alloy formation is similar to what has been observed in the growth of AuAg alloy nanocages.[9] We should note that the sequential addition of Pt(acac)$_2$ and Pd(acac)$_2$ as described in the synthesis is essential for the formation of alloy NWs. If Pt(acac)$_2$ and Pd(acac)$_2$ were added together before introducing Fe(CO)$_5$ at 120 °C, only irregular NPs were formed (**Figure 8-3B**).
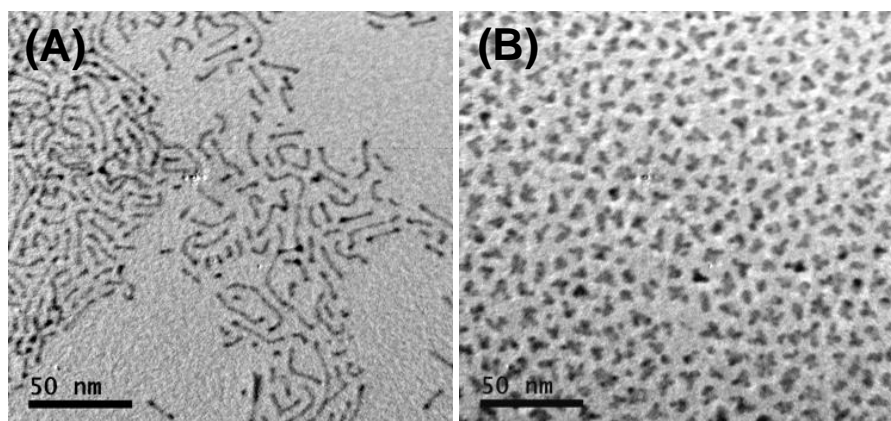
Figure 8-3. TEM images of (**A**) FePt NWs obtained at 160 ℃ and (**B**) the NPs obtained through adding Fe(CO)$_5$ into the mixture of Pt(acac)$_2$ and Pd (acac)$_2$.

In addition to FePt and FePtPd NWs, ~3 nm Pt NPs,[10] ~5 nm Pd NPs,[11] and ~4 nm Pt$_{48}$Pd$_{52}$ alloy NPs[12] were made by previous methods. **Figure 8-4** shows the TEM images of these NPs. They were used as controls to compare with the trimetallic FePtPd NWs in electrochemical and electro-catalytic studies.
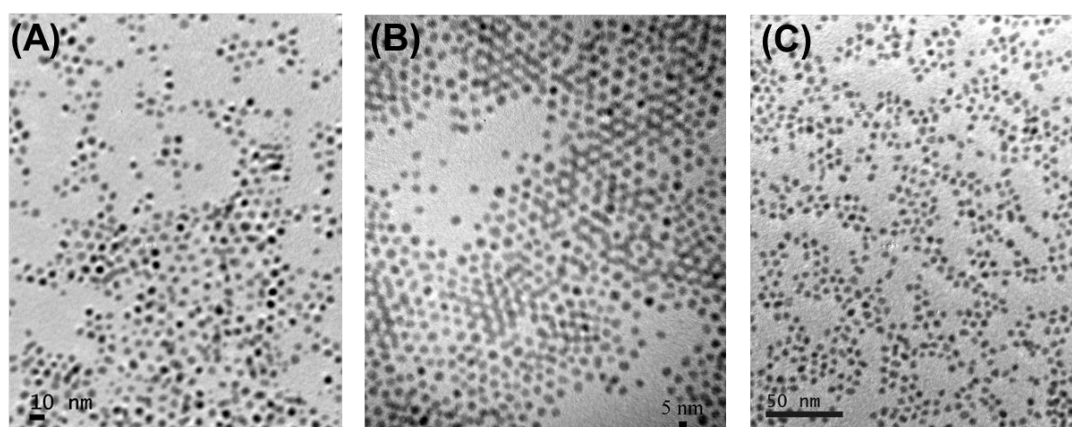
Figure 8-4. TEM images of (**A**) 3 nm Pt NPs, (**B**) 5 nm Pd NPs and (**C**) 4 nm PdPt NPs.

159

8.2.2 Electrocatalysis for MOR of FePtPd NWs

The as-synthesized FePtPd NWs were further characterized by their electrochemical properties. To perform the tests, the NWs or NPs were first deposited on a carbon support (Kejen EC 300J) *via* sonication of the equal amount of two constituents in the mixture of hexane and acetone and then washed with acetic acid (99%) at 70 ℃ to remove the surfactant.[11] During this acid wash, part of Fe in FePtPd NWs was etched away, as confirmed by the composition change from $Fe_{58}Pt_{32}Pd_{10}$, $Fe_{43}Pt_{34}Pd_{23}$ and $Fe_{28}Pt_{38}Pd_{34}$ NWs to $Fe_{49}Pt_{39}Pd_{12}$, $Fe_{36}Pt_{37}Pd_{27}$ and $Fe_{24}Pt_{34}Pd_{32}$ NWs, respectively. The treated NWs/C or NPs/C were redispersed in deionized water + isopropanol (v:v 4:1) to reach a concentration of 2 mg/mL. Nafion at a concentration of 0.025% was also added into the dispersion. 20 μL of this dispersion was deposited on the surface of glassy carbon (GC) electrode and the NWs (or NPs) were fixed onto the electrode by Nafion once the solvent was evaporated. **Figure 8-5A** summarizes the typical cyclic votammograms (CVs) of $Fe_{28}Pt_{38}Pd_{34}$ NWs, $Fe_{68}Pt_{32}$ NWs, Pt NPs, Pd NPs and PtPd NPs in N_2-saturated 0.1 M $HClO_4$. In the positive scan, metals/alloys are oxidized at 0.51-0.65 V. In the negative scan, the oxidized metals/alloys are reduced at 0.3-0.39 V. The reduction peak potential of the FePtPd NWs is similar to that of PdPt, but is between those of Pt, FePt and Pd. The composition effects of FePtPd NWs on oxidation and reduction behaviors of the FePtPd NWs were also studied (**Figure 8-5B**). With the increase of Pd concentration

in FePtPd structure, the reduction peak potential of FePtPd NWs is negatively shifted.

From **Figure 8-5A&B**, we can conclude that FePtPd NWs are formed as an alloy, not

as a core/shell, structure.
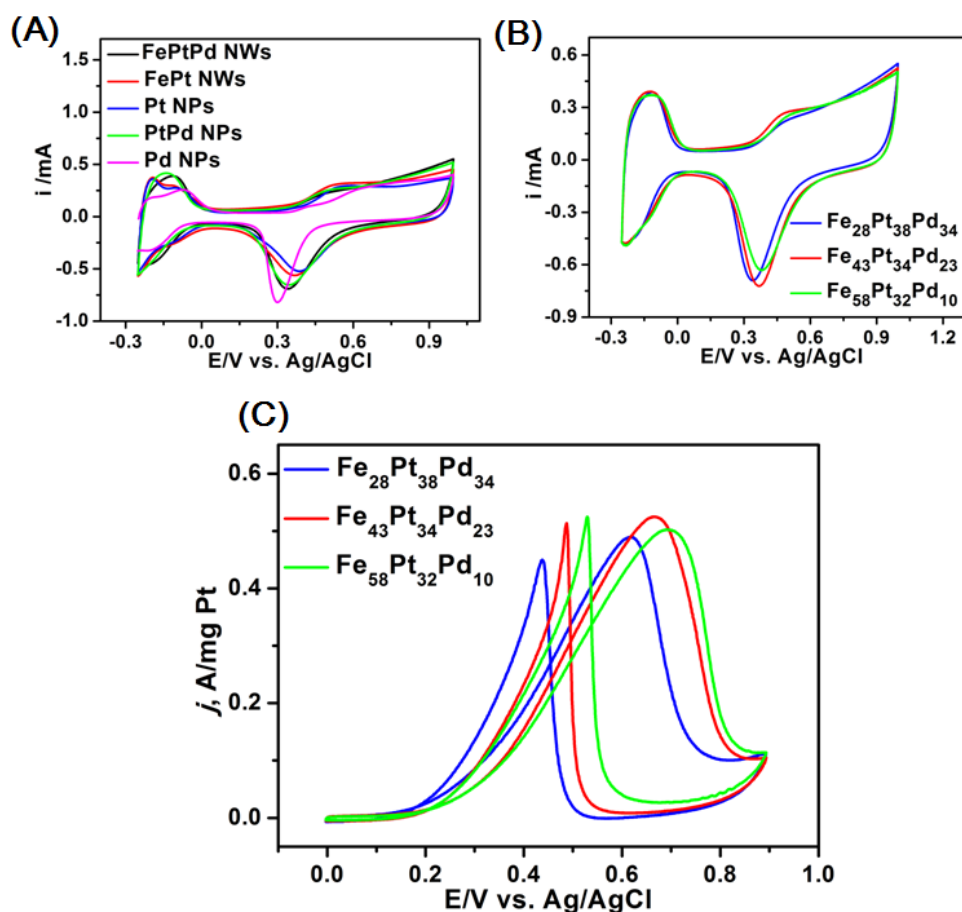
Figure 8-5. CVs of (**A**) $Fe_{28}Pt_{38}Pd_{34}$ NWs, FePt NWs, Pt NPs, Pd NPs and PtPd NPs and (**B**) FePtPd NWs with different compositions in N_2-saturated 0.1 M $HClO_4$ solution at a scan rate of 50 mV/s. (**C**) CVs of MOR catalyzed by FePtPd NWs with different compositions in N_2-saturated 0.1 M $HClO_4$ and 0.2 M methanol solution at a scan rate of 50 mV/s.

The FePtPd NWs are electro-catalytically active for MOR. The electro-oxidation

curves of these NWs in 0.1 M $HClO_4$ and 0.2 M methanol solution are shown in

Figure 8-5C. Among three kinds of FePtPd NWs investigated, $Fe_{28}Pt_{38}Pd_{34}$ NWs

have the highest activity by displaying less positive oxidation peak potential at 0.614 V and high mass current density at 488.7 mA/mg Pt. The catalytic performance of $Fe_{28}Pt_{38}Pd_{34}$ NWs was further compared with Pt, PtPd and FePt catalysts (the Pd catalyst was not active for MOR (**Figure 8-6**)). **Figure 8-7A** shows the CVs of MOR catalyzed by $Fe_{28}Pt_{38}Pd_{34}$ NWs, $Fe_{68}Pt_{32}$ NWs, 3 nm Pt NPs and 4 nm $Pt_{48}Pd_{52}$ alloy NPs in a solution containing 0.1 M $HClO_4$ and 0.2 M methanol. We can see that the $Fe_{28}Pt_{38}Pd_{34}$ NWs have a significant increase in peak current density and a negative potential shift in methanol oxidation peak over Pt, PtPd and FePt catalysts. The $Fe_{28}Pt_{38}Pd_{34}$ NWs have also the lowest potential for MOR at the same oxidation current density (the inset of **Figure 8-7A**). These indicate that $Fe_{28}Pt_{38}Pd_{34}$ NWs have much enhanced catalytic activity for MOR.
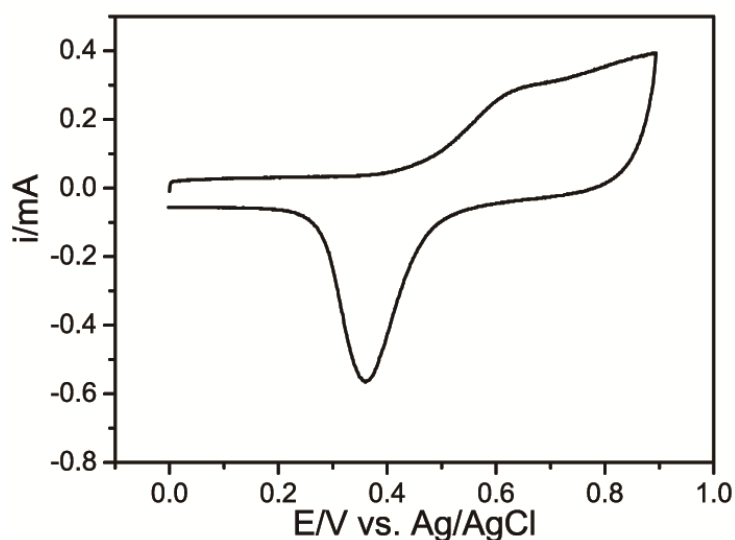
Figure 8-6. CV of methanol oxidation on a Pd/C-modified GC electrode in N_2-saturated 0.1 M $HClO_4$ + 0.2 M methanol solution at the scan rate of 50 mV/s.
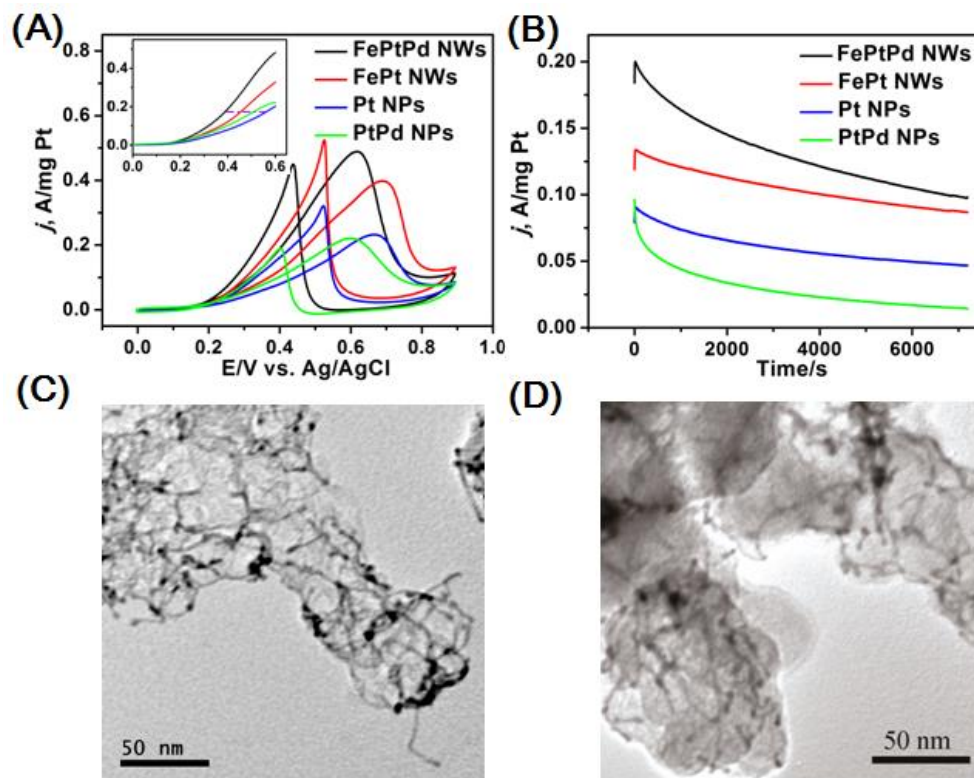
Figure 8-7. CVs (**A**), linear sweep voltammetry (inset) and i-t curves (**B**) of MOR catalyzed by $Fe_{28}Pt_{38}Pd_{34}$ NWs, FePt NWs, Pt NPs and PtPd NPs in 0.1 M $HClO_4$ + 0.2 M methanol solution. The CVs were obtained at a scan rate of 50 mV/s and the i-t curves were collected at a constant potential of 0.4 V. TEM images of the $Fe_{28}Pt_{38}Pd_{34}$ NWs/C before (**C**) and after (**D**) 2 h i-t test.

Chronoamperometry, a useful method used for evaluation of electrocatalyst stability in fuel cells,[13] was employed to investigate the electrochemical activity and stability of different catalysts. **Figure 8-8 and 8-7B** are typical current (i) - time (t) test results on various catalysts. We can see that the FePtPd NWs have the highest activity among all catalysts studied both before and after the 2 h i-t test. **Figure 8-7B** also shows that the Pd-containing catalysts have a faster decay rate than the non-Pd catalysts. These indicate that Pd in the alloy structure is not very stable in the acidic MOR condition and can be etched away readily. The catalyst morphology change

during the i-t test was monitored by TEM, as shown in **Figure 8-7C** & **D** and **Figure 8-9 & 8-10**. The FePtPd and FePt NWs have no noticeable morphology change before and after the test, whereas Pt NPs show sign of aggregation. This enhanced stability of NWs *vs* NPs is likely caused by stronger NW interactions with carbon support and/or by better NW structure stability,[4, 14] which makes the NWs less subject to dissolution, Ostwald ripening, and aggregation than NPs in the acidic MOR condition.
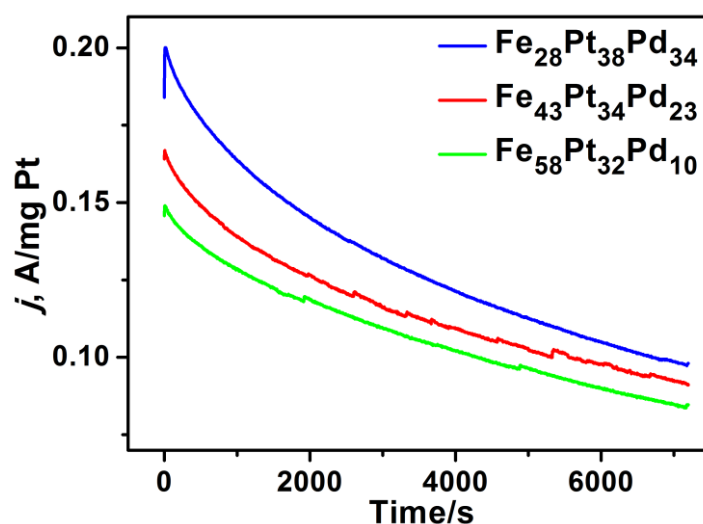
Figure 8-8. Current density-time curves of methanol oxidation reaction catalyzed by FePtPd NWs with different compositions in N_2-saturated 0.1 M $HClO_4$ and 0.2 M methanol solution. The curves were collected at a constant potential of 0.4 V.
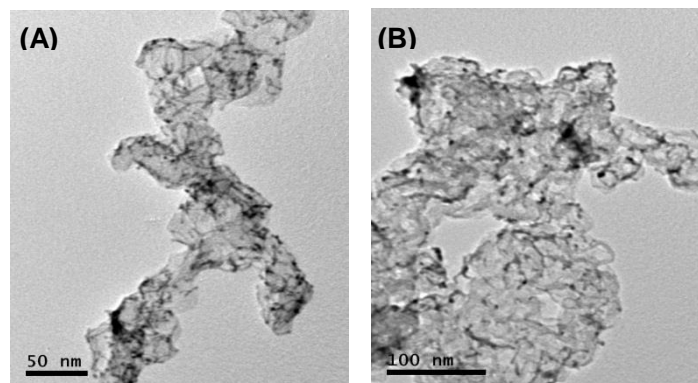
Figure 8-9. TEM images of the FePt NWs before (**A**) and after (**B**) 2 h i-t test.
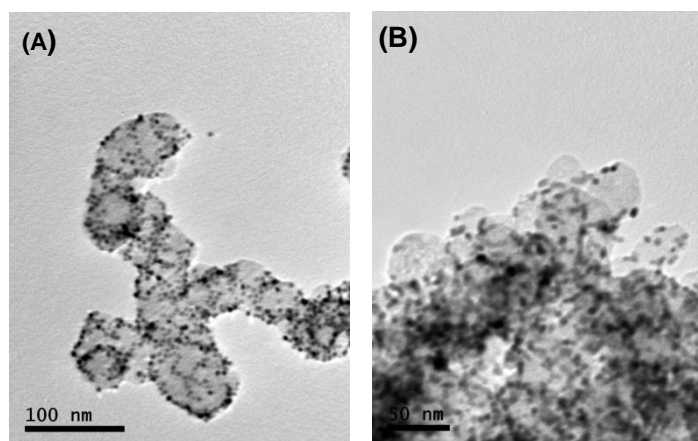
Figure 8-10. TEM images of the Pt NPs before (**A**) and after (**B**) 2 h i-t test.

8.3 Summary

In summary, we have developed a facile synthesis of ultra-thin trimetallic FePtPd alloy NWs by thermal decomposition of $Fe(CO)_5$ and sequential reduction of $Pt(acac)_2$ and $Pd(acac)_2$. The key to the successful synthesis is that FePt NWs should first be made and Pd is allowed to deposit on FePt NWs *via* a galvanic replacement of

Fe with Pd followed by a high temperature (240 °C) reaction. The FePtPd NWs have a diameter around 2.5 nm and length less than 100 nm. More importantly, due to the molar ratio carryover from the precursors to the product, the compositions of these trimentallic NWs are readily tuned. These FePtPd NWs show composition-dependent MOR activity and stability and $Fe_{28}Pt_{38}Pd_{34}$ NWs are the most efficient MOR catalyst with the mass current density reaching 488.7 mA/mg Pt and oxidation peak potential decreased to 0.614 V from 0.665 (Pt NP catalyst). The reported synthesis should offer a general approach to trimetallic NWs as a promising new class of catalyst for direct methanol fuel cell and other advanced catalytic applications.

8.4 Experimental

Chemicals and Materials. Oleylamine (OAm, >70%), 1-octadecene (ODE, technical grade, 90%), oleic acid (OA, technical grade, 90%), Pt(acac)$_2$ (acac=aceylacetonate) (99.99%), Pd(acac)$_2$ (99%), iron pentacarbonyl (Fe(CO)$_5$, 99.9+% trace metals basis), hexane (98.5%), isopropanol (99.5%), ethanol (100%), acetic acid (99%), borane t-butylamine complex (BTC) (97%), morphiline borane (MB) (95%) and Nafion (5% in a mixture of lower aliphatic alcohols and water) were all purchased from Sigma Aldrich. Sodium oleate (97%) was obtained from Tokyo Chemical Industry CO., LTD.

Synthesis of FePtPd NWs. Under a gentle nitrgen (N$_2$) flow and a magnetic stirring,

0.3 g of sodium oleate and 12 mL of ODE were mixed and heated to 180 ℃ to make a clear solution. The solution was cooled down to 60 ℃, added 0.1 g of $Pt(acac)_2$ dissolved in 8 mL of OAm, and re-heated to 120 ℃. Under a blanket of N_2, 0.07 mL of $Fe(CO)_5$ was injected into the reaction solution. The solution was heated to 160 ℃ and injected 75 mg (or 50 mg, or 25 mg) of $Pd(acac)_2$ dissolved in 2 mL of OAm. The soluion was finally heated to 240 ℃ at a heating rate of 4-5 ℃/min and kept at this temperature for 30 min. The reaction mixture was cooled to 40-50 ℃, added 30 mL of hexane and then 30 mL of ethanol to precipitate out the product. The product was separated by centrifugation at 9000 rpm for 10 min. The NWs were dispersed in hexane.

Synthesis of FePt NWs. The synthetic procedure was same as that of FePtPd NWs, except that after $Fe(CO)_5$ was injected, the mixture was directly heated to 240 ℃ at the heating rate of 4-5 ℃/min.

Synthesis of 4 nm PtPd NPs. For a typical synthesis of $Pt_{48}Pd_{52}$ NPs, $Pd(acac)_2$ and $Pt(acac)_2$ were dissolved in 15 ml of OAm at 60 ℃ under N_2 protection. 0.2 g of MB (dissolving in 2 mL of OAm) was quickly injected into the above solution. The reaction mixture was heated to 180 ℃ and kept at this temperature for 30 min. After cooled down to room temperature, the NP product was precipitated by adding isopropanol and centrifugation. The NPs were puried for two more times by

re-dispersing in hexane and re-precipitation upon the addition of isopropanol and were finally dispersed in hexane.

Surfactant Removal from NPs or NWs. The surfactant on the surface of NWs or NPs was removed according to our previous report.[11] An equal amount (20 mg each) of NWs (or NPs) and Ketjen-300J carbon support were mixed in 50 mL of hexane/acetone (v/v 1/1) and sonicated with a Fischer Scientific FS 110 for 1 h. The catalyst was separated by centrifugation, and washed with hexane for two times, and mixed with 30 mL of acetic acid. The suspension was heated to 70 °C for overnight. The catalyst was separated by centrifugation and washed with water for two times before it was re-dispersed in a mixture solvent containing water, isopropanol and Nafion (5%) (v:v:v 4:1:0.025) to form a 2 mg/mL suspension.

Catalyst Deposition on the Working Electrode. The glassy carbon working electrode was first polished with 1.0 and 0.05 μm alumina powder, rinsed with deionized water, and sonicated first in ethanol and then in double-distilled water. The electrode was allowed to dry under nitrogen. 20 μL of catalyst ink was casted on the electrode and dried at ambient condition. The test solution was 0.1 M $HClO_4$ and 0.1 M $HClO_4$ + 0.2 M methanol, and was N_2-saturated. In the CV measurements, the electrode potential was scanned in the range of 0-0.9 V *versus* Ag/AgCl. Chronoamperometry was carried out at the constant potential of 0.4 V in 0.1 M

$HClO_4$ + 0.2 M methanol. All the catalyst electrodes were cleaned before data collection with a steady-state CV in the range of -0.25-1.0 V *versus* Ag/AgCl at 50 mV/s.

Characterization. X-ray diffraction (XRD) characterization was carried out on a Bruker AXS D8-Advanced diffractometer with Cu Kα radiation (λ =1.5418 Å). The Inductively coupled plasma-atomic emission spectroscopy (ICP-AES) measurements were carried on a JY2000 Ultrace ICP Atomic Emission Spectrometer equipped with a JY AS 421 autosampler and 2400g/mm holographic grating. Samples for transmission electron microscopy (TEM) analysis were prepared by depositing a single drop of diluted nanoparticle (NP) or nanowire (NW) dispersion in hexane on amorphous carbon coated copper grids. TEM images were obtained with a Philips CM 20 operating at 200 kV. High-resolution TEM (HRTEM) images were obtained on a JEOL 2010 with an accerating votalage of 200 kV. The electrochemical measurements were performed on a Pine Electrochemical Analyzer, Model AFCBP1. A three-electrode system was consisted of glassy carbon (GC) working electrode (5-mm in diameter), an Ag-AgCl reference electrode (10% KNO_3), and a platinum wire counter electrode, respectively.

Reference

1. (a) Cademartiri, L.; Ozin, G. A. *Adv. Mater*. **2009**, *21*, 1013-1020. (b) Wang, C.; Sun, S. *Chem. Asian J*. **2009**, *4*, 1028 – 1034.

2. Wang, C.; Hou, Y.; Kim, J.; Sun, S. *Angew. Chem. Int. Ed*. **2007**, *46*, 6333-6335.

3. (a) Wang, C.; Hu, Y.; Lieber, C. M.; Sun, S. *J. Am. Chem. Soc*. **2008**, *130*, 8902-8903. (b) Lu, X.; Yavuz, M. S.; Tuan, H.-Y.; Korgel, B. A.; Xia, Y. *J. Am. Chem. Soc*. **2008**, *130*, 8900. (c) Huo, Z.; Tsung, C.-K.; Huang, W.; Zhang, X.; Yang, P. *Nano Lett*. **2008**, *8*, 2041-2044. (d) Xu, J.; Wang, H.; Liu, C.; Yang, Y.; Chen, T.; Wang, Y.; Wang, F.; Liu, X.; Xing, B.; Chen, H. *J. Am. Chem. Soc*. **2010**, *132*, 11920-11922. (e) Pazos-Prez, N.; Baranov, D.; Irsen, S.; Hilgendorff, M.; Liz-Marzn, L. M.; Giersig, M. *Langmuir* **2008**, *24*, 9855-9860. (f) Feng, H.; Yang, Y.; You, Y.; Li, G.; Guo, J.; Yu, T.; Shen, Z.; Wu, T.; Xing, B. *Chem. Commun*. **2009**, *45*, 1984-1986.

4. Sun, S.; Zhang, G.; Geng, D.; Chen, Y.; Li, R.; Cai, M.; Sun, X. *Angew. Chem. Int. Ed*. **2011**, *50*, 422-426.

5. Koenigsmann, C.; Santulli, A. C.; Gong, K.; Vukmirovic, M. B.; Zhou, W.-P.; Sutter, E.; Wong, S. S.; Adzic, R. R. *J. Am. Chem. Soc*. **2011**, *133*, 9783-9795.

6. Yang, S.; Hong, F.; Wang, L.; Guo, S.; Song, X.; Ding, B.; Yang, Z. *J. Phys. Chem. C* **2010**, *114*, 203-207.

7. (a) Guo, S.; Li, D.; Zhu, H.; Zhang, S.; Markovic, N. M.; Stamenkovic, V. R. *Angew. Chem. Int. Ed.* **2013**, *52*, 3465-3468. (b) Zhu, H.; Zhang, S.; Guo, S.; Su, D.; Sun, S. *J. Am. Chem. Soc.* **2013**, *135*, 7130-7133.

8. (a) Chen, M.; Kim, J.; Liu, J. P.; Fan, H.; Sun, S. *J. Am. Chem. Soc.* **2006**, *128*, 7132-7133. (b) Metin, O.; Mazumder, V.; Ozkar, S.; Sun, S. *J. Am. Chem. Soc.* **2010**, *132*, 1468-1469.

9. Lu, X.; Au, L.; McLellan, J.; Li, Z.-Y.; Marquez, M.; Xia, Y. *Nano Lett.* **2007**, **7**, 1764-1769.

10. (a) Wang, C.; Daimon, H.; Onodera, T.; Koda, T.; Sun, S. *Angew. Chem. Int. Ed.* **2008**, *47*, 3588-3591. (b) Wang, C.; Daimon, H.; Sun, S. *Nano Lett.* **2009**, *9*, 1493-1496.

11. Mazumder, V.; Sun, S. *J. Am. Chem. Soc.* **2009**, *131*, 4588-4589.

12. Liu, Y.; Chi, M.; Mazumder, V.; More, K. L.; Soled, S.; Henao, J. D.; Sun, S. *Chem. Mater*. **2011**, *23*, 4199-4203.

13. Guo, S.; Dong, S.; Wang, E. *Adv. Mater.* **2010**, *22*, 1269-1272.

14. (a) Chen, Z.; Waje, M.; Li, W.; Yan, Y. *Angew. Chem. Int. Ed.* **2007**, *46*, 4060-4063. (b) Guo, S.; Dong, S.; Wang, E. *Energy Environ. Sci.* **2010**, *3*, 1307-1310.

Chapter 9

Monodisperse AgPd Alloy Nanoparticles and Their Superior Catalysis for Formic Acid Dehydrogenation

In the previous chapters, I have demonstrated how to synthetically tune metallic nanoparticles (NPs) to optimize their catalysis for fuel cell reactions. In this chapter, beyond the electrochemical reactions, I study the NPs heterogeneous catalyst for chemical hydrogen generation- formic acid dehydrogenation (FAD) reaction. We develop a facile approach to composition-controlled synthesis of monodisperse 2.2 nm AgPd alloy NPs. These 2.2 nm AgPd NPs are highly active and durable catalysts for formic acid dehydrogenation. In 1 M formic acid aqueous solution at 50 $^{\circ}$C, the AgPd NPs show the composition-dependent catalysis and $Ag_{42}Pd_{58}$ NPs have the highest activity with an initial TOF of 382 h^{-1} and an apparent activation energy of 22 $\pm$ 1 kJ•mol^{-1}. The work proves the unique approach in using alloying effects to enhance NP catalysis for hydrogen generation from formic acid.

9.1 Background and Motivation

Formic acid (FA, HCOOH) is a common small organic acid with a melting point of 8.4°C and boiling point of 100.8°C. It can undergo a dehydrogenation reaction, HCOOH → H_2 + CO_2, releasing H_2 that will be important for hydrogen-based energy applications. [1] Traditionally, FA dehydrogenation is catalyzed by metal complexes dissolved in an organic solvent and the catalysis is enhanced by adding an additive, such as sodium formate or amine adducts. [2] To make more practical catalyst for the FA dehydrogenation reaction, heterogeneous catalysts based on metal nanoparticles (NPs) are of great interest (**Figure 9-1**). These catalysts are generally more stable but much less active than the homogeneous ones. [3] The **Table 9-1** summaries all the typical NPs heterogeneous catalysts studied for FA dehydrogenation. Recently, bimetallic NP catalysts were found to be more active than their single component counterparts for the FA dehydrogenation. [4] For example, AgPd NPs supported on cerium oxide or AuPd NPs immobilized on metal organic framework showed an enhanced FA dehydrogenation catalysis with the initial turnover frequency (TOF) reaching 210 h^{-1} or 192 h^{-1} at 90°C. [5] However, the high rate of hydrogen generation observed from these heterogeneous catalysts could only be achieved when an additive was present and the reaction was maintained at temperatures close to 100 ^{o}C. [6] Under these "harsh" conditions, HCOOH was also subject to an undesired dehydration reaction, HCOOH → H_2O + CO. [7] Interestingly, Ag/Pd core/shell NPs were found to be promising in catalyzing FA dehydrogenation in an aqueous FA solution at lower

173

temperatures (up to 50°C) without any additive. [8] But their initial TOF's were in the range of 125-252 h^{-1} at temperatures between 25-50 $^{\circ}$C.
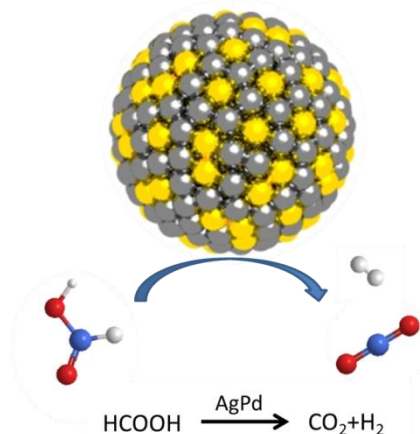
Figure 9-1. The schematic illustration of FA dehydrogenation catalyzed by NP heterogeneous catalyst.

Catalyst (Support)	Substrate/Solvent/Additive	T (^{O}C)	TOF (h^{-1})	Ref
Pd (C)	HCOOH/H$_2$O/HCOONa (Flow)	70	180	6a
Au (C)	HCOOH/H$_2$O/- (High pressure)	80	5	3b
AuPd (CeO$_2$)	HCOOH/H$_2$O/HCOONa	92	227	5a
AuPd (MOF)	HCOOH/H$_2$O/HCOONa (excess)	92	192	5b
Ag/Pd core/shell (C)	HCOOH/H$_2$O/- HCOOH/H$_2$O/-	25 50	127 252	8

Table 9-1. The typical NP heterogeneous catalysts studied for FA dehydrogenation in aqueous solution.
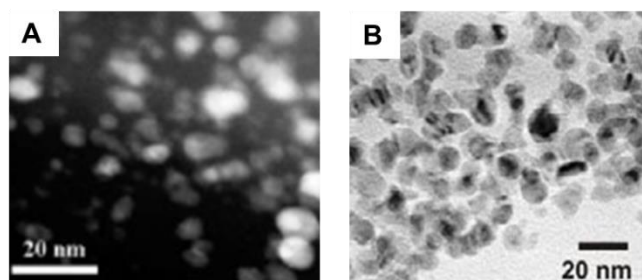
Figure 9-2. TEM images of AuPd NPs immobilized on metal organic framework and Ag/Pd core/shell NPs (Adopted from reference 5b and 8).

It is clearly seen that all these previous NPs synthesized for FA dehydrogenation have limitations in controlling NP size and composition, as show in **Figure 9-2**. With this consideration in mind, we decided to re-evaluate the binary alloy NPs on their catalysis for FA dehydrogenation. Our very recent report showed that monodisperse 4 nm AuPd NPs were more active in catalyzing FA dehydrogenation in water at 50 °C without using any additive and their initial TOF reached 230 h^{-1}.[9] Encouraged by this result, we further improved our solution phase synthesis and produced monodisperse 2.2 nm AgPd NPs with the desired composition controls. We found that these monodisperse 2.2 nm AgPd alloy NPs were a highly-active heterogeneous catalyst for the FA dehydrogenation. In water without any additive, the $Ag_{42}Pd_{58}$ NPs showed the highest catalytic activity among all AgPd tested with their initial TOF reaching 382 h^{-1} at 50 °C and apparent activation energy at 22 ± 1 kJ•mol^{-1}. These are the best values ever reported by a heterogeneous catalyst for the FA dehydrogenation in aqueous solution. It demonstrates the great potential of binary alloy NPs as a more practical catalyst for FA dehydrogenation and hydrogen generation.

9.2 Results and Discussion

The 2.2 nm AgPd alloy NPs were synthesized by co-reduction of silver(I) acetate, Ag(Ac), and palladium(II) acetylacetonate, Pd(acac)$_2$, in oleylamine (OAm), oleic acid (OA) and 1-octadecene (ODE) at 180 ^{o}C (see **Experimental**). Here, OA served as a surfactant and OAm was added both as a co-surfactant and mild reducing agent. The composition of the AgPd NPs (Ag$_{25}$Pd$_{75}$, Ag$_{42}$Pd$_{58}$, Ag$_{52}$Pd$_{48}$, Ag$_{60}$Pd$_{40}$, and Ag$_{80}$Pd$_{20}$) were controlled by varying the molar ratio of Ag(Ac)/Pd(acac)$_2$ and analyzed by inductively coupled plasma-atomic emission spectroscopy (ICP-AES) (**Table 9-2**). Transmission electron microscopy (TEM) images of the as-synthesized AgPd NPs show that they have a mean particle size of 2.2 nm $\pm$ 0.1 nm (**Figure 9-3A & 9-4A-D**). Under the similar reaction condition, we also synthesized 2.2 nm $\pm$ 0.1 nm Ag NPs (**Figure 9-4E**) and 4.5 nm $\pm$ 0.2 nm Pd NPs (**Figure 9-4F**) by reducing only Ag(Ac) or Pd(acac)$_2$.

Sample	Ag(Ac)/Pd(acac)$_2$ molar ratio	As-synthesized NPs
A	4:1	Ag$_{80}$Pd$_{20}$
B	3:1	Ag$_{60}$Pd$_{40}$
C	6:4	Ag$_{52}$Pd$_{48}$
D	1:1	Ag$_{42}$Pd$_{58}$
E	1:3	Ag$_{25}$Pd$_{75}$

Table 9-2. The composition control of AgPd NPs by varying the molar ratios of Ag(Ac)/Pd(acac)$_2$.
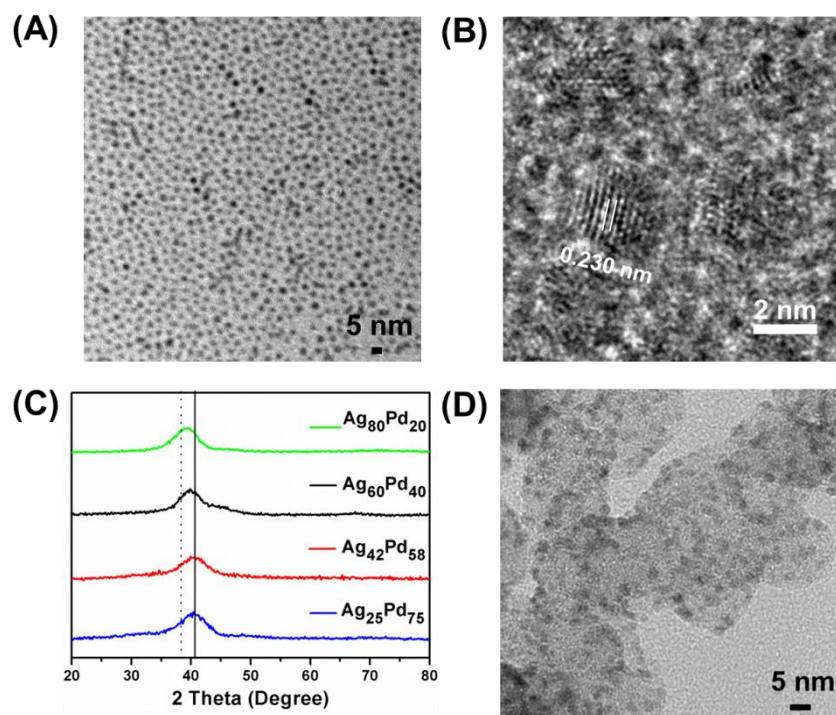
Figure 9-3. (A) TEM image of the 2.2 nm Ag$_{42}$Pd$_{58}$ NPs. **(B)** HRTEM image of the 2.2 nm Ag$_{42}$Pd$_{58}$ NPs. **(C)** XRD patterns of the 2.2 nm Ag$_{25}$Pd$_{75}$, Ag$_{42}$Pd$_{58}$, Ag$_{60}$Pd$_{40}$ and Ag$_{80}$Pd$_{20}$ NPs (dash line and solid line denote standard (111) peak positions of bulk Ag and Pd respectively). **(D)** TEM image of the carbon-supported 2.2 nm Ag$_{42}$Pd$_{58}$ NPs after treated with acetic acid.
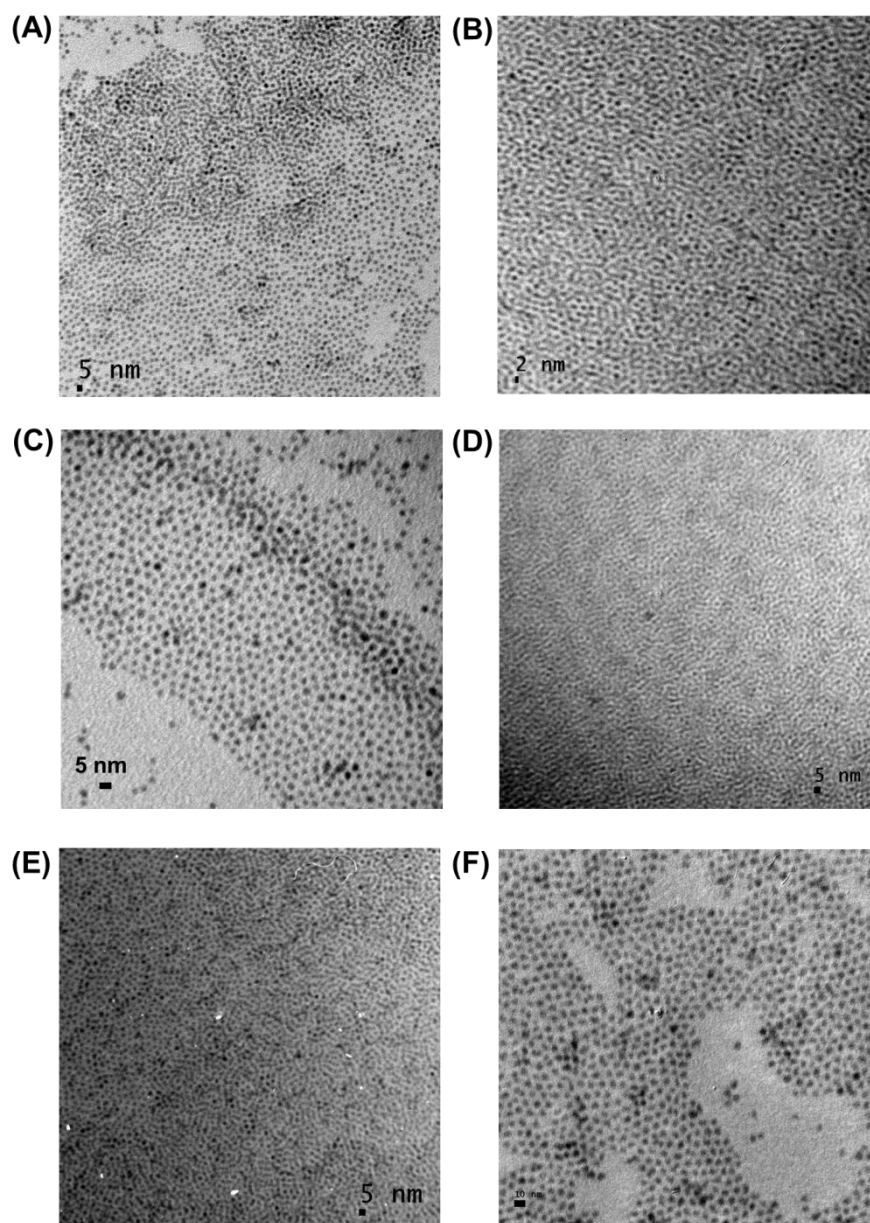
Figure 9-4. TEM images of **(A)** $Ag_{25}Pd_{75}$, **(B)** $Ag_{52}Pd_{48}$, **(C)** $Ag_{60}Pd_{40}$, **(D)** $Ag_{80}Pd_{20}$, **(E)** Ag NPs and **(F)** Pd NPs.

Different from the previous approaches to AgPd alloy NPs (larger than 7 nm) by a strong reducing agent,[5a] or a multi-step reaction scheme (diffusing Pd into Ag seeds in high temperature),[10] our one-step co-reduction of metal salts by OAm is

highly efficient in producing monodisperse AgPd NPs at only 2.2 nm. The use of excess amount of OA was crucial for NP size controls. If OA was present in a small amount (e.g 0.5 mL) or no OA was used, polydisperse AgPd NPs were obtained (**Figure 9-5A&B**).
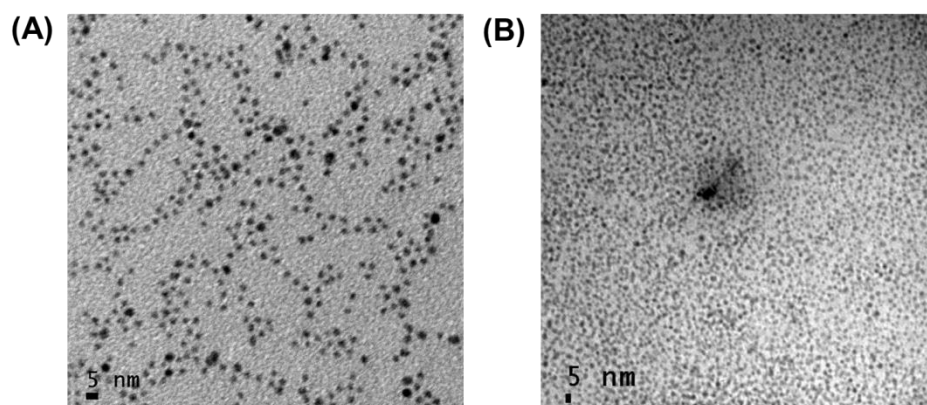
Figure 9-5. TEM images of the AgPd NPs synthesized by using (**A**) 0.5 ml of OA and (**B**) without OA.

A representative high resolution (HR) TEM image of the 2.2 nm $Ag_{42}Pd_{58}$ NPs (**Figure 9-3B**) shows the (111) lattice fringe distance of 0.23 nm, which is between the (111) lattice spacing of face centered cubic (*fcc*) Ag (0.24 nm) and *fcc* Pd (0.22 nm). **Figure 9-3C** is the X-ray diffraction (XRD) patterns of the 2.2 nm AgPd NPs. The AgPd NPs have very weak peak intensity due to their small size. With the Ag amount increased in AgPd, the (111) peak shifts to a lower angle towards Ag (111) due to the increase of the lattice parameters, indicating that AgPd is formed as an alloy, not a core/shell, structure. Furthermore, AgPd NPs show almost no surface

plasmon resonance (SPR) absorption in UV-vis spectra, while Ag NPs have a very strong SPR absorption at 425 nm (**Figure 9-6**). This SPR "quenching" caused by the alloying effect was also observed in other Ag- and Au-based alloy NPs.[11]
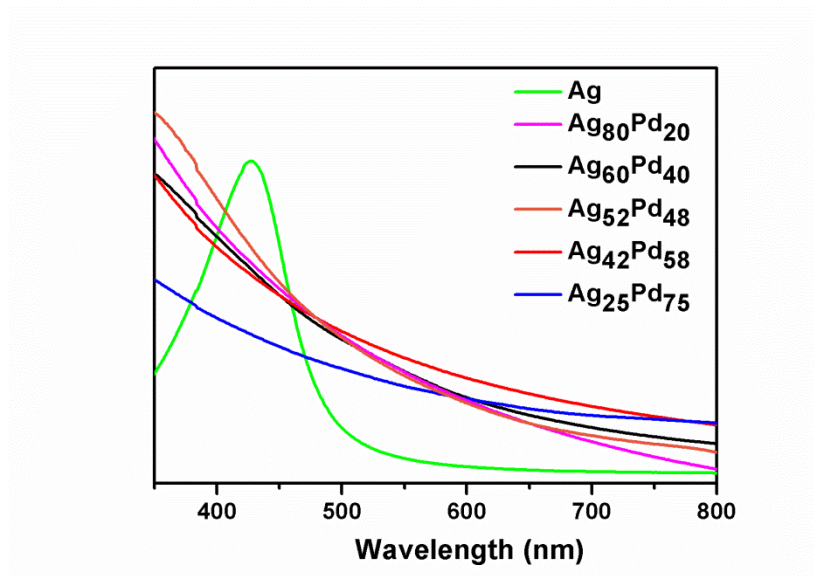
Figure 9-6. UV-vis spectra of the 2.2 nm Ag, $Ag_{80}Pd_{20}$, $Ag_{60}Pd_{40}$, $Ag_{52}Pd_{48}$, $Ag_{42}Pd_{58}$ and $Ag_{25}Pd_{75}$ NPs.

To study NP catalysis for FA dehydrogenation in water, we deposited Ag, Pd, or AgPd NPs on Ketjen carbon (C) and cleaned these C-NPs via acetic acid treatment and ethanol washing followed by drying under vacuum (see **Experimental**). The representative TEM image (**Figure 9-2D**) and the relevant ICP-AES analysis (**Table 9-3**) revealed that these C-AgPd NPs preserved their size, morphology and composition after the cleaning process. The metal contents of the C-AgPd, C-Pd and C-Ag catalysts were measured (by ICP-AES) to have 17 wt% AgPd, 19 wt% Pd and

18 wt% Ag, respectively.

Sample	As-synthesized NPs	After AA washing
A	$Ag_{80}Pd_{20}$	$Ag_{77}Pd_{23}$
B	$Ag_{60}Pd_{40}$	$Ag_{59}Pd_{41}$
C	$Ag_{52}Pd_{48}$	$Ag_{50}Pd_{50}$
D	$Ag_{42}Pd_{58}$	$Ag_{41}Pd_{59}$
E	$Ag_{25}Pd_{75}$	$Ag_{25}Pd_{75}$

Table 9-3. AgPd NP compositions before and after the acetic acid treatment.

The catalytic activity of the C-NP catalysts in FA dehydrogenation was evaluated in a gas burette system. **Figure 9-7A** shows the plots of volume of gas ($CO_2 + H_2$) generated vs. reaction time during the dehydrogenation of aqueous FA solution (10 mL, 1 M FA solution at 50 ^{o}C) catalyzed by different C-AgPd and C-Pd. We can see that most C-AgPd catalysts have higher activity than the C-Pd NPs, except C-$Ag_{80}Pd_{20}$. The C-$Ag_{25}Pd_{75}$, C-$Ag_{42}Pd_{58}$, and C-$Ag_{52}Pd_{48}$ catalysts have the initial TOF of 318 h^{-1}, 382 h^{-1} and 228 h^{-1}, respectively. They are even more active than the state-of-the-art AgPd alloy (TOF = 210 h^{-1} at 92 ^{o}C) and Ag/Pd core/shell NPs (TOF = 252 h^{-1} at 50 ^{o}C). **Figure 9-7B** shows the plot of TOF vs. mole fraction of Ag for the C-AgPd catalyst at different compositions. The TOF increases with the increasing Ag mole ratio up to 0.42, then decreases. The observed "volcano" type activity of the

C-AgPd catalyst vs. Ag/Pd compositions indicates that although neither Ag nor Pd is active for catalyzing FA dehydrogenation reaction, alloying Ag with Pd provides a necessary synergistic effect on the catalysis and $Ag_{42}Pd_{58}$ is the optimum catalyst for catalyzing FA dehydrogenation. This further supports that Ag and Pd form a uniform alloy structure in the synthesis.
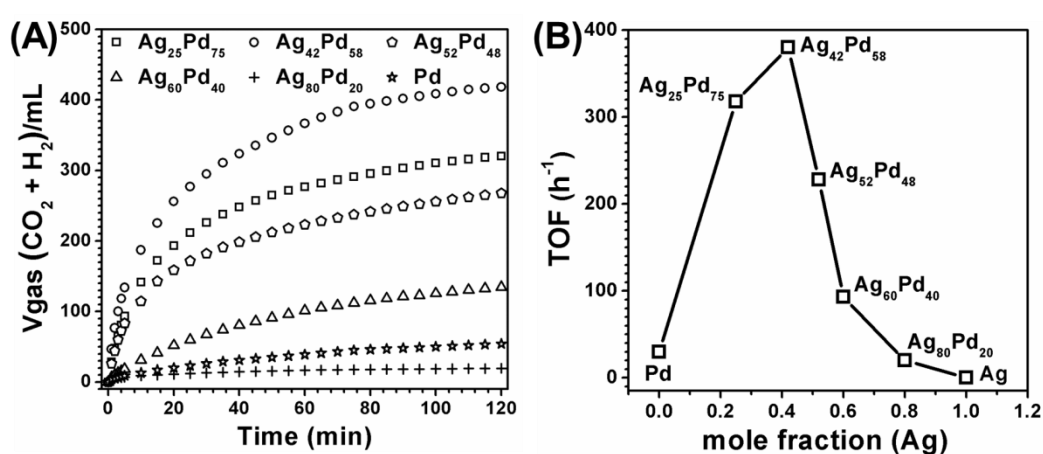
Figure 9-7. (**A**) The plots of gas (CO_2+H_2) generated vs. time during the dehydrogenation of aqueous FA solution (10 mL of 1 M, 50 ^{o}C) in the presence of C-AgPd and C-Pd catalysts and (**B**) TOF vs. mole fraction of Ag for the C-AgPd catalysts at different Ag, Pd compositions.

Since FA dehydration route (HCOOH → CO + H_2O) is generally associated with the dehydrogenation at relatively high reaction temperatures (T > 60 ^{o}C),[3,7] we also tested our reaction and characterized the evolving gas mixture with FT-IR and mass spectroscopy. We found no detectable amount of CO in the gas mixture generated from the C-$Ag_{42}Pd_{58}$ catalyzed FA dehydrogenation (**Figure 9-8**). After reacting the gas mixture with the aqueous NaOH solution, the volumes of CO_2 and H_2 were

estimated and the gas mixture was found to consist of equal molar of CO_2 and H_2 (**Figure 9-9**), proving that the AgPd catalyst promotes complete FA dehydrogenation into CO_2 and H_2. The drastic dehydrogenation activity enhancement of these 2.2 nm AgPd NPs is likely caused by their small size and the synergistic effect between Ag and Pd in the alloy structure that inhibits the adsorption of CO on Pd. This is consistent with what was observed on the CeO_2-supported MPd systems.[5a] However, our system is also different from the CeO_2-supported MPd catalyst in which the enhanced activity was believed to originate from the NP-support interactions,[5a] and ours seem to show more drastic alloy effect with their catalysis optimized when AgPd $= Ag_{42}Pd_{58}$.
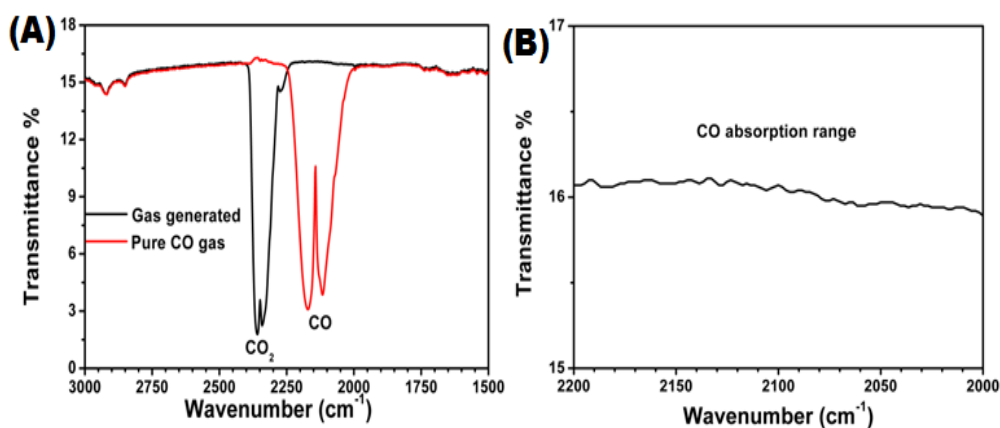
Figure 9-8. FTIR spectra of pure CO gas and gas generated during the C-$Ag_{42}Pd_{58}$ catalyzed FA dehydrogenation in water at 50 °C for 1 h (**A**) and the zoom-in of the CO stretching absorption range (**B**).
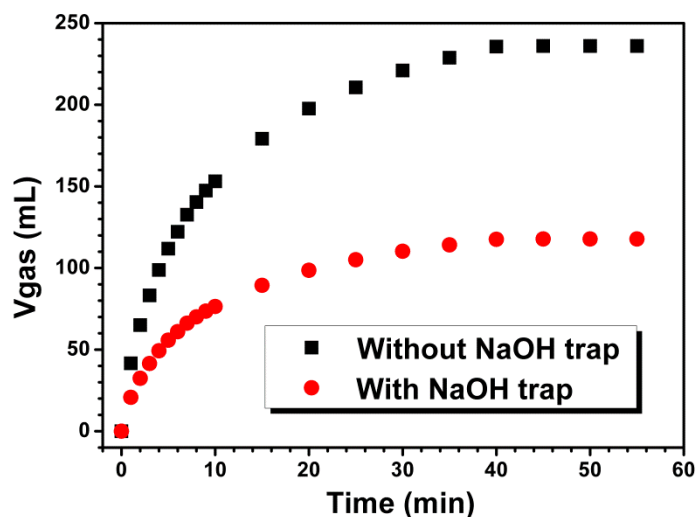
Figure 9-9. The comparison of the volume of gas generated during the C-$Ag_{42}Pd_{58}$ catalyzed dehydrogenation of aqueous FA solution (10 mL, 0.5 M) with and without NaOH trap.

NP catalyst concentration, FA concentration and temperature effects were studied to obtain more kinetic information for FA dehydrogenation. In the first set of experiments, the dehydrogenation reaction was performed at different catalyst concentrations in the range of 10 mg – 40 mg (1.6 - 6.4 mM) $Ag_{42}Pd_{58}$ by keeping the FA concentration at 1.0 M and temperature at 50 ^{o}C. The volume of gas ($CO_2 + H_2$) generated vs. reaction time during the FA dehydrogenation at different catalyst concentrations were plotted (**Figure 9-10A**). The hydrogen generation rates from each catalyst concentration were calculated from the linear portion of each plot comprising 20 min reaction duration. **Figure 9-10B** shows the logarithmic plot of hydrogen generation rate vs. AgPd concentration. The line with a slope of 0.88 in the **Figure 9-10B** indicates the reaction is close to the first-order with respect to the catalyst concentration.
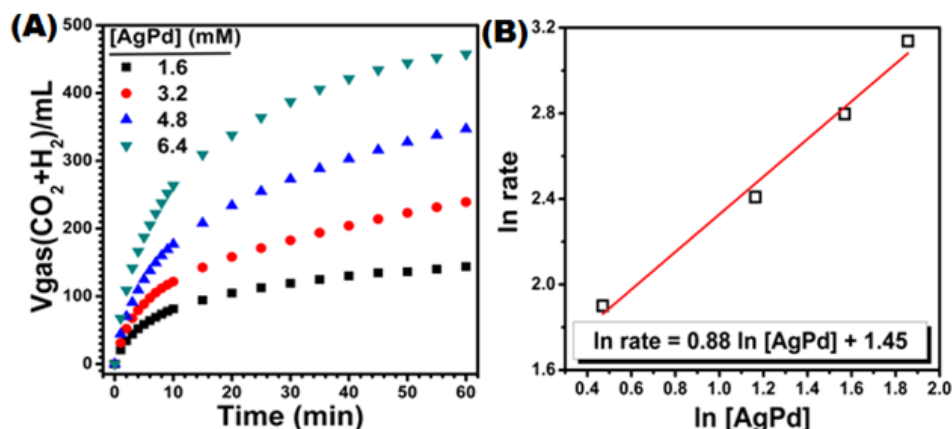
Figure 9-10. **(A)** Gas (CO_2+H_2) generated vs. time during the dehydrogenation of aqueous FA solution (10 mL, 1 M, 50 ^oC) in the presence of different catalyst concentrations, and **(B)** plot of hydrogen generation rate vs. AgPd concentration.

To study FA concentration effect on the gas generation rate, we kept the C-Ag$_{42}$Pd$_{58}$ concentration at 3.2 mM Ag$_{42}$Pd$_{58}$ and temperature at 50 ℃. **Figure 9-11A** shows the volume of gas (CO_2 + H_2) generated vs. time at different FA concentrations. The initial TOFs (h^{-1}) were calculated and presented in **Figure 9-11B**. From **Figure 9-11A&B**, we can see a volcano shaped relationship between TOF and HCOOH concentration. The gas generation rate increases almost linearly with FA concentration in the range of 0.125-1.0 M, but drops when HCOOH concentration is higher than 1 M. This, plus catalyst inactivity observed in dehydrogenating pure FA, reveals that large amount of water plays an indispensible role in catalytic FA dehydrogenation. To measure the ease of the dehydrogenation reaction catalyzed by the AgPd alloy catalyst, we recorded the time-dependent H_2 generations at different temperatures (25-50 ^oC) in the presence of C-Ag$_{42}$Pd$_{58}$ (3.2 mM AgPd) and FA (1 M),

as shown in **Figure 9-11C**. By converting the reactivity into TOF and by plotting

logarithmic TOF vs. 1/T, we obtained the Arrhenius plot (**Figure 9-11D**). From the

linear Arrhenius behavior, we calculated the apparent activation energy (E_a^{app}) to be

22 ± 1 kJ·mol^{-1} for the C-Ag$_{42}$Pd$_{58}$ catalyzed FA dehydrogenation reaction. This is the

lowest value ever reported for the FA dehydrogenation reaction catalyzed by a

heterogeneous catalyst.
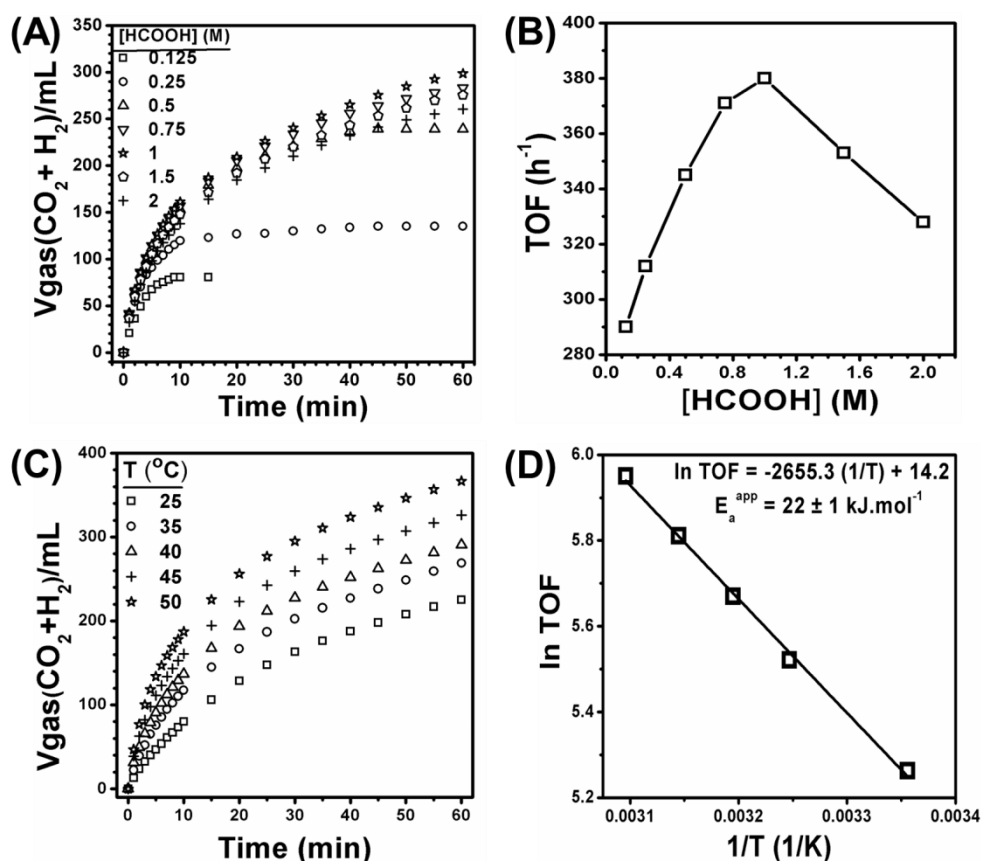
Figure 9-11. (**A**) The volume of the gas ($CO_2 + H_2$) generated vs. time for the FA dehydrogenation catalyzed by the C-Ag$_{42}$Pd$_{58}$ at different FA concentrations (0.125-2 M). (**B**) The plot of initial TOF (h^{-1}) vs FA concentration. (**C**) The volume of the gas ($CO_2 + H_2$) generated vs. time for the FA dehydrogenation catalyzed by the C-Ag$_{42}$Pd$_{58}$ at different different temperatures (25-50 $^{\circ}$C). (**D**) Arrhenius plot (ln TOF vs. 1/T).

We further tested briefly the stability of C-Ag$_{52}$Pd$_{48}$ catalyst by performing the FA dehydrogenation in water at 50 ^{o}C and recovering the catalyst from the solution after the reaction completion for the next round of reaction. Our tests showed that the C-Ag$_{42}$Pd$_{58}$ catalyst preserved 90% of its initial activity after the fourth run (**Figure 9-12A**). We analyzed the recovered catalyst by ICP-AES and TEM (**Figure 9-12B**). We found no obvious change in the Ag/Pd composition, catalyst loading on carbon, and NP morphology. These indicate that the C-Ag$_{42}$Pd$_{58}$ catalyst was stable in the current FA dehydrogenation condition and could be re-used for multiple rounds of the dehydrogenation reaction.
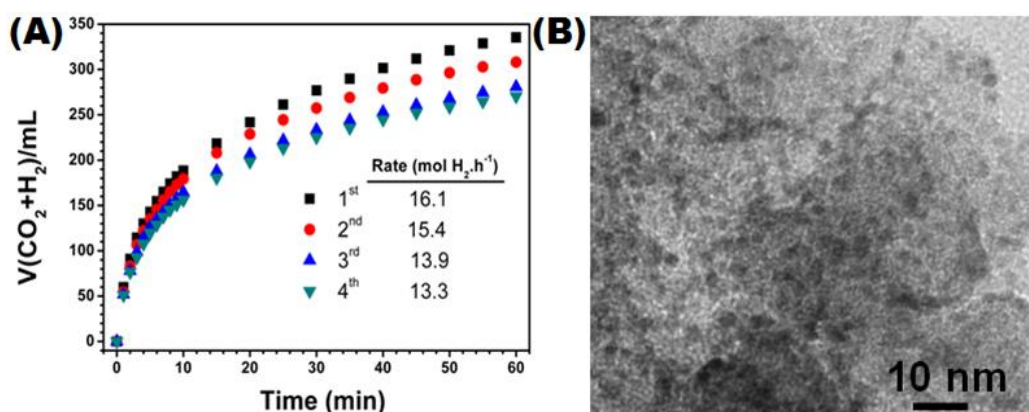
Figure 9-12. (A) The gas (CO$_2$+H$_2$) - reaction time plot obtained from four reaction cycles of the C-Ag$_{42}$Pd$_{58}$ catalyst in the dehydrogenation of aqueous FA solution (10 mL, 1 M) at 50 ^{o}C. **(B)** A representative TEM image of the C-Ag$_{42}$Pd$_{58}$ catalyst after the 4th catalytic run.

9.3 Summary

In this chapter we have demonstrated a facile approach to composition-controlled synthesis of monodisperse 2.2 nm AgPd NPs. These 2.2 nm AgPd NPs are highly

active and durable as catalysts for FA dehydrogenation and for hydrogen generation without the need of any additive. Under our evaluation condition (in water at 50 ^{o}C), the AgPd NPs show the composition-dependent catalysis and the $Ag_{42}Pd_{58}$ NPs have the highest activity with an initial TOF of 382 h^{-1} and an apparent activation energy of 22 ± 1 kJ•mol^{-1} – the best catalytic performance ever reported among all heterogeneous catalysts tested for FA dehydrogenation in aqueous solution. This, combining with the fact that Pd and Ag NPs are much less active in catalyzing FA dehydrogenation, proves the unique approach in using alloying effects to enhance NP catalysis. With the desired control on NP sizes, compositions and shapes, NP catalysis for FA dehydrogenation can be further optimized and a new type of heterogeneous catalyst may be developed for hydrogen generation and for hydrogen-based energy device applications.

9.4 Experimental

Materials. Oleylamine (OAm, >70%), oleic acid (OA, 90%), 1-octadecene (ODE, 90%), hexane (98.5%), ethanol (100%), and acetic acid (AA, 99%) were purchased from Sigma-Aldrich® without further purification. Palladium (II) acetylacetonate (Pd(acac)$_2$, 99%) and silver (I) acetate (AgAc, 99%) was purchased from Strem Chemicals® without further purification. The deionized water was obtained from a Millipore-Autopure system.

Synthesis of AgPd NPs. Under a gentle nitrogen flow, 0.084 g of silver (I) acetate (Ag(Ac), 0.5 mmol) and 0.15 g of palladium (II) acetylacetonate (Pd(acac)$_2$, 0.5 mmol) were magnetically stirred in 4.5 ml of oleic acid (OAc), 0.5 ml of oleylamine (OAm) and 10 ml of 1-octadecene (ODE). The mixture was heated to 60 ℃ to generate a homogeneous solution. Then the solution was heated to 180 ℃ at a rate of 3-5 ℃/min and kept at this temperature for 20 min during which the transparent solution was gradually turned into brown and finally dark-brown color. Once the reaction solution was cooled down to room temperature, the NPs were separated by adding isopropanol (50 mL) and centrifugation (9500 rpm, 8 min). To remove the organic impurities and precursor residues, the product was redispersed in 10 ml of hexane and then recollected by adding 40 ml of ethanol and centrifugation (9500 rpm, 8 min). This synthesis yielded Ag$_{42}$Pd$_{58}$NPs (yield: 95%), which were dispersed in hexane for future use. In the same reaction condition, 0.134 g of Ag(Ac) (0.8 mmol) and 0.06 g of Pd(acac)$_2$ (0. 2 mmol) led to the formation of Ag$_{80}$Pd$_{20}$ NPs; 0. 126 g of Ag(Ac) (0.75 mmol) and 0.075 g of Pd(acac)$_2$ (0. 25 mmol) generated Ag$_{60}$Pd$_{40}$ NPs; 0. 1 g of Ag(Ac) (0.6 mmol) and 0.12 g of Pd(acac)$_2$ (0. 4 mmol) produced Ag$_{52}$Pd$_{48}$ NPs; 0. 042 g of Ag(Ac) (0.25 mmol) and 0.225 g of Pd(acac)$_2$ (0. 75 mmol) yielded Ag$_{25}$Pd$_{75}$ NPs. Under the similar conditions, 0.168 g of Ag(Ac) (1 mmol) in the absence of Pd(acac)$_2$ yielded 2.2 nm Ag NPs. The synthesis of 4.5 nm Pd NPs was conducted according to a protocol published elsewhere.[12]

Preparation of C-NP catalysts. 50 mg of Ketjen carbon were suspended in 10 mL of hexane and sonicated for 15 min. Next, ~25 mg of NPs in hexane was added

dropwise into the carbon support mixture under sonication. The resulted mixture was sonicated for 1 h to ensure NP adsorption onto the carbon support. The C-NPs were separated by centrifugation and washed with ethanol. Next, the C-NPs were suspended in 30 mL of acetic acid and the suspension was heated for 10 h at 70 ^{o}C. 30 mL of ethanol was added and the mixture was centrifuged at 8500 rpm for 6 min. This ethanol washing procedure was repeated three times. The C-NPs were recovered and dried under vacuum.

Formic acid dehydrogenation. 20 mg of C-NP catalysts were dispersed in 9.6 mL of water via sonication and then 0.4 mL of formic acid was injected into the catalyst solution at 50 ^{o}C. The volume of the gas (CO_2 + H_2) generated during the catalytic reaction was monitored by a gas burette system.

Characterization. The inductively coupled plasma-atomic emission spectroscopy (ICP-AES) measurements were carried on a JY2000 Ultrace ICP Atomic Emission Spectrometer equipped with a JY AS 421 autosampler and 2400g/mm holographic grating. TEM were conducted on a Philips CM 20 operating at 200 kV. Samples for TEM analysis were prepared by depositing a single drop of diluted NP dispersion in hexane on amorphous carbon coated copper grids. HRTEM images were obtained using a JEOL 2100F (200 kV) with an field-emission electron source in the Center

for Functional Nanomaterials at Brookhaven National Lab. X-ray diffraction (XRD) characterization was carried out on a Bruker AXS D8-Advanced diffractometer with Cu Kα radiation (λ =1.5418 Å). The UV/Vis spectra were recorded on a Perkin Elmer Lambda 35 spectrometer. Infrared spectra were recorded on a Bruker Tensor 27 FTIR spectrometer.

NaOH Trap Experiments. To understand the CO_2 to H_2 molar ratio in the gas mixture generated during the C-$Ag_{42}Pd_{58}$ catalyzed dehydrogenation of aqueous FA solution (10 mL of 0.5 M), we performed NaOH trap experiment as reported elsewhere. [5b] In this experiment, the gas burette system was modified by placement of trap (10 M NaOH solution) between the jacketed reactor and gas burette. The generated gas during the reaction was passed through the NaOH trap and the CO_2 was captured. Next, the volume of the gas generated from catalytic FA dehydrogenation was monitored and compared to those without trap experiment (**Figure 9-9**). The volume of the gas was decreased almost 50% in same time intervals, indicating the volume ratio of CO_2 to H_2 was ~1.

Reference

1. (a) B. Loges, A. Boddien, F. Gätner, H. Junge, M. Beller, *Top. Catal.* **2010**, *53*, 902-914. (b) T. C. Johnson, D .J. Morris, M. Wills, *Chem. Soc. Rev.* **2010**, *39*, 81-88. (c) S. Enthaler, *ChemSusChem* **2008**, 1, 801-804. (d) F. Joo, *ChemSusChem* **2008**, *1*, 805-808.

2. (a) A. Boddien, B. Loges, H. Junge, M. Beller, *ChemSusChem* **2008**, *1*, 751-758. (b) B. Loges, A. Boddien, H. Junge, M. Beller, *Angew. Chem. Int. Ed.* **2008**, *47*, 3962-3965. (c) C. Fellay, P. J. Dyson, G. Laurenczy, *Angew. Chem. Int. Ed.* **2008**, *47*, 3966-3968. (d) Y. Himeda, *Green Chem.* **2009**, *11*, 2018-2022. (e) W. Gan, C. Fellay, P. J. Dyson, G. Laurenczy, *J. Coord. Chem.* **2010**, *63*, 2685-2694.

3. (a) M. Grasemann, G. Laurency, *Energy Environ. Sci.* **2012**, *5*, 8171-8181. (b) A. Gazsi, T. Bánsági, and F. Solymosi, *J. Phys. Chem. C* **2011**, *115*, 15459-15466.

4. (a) S. W. Ting, S. Cheng, K. Y. Tsang, N. Laak, K. Y. Chan, *Chem. Commun.* **2009**, 7333-7335. (b) Y. Huang, X. Zhou, M. Yin, C. Liu, W. Xing, *Chem. Mater.* **2010**, *22*, 5122-5128.

5. (a) X. Zhou, Y. Huang, W. Xing, C. Liu, J. Liao, T. Lu, *Chem. Commun.* **2008**, 3540-3542. (b) X. Gu, Z. H. Lu, H. L. Jiang, T. Akita, Q. Xu, *J. Am. Chem. Soc.* **2011**, *133*, 11822-11825.

6. (a) D. A. Bulushev, S. Beloshapkin, J. R. H. Ross, *Catal. Today* **2010**, *154*, 7-12. (b) Q. Y. Bi, X. L. Du, Y. M. Liu, Y. Cao, H. Y. He, K. N. Fan, *J. Am. Chem. Soc.* **2012**, *134*, 8926-8933.

7. N. Akiya, P. E. Savage, *AIChE J.* **1998**, *44*, 405-415.

8. K. Tedsree, T. Li, S. Jones, C. W. A. Chan, K. M. K. Yu, P. A. J. Bagot, E. A. Marquis, G. D. W. Smith, S. C. E. Tsang, *Nat. Nanotech.* **2011**, *6*, 302-307.

9. Ö. Metin, X. Sun, S. Sun, *Nanoscale* **2013**, *5*, 910-913.

10. (a) D. A. Slanac, W. G. Hardin, K. P. Johnston, K. J. Stevenson, *J. Am. Chem. Soc.* **2011**, *134*, 9812-9819. (b) J. Yang, J. Yang, J. Y. Yang, *ACS Nano* **2012**, *6*, 9373-9382.

11. F. Abild-Pedersen, M.P Andersson, *Surf. Sci.* **2007**, *601*, 1747-1753.

12. V. Mazumder, S. Sun, *J. Am. Chem. Soc*. **2009**, *131*, 4588-4589.